

ABSTRACT

Damage Accumulation of Bovine Bone Under Chaotic Loading

Michelle L. Cler, M.S.B.M.E.

Mentors: Joe Kuehl, Ph.D.

Carolyn Skurla, Ph.D.

A stress fracture is a common injury that plagues many individuals. Since there is not currently a method to predict if a stress fracture will develop, this pilot study was conducted to determine if either the Palmgren-Miner rule (PMR) or phase space warping (PSW) could be used as a prediction method for fatigue failure in bone tissue. In this study the Moon's beam experimental set-up was used to perform fatigue tests on bovine bone specimens. Scanning electron microscopy was used to evaluate the fracture surface and identify the fracture type. It was found that the PMR tended to under predict the fatigue life of the specimens. The PSW method was able to successfully identify the various damage modes and may be a viable tool for predicting the fatigue life of bone. As such, PSW is worth further research. Many more tests need to be completed to obtain statistical significance.

Damage Accumulation of Bovine Bone Under Chaotic Loading

by

Michelle L. Cler, B.S.E.

A Thesis

Approved by the Department of Mechanical Engineering

Kenneth Van Treuren, Ph.D., Interim Chairperson

Submitted to the Graduate Faculty of
Baylor University in Partial Fulfillment of the
Requirements for the Degree
of
Master of Science in Biomedical Engineering

Approved by the Thesis Committee

Joseph Kuehl, Ph.D., Co-Chairperson

Carolyn Skurla, Ph.D., Co-Chairperson

Erich Baker, Ph.D.

Accepted by the Graduate School

December 2016

J. Larry Lyon, Ph.D., Dean

Copyright © 2016 by Michelle L. Cler

All rights reserved

TABLE OF CONTENTS

LIST OF FIGURES	vii
LIST OF TABLES	xi
NOMENCLATURE	xii
ACKNOWLEDGMENTS	xiii
DEDICATION	xiv
CHAPTER ONE	1
Introduction.....	1
Stress Fractures	1
Hierarchical Structure of Bone	2
Properties of Bone.....	4
Constitutive Fatigue Model.....	10
Estimation of Fatigue Limit	15
CHAPTER TWO	24
Materials and Methods.....	24
Specimen Preparation	24
Testing Apparatus	26
Experimental Method.....	32
Analysis.....	34
CHAPTER THREE	38
Results.....	38
Break Classification	40
Rainflow Counting.....	44
Palmgren-Miner Rule.....	49
Phase Space Warping.....	49
CHAPTER FOUR.....	52
Discussion and Conclusion.....	52
Discussion	52
Conclusion	55
CHAPTER Five	57
Future Work.....	57
Determine Strain	57

Improve Apparatus.....	58
Statistical Significance.....	59
APPENDIX A.....	61
Data Logbook	61
APPENDIX B.....	62
Fracture Surface Images Taken with 16 Megapixel Camera.....	62
APPENDIX C.....	66
Data Summaries.....	66
Specimen 1 (2015121701).....	66
Specimen 2 (2016012002).....	67
Specimen 3 (2016012101).....	68
Specimen 4 (2016012701).....	69
Specimen 5 (2016020401).....	70
Specimen 6 (2016020501).....	71
Specimen 7 (2016021201).....	72
Specimen 8 (2016021401).....	73
Specimen 9 (2016030401).....	74
Specimen 10 (2016030701).....	75
APPENDIX D.....	76
MATLAB Code.....	76
Resonant Frequency.....	76
Trim Data File.....	77
Retrieve Column Data From File.....	78
Rainflow Counting with 0.25 mm Bins.....	81
Rainflow Counting with 3 Amplitude Bins.....	87
Palmgren-Miner Rule.....	93
Phase Space Warping Protocol Code.....	94
Phase Space Warping Code Set.....	96
APPENDIX E.....	97
CAD Drawings.....	97
Shaker Converter Piece.....	97
8 inch Connector Arm.....	97
C-Frame Top Arm.....	99
Fastener Cap.....	100
C-Frame Vertical Arm.....	101
C-Frame Base Arm.....	102
Linear Guide Conversion Piece.....	103
Magnet Holder Cap.....	104
Magnet Holder Slider.....	105
Pendulum Metal Plates.....	106
Laser Stand Base.....	107

Laser Stand Plate.....	108
Laser Stand Vertical Rod	109
Laser Stand Fastener	110
APPENDIX F.....	111
Specifications.....	111
Amplifier.....	111
Laser Vibrometer	113
Linear Guide	114
Shaker	115
APPENDIX G.....	116
Testing Apparatus of Prior Study	116
APPENDIX H.....	117
Bill of Materials	117
BIBLIOGRAPHY.....	119

LIST OF FIGURES

Figure 1.1. Hierarchical structure of bone	3
Figure 1.2. Load-deformation curve of bovine femoral cortical bone.....	5
Figure 1.3. Effect of strain rate in bone	6
Figure 1.4. Strength and modulus of human cortical bone	7
Figure 1.5. Four-point bend load versus displacement curves for hydrated and dehydrated bovine bone	7
Figure 1.6. Percentage of bone loss and recovery in the femur.....	9
Figure 1.7. Bone toughening mechanisms.....	12
Figure 1.8. Osteonal pullout.....	15
Figure 1.9. Rainflow counting plot.....	17
Figure 1.10. CAD of the Moon's beam experimental set-up built for this study	18
Figure 1.11. Phase space of the unforced Duffing equation.....	19
Figure 1.12. Phase space warping diagram depicting the comparison of a fatigued phase space to the healthy phase space of a system.....	22
Figure 2.1. Diagram depicting the location and alignment of the specimens within the bone, where L signifies the lateral side and M signifies the medial side of the bone.....	25
Figure 2.2. Shaker system testing apparatus.....	26
Figure 2.3. Pendulum set-up	28
Figure 2.4. Photo of the shaker system testing apparatus and control table	29
Figure 2.5. Waveform generation virtual instrument graphical user interface	30
Figure 2.6. Waveform generation virtual instrument block diagram.....	31

Figure 2.7. Continuous laser step data collection virtual instrument graphical user interface.....	31
Figure 2.8. Continuous laser step data collection virtual instrument block diagram.....	32
Figure 2.9. Reaching and chaotic motion	34
Figure 3.1. Time series.....	38
Figure 3.2. Fracture Classification.....	41
Figure 3.3. Brittle break	42
Figure 3.4. Mixed mode break	42
Figure 3.5. Ductile mixed mode break.....	43
Figure 3.6. Ductile mixed mode break with osteon pullout predominant	43
Figure 3.7. Mixed mode break	44
Figure 3.8. Histograms.....	45
Figure 3.9. Phase space warping SOV and SOC graphs	50
Figure A.1. Data Logbook	61
Figure B.1. Specimen 1 (2015121701).....	62
Figure B.2. Specimen 2 (2016012002).....	62
Figure B.3. Specimen 3 (2016012101).....	63
Figure B.4. Specimen 4 (2016012701).....	63
Figure B.5. Specimen 5 (2016020401).....	63
Figure B.6. Specimen 6 (2016020501).....	64
Figure B.7. Specimen 7 (2016021201).....	64
Figure B.8. Specimen 8 (2016021401).....	64
Figure B.9. Specimen 9 (2016030401).....	65

Figure B.10. Specimen 10 (2016030701)	65
Figure C.1. Specimen 1 (2015121701) Summary	66
Figure C.2. Specimen 2 (2016012002) Summary	67
Figure C.3. Specimen 3 (201602101) Summary	68
Figure C.4. Specimen 4 (2016012701) Summary	69
Figure C.5. Specimen 5 (2016020401) Summary	70
Figure C.6. Specimen 6 (2016020501) Summary	71
Figure C.7. Specimen 7 (2016021201) Summary	72
Figure C.8. Specimen 8 (2016021401) Summary	73
Figure C.9. Specimen 9 (2016030401) Summary	74
Figure C.10. Specimen 10 (2016030701) Summary	75
Figure E.1. Shaker converter piece	97
Figure E.2. 8 inch connector arm.....	98
Figure E.3. C-frame top arm.....	99
Figure E.4. Fastener cap.....	100
Figure E.5. C-frame vertical arm	101
Figure E.6. C-frame base arm.....	102
Figure E.7. Linear guide conversion piece	103
Figure E.8. Magnet holder cap.....	104
Figure E.9. Magnet holder slider	105
Figure E.10. Pendulum metal plates	106
Figure E.11. Laser stand base	107
Figure E.12. Laser stand plate.....	108

Figure E.13. Laser stand vertical rod	109
Figure E.14. Laser stand fastener	110
Figure F.1. Amplifier specifications part 1	111
Figure F.2. Amplifier specifications part 2	112
Figure F.3. Linear guide specifications.....	114
Figure F.4. Shaker specifications.....	115
Figure G.1. Testing apparatus used in previous study	116

LIST OF TABLES

Table 3.1. Break Classification.....	44
Table 3.2. Rainflow Counting Cycles and Break Classification	48
Table 3.3. Palmgren Miner Rule Results and Break Classification.....	49
Table 3.4. Phase space warping SOV chart	51
Table F.1. Laser Vibrometer Specifications	113
Table H.1. Bill of Materials	117

NOMENCLATURE

B	Brittle fracture
BEC	Bose-Einstein condensate
D	Ductile fracture
DB	Combined ductile and brittle fracture
PMR	Palmgren-Miner rule
POD	Proper orthogonal decomposition
PSW	Phase space warping
SEM	Scanning electron microscopy
SOC	Smooth orthogonal coordinates
SOD	Smooth orthogonal decomposition
SOV	Smooth orthogonal variables
VI	Virtual instrument

ACKNOWLEDGMENTS

First, I would like to thank Dr. Kuehl and Dr. Skurla for their help and guidance throughout this study. I would also like to thank Abbey Campbell for her help and work on the previous study. Next, I would like to thank Mr. Orr for machining the parts for the system apparatus. Finally, I would like to thank my senior design teammates (Carley Fuller, Andy Hoeckel, Corey Higgins, and Colby Schaefer) for all of the effort they put into the initial design of the system apparatus and LabVIEW programs.

DEDICATION

To my wonderfully supportive family

CHAPTER ONE

Introduction

Stress Fractures

The high prevalence of stress fractures among military recruits and athletes is the main motivation behind this study. Approximately 21% of American military recruits have been diagnosed with stress fractures, and approximately 21% of competitive runners were reported as acquiring stress fractures over the period of one year [1],[2]. This injury not only occurs in runners and military recruits, it also plagues gymnasts, dancers, figure skaters, astronauts, and elderly individuals; as well as animals such as racing horses and greyhound dogs.

Stress fractures are small cracks in the bone that are caused by bone fatigue, and they can become complete fractures if left untreated. These fractures take place as a result of the bone remodeling process, which involves osteoclasts resorbing bone tissue and osteoblasts building new bone tissue, being unable to keep up with the micro-damage caused by the repetitive loading of the bone during training. Stress fractures may also result from loading bone tissue that has weakened during aging or space flight due to an imbalance in the resorption and deposition rates of the bone remodeling process. Eventually, when the natural toughening mechanisms in the bone are unable to withstand the continued loading, the bone fails. Stress fractures occur most commonly in the femur, tibia, metatarsal and tarsal bones [3],[4].

Currently, stress fractures can only be diagnosed after they are large enough to be detected using radiography, magnetic resonance imaging, or triple-phase bone scintigraphy [3]. Furthermore, to treat this injury, the patient wears a brace to restrict movement and modifies their activity level. This treatment allows the bone to remodel and heal where the fracture occurred; however, it takes approximately 12 weeks for the injury site to fully heal and for the individual to return to his or her previous activity level [3].

The purpose of this study is to develop better methodologies to monitor bone health and to predict the failure due to fatigue of the bone. Specifically, the Palmgren-Miner rule and phase space warping are tested in an effort to determine if the damage state of the bone may be detected prior to failure. If the damage state of bone may be monitored, then stress fractures may be prevented.

Hierarchical Structure of Bone

The skeletal system in humans and animals is responsible for supporting and protecting the body as well as for enabling movement via a lever system at the various joints. This system is composed of bone, ligament, tendon, and cartilage. The focus of this study is on bone tissue. In this section, the mechanical properties and structure of the bone tissue will be discussed.

Bone tissue is an anisotropic material composed of an organic matrix, water, and inorganic mineral substances, structured in such a way as to maximize its mechanical properties in the direction of loading. The hierarchical structure of bone is displayed in Figure 1.1 [5]. At the smallest level it is composed of collagen fibrils that are made up of collagen molecules and bone mineral crystals. Many collagen fibrils are then bundled together to form the collagen fiber. Collagen fibers act as reinforcing fibers for the bone

material and are arranged in a way that provides optimal strength for the bone. The orientation of the collagen fibers are developed as the bone develops and is loaded. If the collagen fibers are oriented parallel to each other, then they form lamellar bone, which is arranged in layers surrounding the Haversian canals. The fiber orientation varies from layer to layer in order to optimize the strength of the bone's sub-microstructure, and between these layers there are lacunae that contain osteocytes, bone cells that are responsible for sustaining the bone. These canals with surrounding lamella form the osteons, which are the fundamental unit of bone that runs parallel to the long axis of the bone and contains blood vessels and nerve cells.

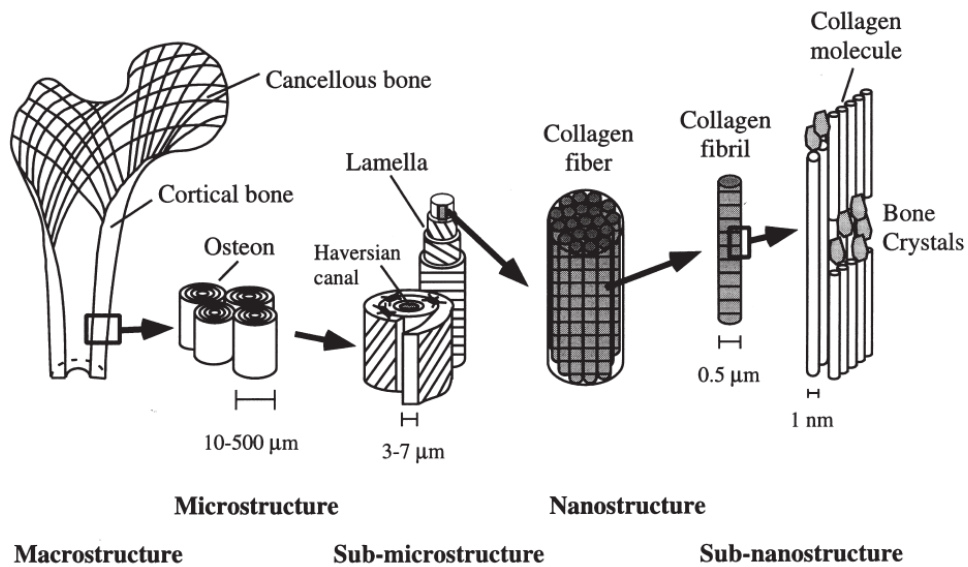


Figure 1.1. Hierarchical structure of bone [5]. Reprinted from Medical Engineering & Physics, 20, Jae-Young Rho, Liisa Kuhn-Spearing, Peter Zioupos, Mechanical properties and the hierarchical structure of bone, 92-102, Copyright 1998, with permission from Elsevier.

Woven bone, unlike lamellar bone, consists of randomly oriented collagen fibers. Due to its structural arrangement, it is weaker than lamellar bone. It is found in immature bone at sites where fractures are healing and between layers of lamellar bone in another

type of bone called lamellar bone. The layers of lamellar bone and woven bone are oriented in rings around the bone's long axis and allow for rapid growth [6], which is why lamellar bone is generally present in large animals like horses and cows.

Cortical and cancellous bone may be composed of lamellar, woven, or lamellar bone. Cortical bone forms the diaphysis of long bones and the encasement about the metaphyses and epiphyses [7]. This particular type of bone is also known as compact bone since it is not porous; the only holes are those of the lacunae and blood channels. Due to its make up, cortical bone is hard and resistant to bending. Cancellous bone, on the other hand, is highly porous and can be found in the epiphyses and metaphyses of long bones. Since this study was performed solely on cortical bone, cortical bone is the only type that will be further discussed.

Properties of Bone

Bone demonstrates elastic, plastic, and viscoelastic properties. In Figure 1.2 a load-deformation curve is depicted for a tensile test that was performed on bovine femoral bone. It is comparable to a stress-strain curve where the elastic region is the region on the graph leading up to point A. In this region the bone can be loaded and unloaded without experiencing permanent deformation, thus it may undergo an infinite number of cycles to failure. Around 1% elastic strain, the yield point in the material occurs. Any strain experienced beyond this point causes the material to enter the plastic region. In the plastic region, the bone will not return to its original shape after the load has been removed, but it can absorb as much as 6 times the amount of energy that can be absorbed in the elastic region. It is believed this may be due to the coupling of the fibrous matrix and the mineral crystals in the bone. For instance, the mineral crystals may plastically deform or fracture

while the matrix is experiencing elastic or plastic deformation [6]. However, when the strain reaches approximately 4%, the bone will fracture [8].

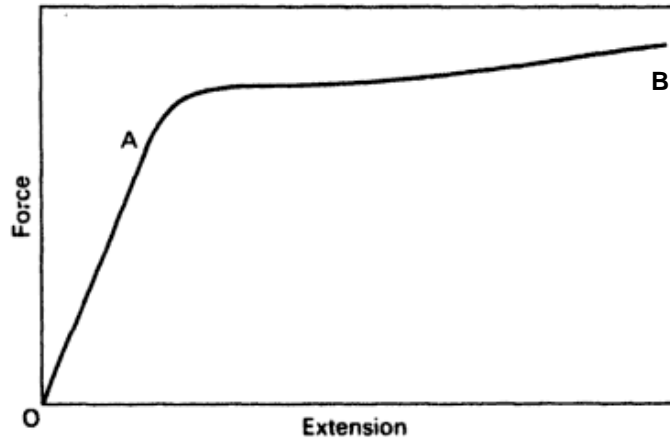


Figure 1.2. Load-deformation curve of bovine femoral cortical bone [6],[8]: Between points O and A there are an infinite number of cycles to failure while at point B there is only 1 cycle to failure. Reproduced with permission from S.A. Wainwright, Mechanical Design in Organisms. Copyright 1982, Princeton University Press.

Bone tissue, also displays viscoelastic properties. When a force is applied to bone and causes deformation, the material will display viscous characteristics along with its elastic properties. Part of the viscous characteristics is that the bone structure is allowed to change with time. This phenomenon means there is not a unique modulus of elasticity or fracture stress, but rather these properties need to be defined with respect to the strain rate or time over which the load was applied. This can be seen more clearly in the data presented in Figure 1.3, which depicts how ultimate stress, Young's modulus, and ultimate tensile strain of bone are affected by various applied strain rates. An increase in the strain rate causes the ultimate stress to increase, the Young's modulus to increase, and the ultimate tensile strain to decrease [6].

Effects on bone of different strain rates. σ_t , ultimate stress
(MN m^{-2}); ϵ_t , ultimate tensile strain; E , Young's modulus (GN m^{-2}).

Strain rate in s^{-1}	Loading mode	σ_t	E	ϵ_t	Reference	
0.01	(man)	Tension	125	17.0	0.033	1
0.1		Tension	133	17.4	0.038	1
1		Tension	166	21.4	0.018	1
0.001	(ox)	Compression	179	18.9	0.018	2
0.01		Compression	210	19.6	0.018	2
0.1		Compression	235	24.6	0.018	2
1		Compression	255	28.1	0.012	2

References: (1) Burstein and Reilly, unpublished; (2) McELHENEY (1966).

Figure 1.3. Effect of strain rate in bone [6]. Reproduced with permission from S.A. Wainwright, Mechanical Design in Organisms. Copyright 1982, Princeton University Press.

The Young's modulus and strength of the cortical bone are also dependent upon the direction of the loading force. Since bone is an anisotropic and inhomogeneous material, it is stronger in some directions than others. Figure 1.4 shows how the loading mode affects the ultimate strength and modulus of elasticity of the human femoral cortical bone [7]. As can be seen in the tables presented in the figure, cortical bone is stronger in compression than it is in tension. This is also apparent in bending tests, similar to engineering and naturally occurring composite materials, bone tends to break on the side that is in tension rather than compression.

Another factor that affects all of these properties is the physical state of the bone. Figure 1.5 depicts the results of 4-point bend tests performed on hydrated and dehydrated bovine cortical bone in a load versus displacement graph. As can be seen in the figure, hydrated bone is much stronger and tougher than dehydrated bone [9].

Strength of femoral cortical bone^a

Loading mode	Ultimate strength (MPa)
Longitudinal	
Tension	133
Compression	193
Shear	68
Transverse	
Tension	51
Compression	133

Modulus of femoral cortical bone^a

Longitudinal	17.0 GPa
Transverse	11.5 GPa
Shear	3.3 GPa

^aAge span of population 19–80 years.

1GPa (gigapascal) = 1,000 MPa. From Hayes and Gerhart (61), with permission. Mean values from Reilly and Burstein (116b), with permission.

Figure 1.4. Strength and modulus of human cortical bone [7]. Reproduced with permission from Van C. Mow, Wilson C. Hayes, Basic Orthopaedic Biomaterials. Copyright 1997, Lippincott-Raven Publishers.

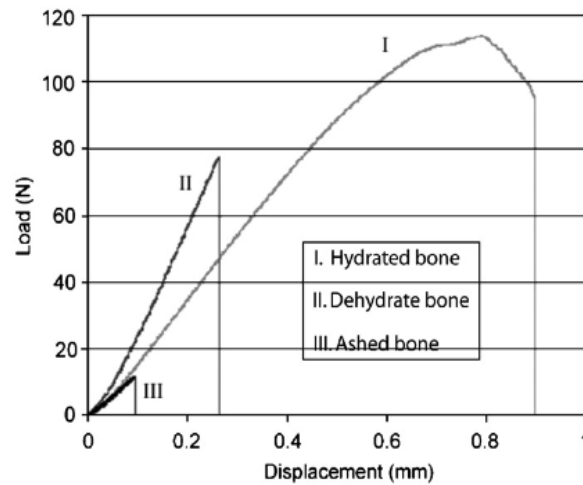


Figure 1.5. Four-point bend load versus displacement curves for hydrated and dehydrated bovine bone [9]. Reprinted from Journal of Biomechanics, 41, J. Yan, A. Daga, R. Kumar, J. Mecholsky, Fracture toughness and work of fracture of hydrated dehydrated and ashed bovine bone, 1929-1936, Copyright 2008, with permission from Elsevier.

As humans and other mammals age, the elastic modulus, toughness, and strength of mature bone tend to decrease. In humans, between the ages of 20 and 90 years, these properties decrease by approximately 2% every ten years [7]. Thus bone fractures are a concern in the elderly population, particularly in osteoporotic, post-menopausal women.

Osteoporosis can occur in men and women; however, it generally progresses more rapidly in postmenopausal women. This condition is due to an increase in bone resorption and decrease in the deposition of bone during the remodeling process, which causes the bone to progressively become weaker and the fracture risk to increase [7]. Remodeling continually occurs in bone tissue in order to keep the bone strong, its main purpose is to repair bone and to adapt the tissue to applied mechanical loads. In healthy bone tissue, resorption and deposition are coupled and are controlled by hormones and proteins that are secreted by bone and bone marrow cells [10]. However, as people age, hormone production in the body and other factors, such as physical activity level, change. These changes can cause more bone to be broken down than to be built up.

Additionally, astronauts who spend a prolonged period of time in a microgravity environment are at an increased risk of bone fracture upon returning to an environment with gravity. This is due to disuse osteoporosis which is similar to what postmenopausal osteoporotic individuals experience, but the bone loss in space is approximately 10 times greater and is due to a significantly decreased level of mechanical loading on the tissue [11]. At the end of a 4-6 month long space flight, the percentage of total bone loss is about 0-3% with the largest percentage of bone loss in the weight bearing bones at 0-20% [11]–[14]. Lang et al. performed a study on astronauts after 4-6 months in space and found that

1 year after the space flight, the bending and compressive strength of the bone were still approximately 10% less than the preflight strength (Figure 1.6) [14].

TOTAL FEMUR vBMD, MASS, AND VOLUME MEASURED PREFLIGHT (PrFL), POSTFLIGHT (PoFL), AND 1 YEAR AFTER MISSION, FOLLOWED BY THE PERCENTAGE CHANGES MEASURED DURING THE FLIGHT AND RECOVERY PERIODS AND THE RATIO OF 1 YEAR TO PrFL VALUES

		<i>PrFL</i>	<i>PoFL</i>	<i>R12</i>	$\Delta(\%)$ <i>Flight</i>	$\Delta(\%)$ <i>Recovery</i>	<i>Ratio (R + 12/PrFL)</i>
Total vBMD (g/cm ³)	Mean	0.332	0.297	0.309	-10.40	4.40	0.93
	Median	0.325	0.297	0.308	-9.72	4.72	0.93
	<i>p</i> value				<0.001	0.02	<0.001
Trabecular vBMD (g/cm ³)	Mean	0.145	0.124	0.132	-14.40	6.70	0.91
	SD	0.026	0.027	0.026	6.30	5.90	0.05
	<i>p</i> value				<0.001	<0.001	<0.001
Cortical vBMD (g/cm ³)	Mean	0.539	0.521	0.523	-3.40	0.60	0.97
	SD	0.037	0.035	0.033	3.60	3.20	0.03
	<i>p</i> value				<0.001	0.38	0.02
Total mass (g)	Mean	35.182	30.772	34.397	-11.10	12.20	0.99
	SD	7.342	4.686	5.686	11.20	11.80	0.12
	<i>p</i> value				<0.001	<0.001	0.560
Cortical mass (g)	Mean	25.502	22.000	24.547	-12.10	12.40	0.98
	SD	5.668	3.675	4.171	12.20	14.70	0.13
	<i>p</i> value				<0.001	0.010	0.320
Total volume (cm ³)	Mean	106.322	104.242	112.008	-0.70	7.20	1.06
	SD	19.803	14.678	19.234	10.10	7.30	0.11
	<i>p</i> value				0.710	<0.001	0.070
Cortical volume (cm ³)	Mean	47.011	42.091	46.804	-9.2	11.5	1.01
	SD	8.447	5.250	6.957	10.8	12.2	0.12
	<i>p</i> value				0.010	<0.001	0.710

p values denote the statistical significance of the percentage changes and the significance of the difference between preflight and 1-year values.

Figure 1.6. Percentage of bone loss and recovery in the femur [14]. Reprinted from Journal of Bone and Mineral Research, 21, Thomas F. Lang, Adrian D. Leblanc, Harlan J. Evans, Ying Lu, Adaptation of the Proximal Femur to Skeletal Reloading After Long-Duration Spaceflight, 1224-1230, Copyright 2006, with permission from John Wiley and Sons.

Human long bones and bovine bone have significantly different properties because human long bones are lamellar bone and bovine long bones are laminar bone [15]. However, because human bone is expensive, requires stringent record keeping, and must be returned to the source at the end of the study, a surrogate material is commonly used in the preliminary studies. One of the commonly used surrogates is bovine bone, which is relatively inexpensive, has fewer regulatory issues, and is easy to acquire [16]–[19].

Constitutive Fatigue Model

Many researchers have applied a variety of methods to the study of bone fatigue with the intent to develop an accurate constitutive fatigue model. It has been determined that bone reacts to applied stress and strain in a similar manner as fiber-reinforced composite materials [20]–[25]. Varvani-Farahani et al. related the structure and mechanical properties of human cortical bone to an engineered composite [26]. In bone, the osteons, which run in the direction of the bone's long axis, act as the reinforcing fibers and carry a large portion of the applied load, and are surrounded by the interstitial bone matrix tissue. The weak interfaces in the fiber-reinforced composites are comparable to the cement lines present between the osteons in bone tissue. Additionally, since the compositions are analogous, they have comparable mechanical properties. For instance, both materials are strongest when loaded parallel to the fibers. They also experience a similar 3-phase process of fatigue under axial cyclic loading [15], [26], [27].

Phase 1

In the first phase, the material's response is in the elastic region. In this region the bone experiences reversible deformation and a decline in stiffness as it develops and repairs microcracks in the interstitial bone [26]–[28]. Studies have shown that, as a result of osteocytic apoptosis, microcracks start their own healing process and are in steady state with the bone's natural repair and remodeling systems [29]–[32]. Also, it is believed that this type of microdamage is present in healthy bone and helps dissipate the energy imparted upon the bone during the loading process [33].

Phase 2

The second phase begins after the bone reaches its yield point at the end of the elastic region. In the second phase, the material is in the plastic region, its stiffness decreases at a slower rate than it did in the elastic region, and it becomes permanently damaged while maintaining structural integrity [27]. As the stiffness continues to decrease in this phase, the toughness increases and thus the amount of energy required for a crack to propagate through the material increases. Since the cement lines are the weakest part of the bone, a large portion of the damage occurs there [26]. H. S. Gupta and P. Zioupos presented the notion that the propagation of a crack is more significant than the initiation, because the structure of bone does not work to prevent damage, but rather to slow the rate of the crack growth [27]. If the crack's growth rate is slower than the rate of the body's repair mechanisms, then the bone heals. If the crack's growth rate is much faster than the body can repair the bone, then the bone may experience a catastrophic failure. A significant amount of research has been conducted in order to discover what takes place during this phase, and it has been determined that multiple mechanisms are responsible for the observed behavior. A few examples of the mechanisms can be seen in Figure 1.7.

There are two main theories presented by Gupta and Zioupos regarding the propagation of cracks in bone [27]. The first theory is the stress-based method that considers the stress intensity factor. It claims that a crack begins in the material when the critical stress value is reached or surpassed at the tip of the crack, and the microstructure of the bone is largely responsible for how the cracks propagate. Additionally, a study indicated that the initiation point of the crack and the orientation of the fibrils in the bone directly affect the direction of the crack's propagation [35]. The second theory is based on

energy; in particular, the critical amount of energy that leads to the fracture of the specimen is determined by the critical strain energy release rate and the work to fracture of the specimen. According to an article by Burr [33], a material's fracture resistance is determined by its ability to absorb energy. The more energy it is able to absorb, the less likely it is to fracture. In bone, the cement lines are weak and thus are more likely to fail. This increases the fracture resistance of bone because these interlamellar surfaces are able to absorb energy and redirect the main crack. As a result, a catastrophic failure is mitigated (See Figure 1.7 (a)).

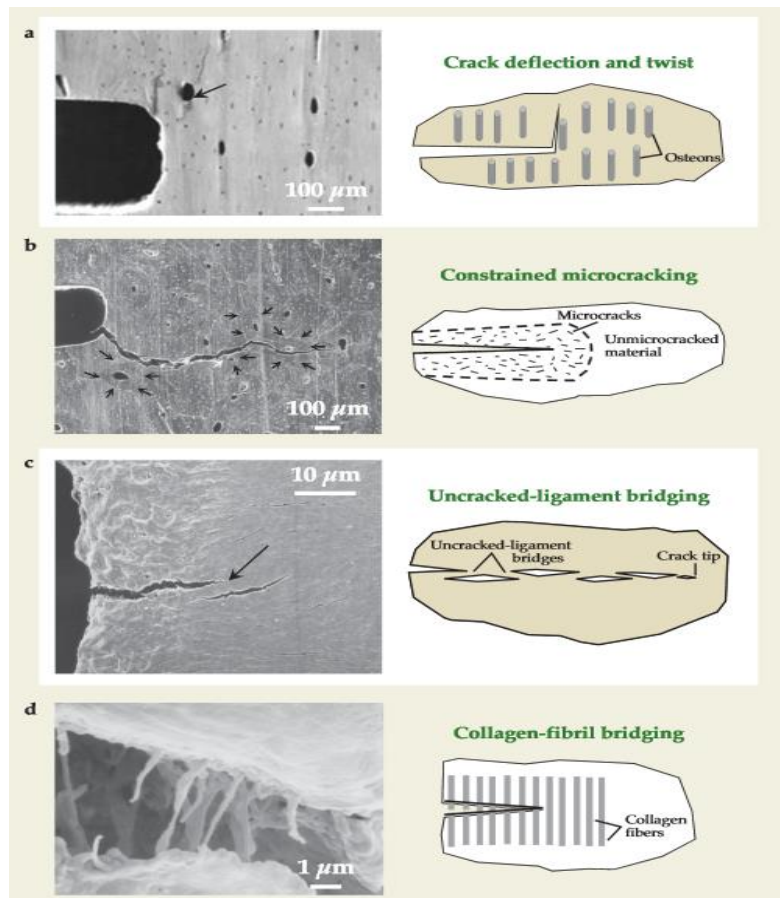


Figure 1.7. Bone toughening mechanisms: (a-b) intrinsic toughening, (c-d) extrinsic toughening [34]. Reproduced with permission from R.O. Ritchie, M.J. Buehler, and P. Hansma, *Physics Today*, 62(6), 41 (2009), Copyright 2009, American Institute of Physics.

Microdamage has been found to be a common mechanism to minimize crack growth. It accomplishes this by dissipating energy within the bone and can be found in healthy bone as well as around the initiation site of the crack to prevent crack growth (See Figure 1.7 (b)) [36]. However, as a whole, microdamage weakens the bone's mechanical properties, which can cause susceptibility to fracture. Microdamage is composed of microcracks that take one of two forms in cortical bone, are specific to their incitement, location, development, and restoration [33]. The first and most common form are linear microcracks. Linear microcracks are the result of compressive stresses and are present where the material has deformed. The other form is known as diffuse microdamage, which are groupings of microcracks that are the result of tensile loads. Diffuse microdamage tends to merge, grow, and nucleate as the microcracks divert energy away from the main crack [37].

Another mechanism that increases bone's resistance to fracture is known as crack bridging. Collagen fibrils span the width of propagating microcracks [38]–[43]. There are two types of this mechanism. One type is collagen-fibril bridging (See Figure 1.7 (d)), which does not have a large impact on preventing crack propagation. The other type is uncracked-ligament bridging (See Figure 1.7 (c)), which helps prevent crack growth and propagation because it can withstand significant loads.

Another theory, the 'sacrificial bond' theory, has to do with the reforming, yielding, and breaking of bonds within the organic molecules in the bone [37], [44], [45]. These 'sacrificial bonds' toughen the bone by absorbing large quantities of energy. However, not all bonds within the bone material can play the role of the 'sacrificial bond'. Additional studies [46]–[48] by Gupta et al. demonstrated that the breaking of certain bonds within

the bone can lead to fracture. The breaking of ionic bonds within the bone material could result in irreversible deformation because it causes decohesion within and among the fibrils after the yield point [46]–[48]. The particular bonds that are broken here are solely within the collagen fibrils [48].

Phase 3

In the third phase, failure of the material occurs. The bone material has accumulated damage in both Phase 1 and Phase 2. The osteons are left to withstand the load applied to the bone. The bone is no longer able to adequately repair itself or absorb energy. The remaining strength and stiffness are rapidly diminished. As a result, the osteons debond and the crack rapidly grows and causes the bone to fail.

Some studies have observed osteon pullout (See Figure 1.8) during this phase; however, it does not always occur [49], [50]. Osteon pullout is due to shear failure around the osteon cement lines, which are more viscoelastic than the surrounding bone because they have a different mineral and protein composition. In one study [50] by Hiller et al., it was found that osteon pullout occurred when the bone was in tension and had under-gone 4-point bend fatigue loading. When the bone was monotonically loaded, osteon pullout was not observed. The occurrence of osteon pullout under fatigue loading may be due to the cement lines accumulating shear damage during the transverse crack initiation and propagation. Furthermore, the amount of osteon pullout was dependent upon the region of the bone, which may be due to the collagen fiber orientation within the bone [50].



Scanning electron micrograph of an osteon on the transverse fracture surface of a cyclically loaded dorsal specimen. Disruption of interlamellar and cement line interfaces reveals concentric lamellae and the outer osteon boundary of “pulled out” osteons.

Figure 1.8. Osteonal pullout [50]. Reprinted from Journal of Orthopaedic Research, L.P. Hiller, S.M. Stover, V.A. Gibson, J.C. Gibeling, C.S. Prater, S.J. Hazelwood, O.C. Yeh, R.B. Martin, Osteon pullout in the equine third metacarpal bone: Effects of ex vivo fatigue, 8, Copyright 2003, with permission from John Wiley and Sons.

Estimation of Fatigue Limit

The maximum stress a material can repeatedly endure without fracturing is known as the fatigue limit of the material. In a laboratory setting, the fatigue limit can be predicted with the Palmgren-Miner rule using results of cyclic amplitude loading or variable amplitude loading methods [51]–[54]. The fatigue limit can also be estimated with phase space warping using fast-time measurements to reconstruct the slow-time dynamics [55]–[59].

Palmgren-Miner Rule

The Palmgren-Miner rule (PMR) is a cumulative damage model that is commonly used to estimate the fatigue limit of a material. PMR assumes the rate of damage accumulation is constant for a particular stress level and the material's history and loading pattern are not consequential to how the material fails [60]. As was shown in another study [61] by McEvily et al., in reality, the damage accumulation for a particular stress level varies depending on the development and growth of cracks within the material. Additionally, to accurately predict the fatigue life, the fatigue limit stress and the critical stress need to be considered [61]. Although the PMR does not take these things into account, it is widely used because it is simple and one of the best fatigue life prediction methods to date [62]. The PMR damage model is presented in equation 1.1, where D_p is the damage parameter, n_i is the number of cycles, and N_i is the total number of cycles the material can experience prior to failure. This model states that the damage in the material is equal to the summation of the ratio of the number of cycles at a particular amplitude to the total number of cycles to failure at that amplitude, and the material will fracture when the damage parameter is equal to one.

$$D_p = \sum_{i=1}^k \frac{n_i}{N_i} \quad (1.1)$$

When it is difficult to see the cycles, the rainflow counting method (RCM) is used to determine the cycle count at each amplitude [63]. In fact, this method is often used with the PMR in fatigue tests [64]. RCM (See Figure 1.9) can be visualized best by thinking of water flowing down a structure. The structure, in this case, is the plot of strain versus time with the cycles of interest. First, the plot is rotated 90 degrees clockwise such that the time axis runs vertically. The positive and negative strains are due to tensile and compressive

loading, respectively. Each trough is thought of as a water source, and the water flows down the peaks until it comes to a larger trough, encounters the flow from above, or reaches the end of the recorded time for the plot (blue lines in Figure 1.9). Each of these flows is counted as a half cycle whose magnitude is the difference between the values of the dependent variable (strain in Figure 1.9) at the start and end of the flow. Finally, the total cycle count is the sum of the half-cycle pairs [65].

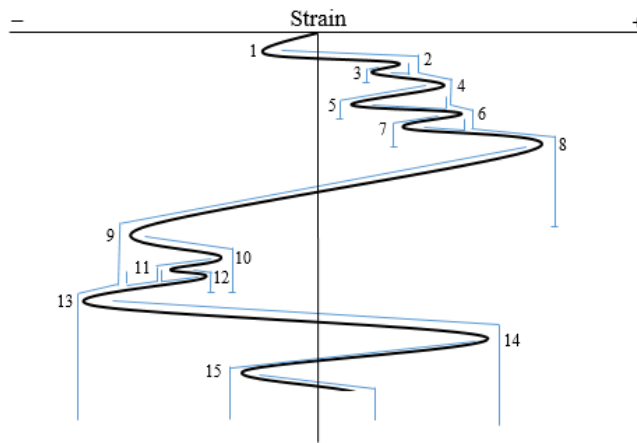


Figure 1.9. Rainflow counting plot [65].

Phase Space Warping

Although slowly developing processes in a system may be difficult to directly observe, they affect the directly observable fast-time processes and ultimately lead to the failure of the system. In order to better study the slow-time dynamics of fatigue damage in a material, Dr. Chelidze with the University of Rhode Island developed an experimental method and mathematical model to analyze slow time processes using fast-time, vibration, measurements [55]–[59], [66]. The experimental method used a testing apparatus that was comprised of a shaker connected to a C-Frame that held the specimen clamped between 2 metal plates, creating a long pendulum, over 2 magnets. A similar apparatus is used in this

study; see Figure 1.10. The mathematical model that was developed employs dynamical systems and a process known as phase space warping in order to predict the fatigue life of a material.

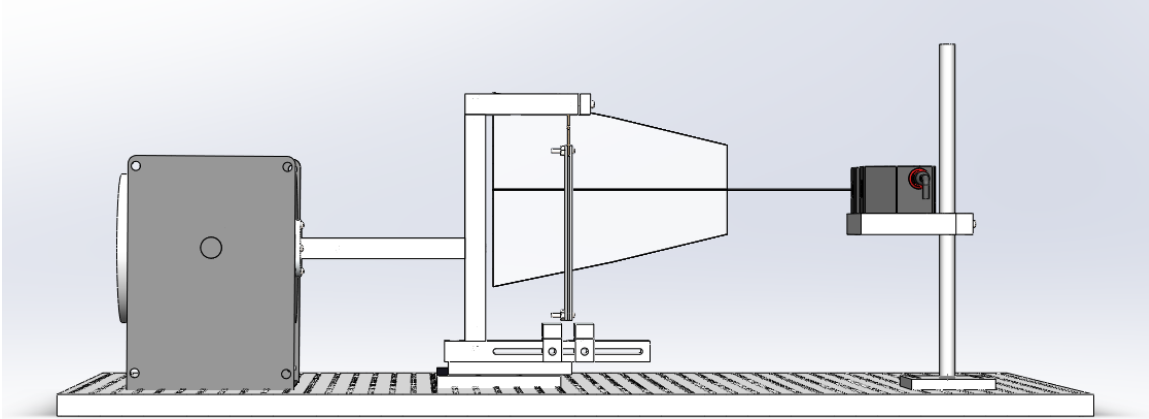


Figure 1.10. CAD of the Moon's beam experimental set-up built for this study.

The Duffing equation models the vibrating beam system used in this study well. It is a mathematical model for a pendulum oscillating in a double potential well [67]. In the forced Duffing equation (equation 1.2), γ , α , and β are positive real constants. The displacement of the pendulum, the directly observable fast-time dynamics, is represented by x , and the forcing is described by the right hand side of the equation where f is the amplitude, ω is frequency, and t is time. Figure 1.11 portrays the phase space for the unforced Duffing equation, which is similar to the phase space of the forced Duffing equation; therefore, it is shown here for clarity. In Figure 1.11, 2 important points at $(-3, 0)$ and $(3, 0)$ are the 2 stable fixed points at the bottom of potential wells, which are formed by the magnets in the experimental set up. At $(0, 0)$ is an unstable position at which the pendulum will fall into either the right or the left potential well. One way to picture these points in the experiment is by envisioning 2 valleys separated by a hill and a freely rolling

ball. If the ball is set on the hill, it will either roll into the left or the right valley. Once in the valley the ball will stay in the valley unless enough energy is added into the system to roll the ball to the top of the hill. At this point, the ball will either roll into the next valley or fall back into the one it was in. In this analogy, the valleys represent the potential wells, the hill is the unstable position, and the ball is the pendulum. If dissipation of energy were included, the stable fixed points would become spiral-attracting points to which the ball would tend to roll.

$$\ddot{x} + \gamma\dot{x} - \alpha x + \beta x^3 = f \sin(\omega t) \quad (1.2)$$

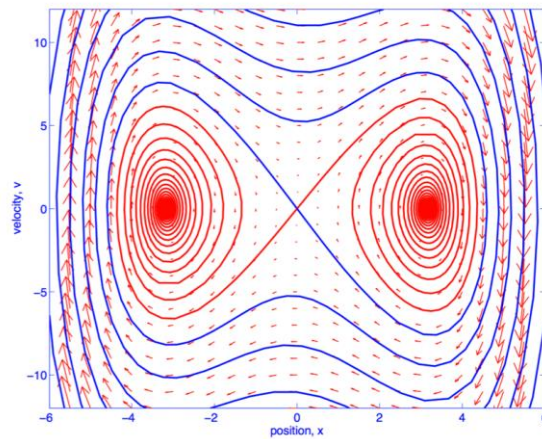


Figure 1.11. Phase space of the unforced Duffing equation.

From the relationship between the fast and the slow-time dynamics and equation 1.2, it is found that the system can be modeled using the hierarchical dynamical systems shown in equations 1.3 through 1.5, where \mathbf{x} is the directly observable fast-time variable, $\boldsymbol{\phi}$ is the slow-time variable, $\boldsymbol{\mu}$ is the vector of parameters, which are a function of the slow-time variable, t is time, ϵ is a small rate constant that is greater than zero but much less than one and is called the time-scale separation between the fast and slow dynamics, and y is the scalar measurement determined by the smooth function h of the fast-time variable.

These equations reveal ϕ , the slow-time variable, can develop and change on a time scale that is slower than the fast time scale that is directly observed.

$$\dot{x} = f(x, \mu(\phi), t) \quad (1.3)$$

$$\dot{\phi} = \epsilon g(x, \phi) \quad (1.4)$$

$$y = h(x) \quad (1.5)$$

To capture the fast and the slow-time dynamics, an experiment needs to be run for a long period of time, and measurements need to be collected at a high sampling rate, which leads to large data sets. In order to analyze the data, it is broken up into intermediate time scales where the fast-time dynamics are quasi-stationary and are modeled as feature vectors. The quasi-stationary fast-time dynamics can be characterized using a local linear model, which approximates a non-linear function with piece-wise linear models. The local linear model is used to reconstruct the fast-time phase space by delay coordinate embedding. This method uses time-delayed values of the scalar measurements to reconstruct the phase space representation of the fast-time dynamics, and from it a feature vector is ascertained.

Delay coordinate embedding requires the delay time. The delay time can be determined via average mutual information, which is a way to measure the dependence between variables [55], [57]–[59]. Specifically, the average mutual information between 2 variables is the negative of the entropy of the variables' joint density function with respect to their marginals' product. The average mutual information between all measurement sets is given by equation 1.6, in which $p(x, y)$ is the joint density function while $p(x)$ and $p(y)$ are the marginals [68]. When this function is plotted, the independent variable value of the first minimum is the delay time.

$$I(X, Y) = \iint p(x, y) \ln \frac{p(x, y)}{p(x)p(y)} dx dy \quad (1.6)$$

Delay coordinate embedding also requires knowledge of the minimum dimension regression vector, also known as the embedding dimension, which can be determined via the method of false nearest neighbors [55], [57]–[59]. In this method, regression vectors are chosen that are close to each other in the regressor space. These regression vectors should have outputs that are close to each other. However, if the dimension of the regression vector is too small, then the projection onto the regressor space may have outputs that appear to be close together when they are not truly close. These are called false neighbors. The true and false neighbors are determined via a ratio test where the outputs are compared to the regression vectors. If the value of the quotient is significantly large or small, then the neighbors are considered false or true, respectively. The minimum dimension of the regression vector required to recreate the phase space is the one with the number of false neighbors equal to 0 [69].

The process of delay coordinate embedding is repeated for each of the intermediate time scales. The shifting of the feature vectors is then analyzed to see if there are changes that are potentially due to damage [59]. The phase space warping function is the difference between the feature vector for the undamaged system and the feature vector for the fatigued system, it shows where the warping is taking place (see Figure 1.12). Then, all of the phase space warping functions are concatenated to create the tracking matrix [56]–[59].

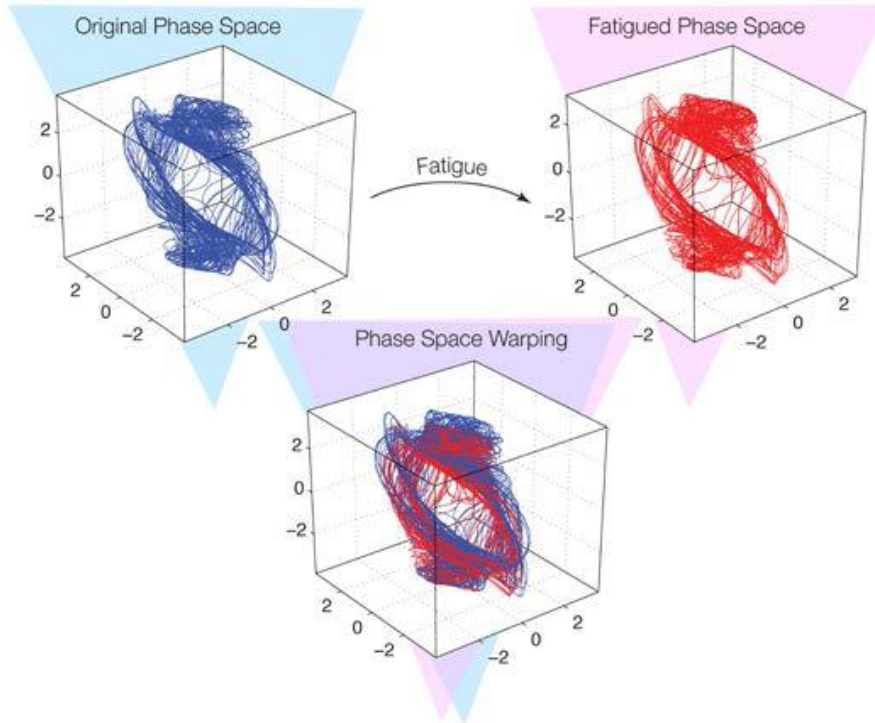


Figure 1.12. Phase space warping diagram depicting the comparison of a fatigued phase space to the healthy phase space of a system. Printed with permission from Dr. David Chelidze, University of Rhode Island.

In order to find the fatigue modes, smooth orthogonal decomposition (SOD) is performed on the tracking matrix. SOD is employed because it handles the bifurcations that are present in the fast-time dynamics better than proper orthogonal decomposition (POD). Both POD and SOD show the statistical modes which best account for variance amplitude, but SOD also makes the signal as smooth in time as is possible. The main difference between SOD and POD is that POD uses the maximization problem stated in equation 1.7, while SOD uses the maximization problem stated in equation 1.8. In these equations X represents the tracking matrix and V is the temporal derivative of X . The tracking matrix is projected onto the SOD modes to find the slow time damage phase space, which is then reconstructed using the SOD coordinates [70]. Finally, analysis of these slow

time dynamics can be used to identify the dynamics of fatigue as was shown in the papers by Chelidze et al. [55]–[59].

$$\max_{\phi} \|X\phi\| \text{ subject to } \|\phi\| = 1 \quad (1.7)$$

$$\max_{\phi} \|X\phi\| \text{ subject to } \min_{\phi} \|V\phi\| \quad (1.8)$$

Using the methodology they developed, Chelidze and his team successfully ran tests on steel to detect fatigue damage. Specifically, they were able to predict failures in a stationary operating environment [55]–[59]. In reality the operating environment is not stationary, but this is an assumption that can be made because the variation in the environment over the observation period is negligible for the experiment type being run [59].

CHAPTER TWO

Materials and Methods

Specimen Preparation

Bovine femurs, purchased from Animal Technologies, Inc. (Tyler, TX) were used as the test specimens. Since the bones were collected from a commercial slaughter house, the gender, age, and health of the cows from which the bones were harvested were unknown. However, it was known that the cows were between the ages of 8 and 30 months old [71]. To prepare the test specimen, the soft tissues on the outer surface of the bone were removed using a large scalpel and forceps. The epiphyses were cut off using a Craftsman band saw. The diaphysis was cut into medial and lateral halves. In order to decrease some of the variability among specimens, the medial side was discarded. Only specimens cut from the lateral side were used in this study. The bone marrow was removed and discarded. The lateral portion of the diaphysis was cut along the long axis of the bone into 3 sections using the band saw. Each section was then cut into 1-2 specimens that were approximately 2-3 inches long, 0.1 inches thick, and 0.5 inches wide, using a Buehler IsoMet™ 1000 precision saw with an IsoMet™ 15 LC diamond wafering blade. To prevent the bone from becoming burnt as it was being cut, a solution that was 1 part Buehler Cool 2 cutting fluid to 33 parts water was used as the lubricant for the saw. Figure 2.1 depicts the locations from which the specimens they were cut from the bone.

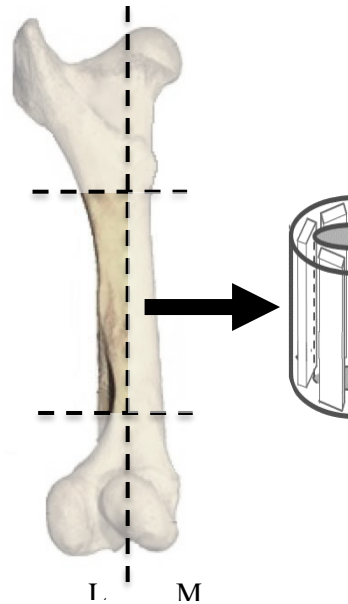


Figure 2.1. Diagram depicting the location and alignment of the specimens within the bone, where L signifies the lateral side and M signifies the medial side of the bone.

Each specimen was notched, to reduce the width of the specimen, on both sides using a triangular file. The width between the notches was 0.32 – 0.35 inches, and the notches were located at least 1.25 inches down from the top of the specimen. These notches allowed for the stress to be concentrated in the center of the test section and caused the bone to fail at the specified location. An 11/64-inch hole was drilled approximately 0.625 inches down from the notches on the specimen with a Central Machinery 13” drill press. This hole enabled the steel plates that form the bottom of the pendulum to be attached to the bone with a nut and bolt, as is shown in Figure 2.3.

If the specimens were to be tested within one week of preparation they were wrapped in gauze, soaked in a 0.9% saline solution, placed in a Ziplock™ bag, and stored in a compact refrigerator (Kenmore, Sears Roebuck and Co., Chicago, IL). If the specimens were not going to be used within the week, they were placed in a commercial freezer at -20°C (Artic Air, WCI/Frigidaire Co., Eden Prairie, MN). Upon removal from the freezer,

specimens were thawed in the refrigerator at least 24 hours prior to testing. Seven hours prior to testing, the specimen was set out in the open air to dry. The drying process was determined from prior experiments that revealed the resonant frequency of the specimen stopped shifting after 7 hours of being exposed to the lab air.

Testing Apparatus

Hardware

The testing system used in this research was modeled after the system used by Dr. Chelidze and his team at the University of Rhode Island. The experimental set-up is called Moon's beam, which is mathematically described by the Duffing equation [55], [56]. A CAD model of the apparatus is provided in Figure 2.2. The apparatus was designed to fatigue bone specimens in a chaotic manner because bone is fatigued *in vivo* in neither a purely cyclic nor cyclically variable manner.

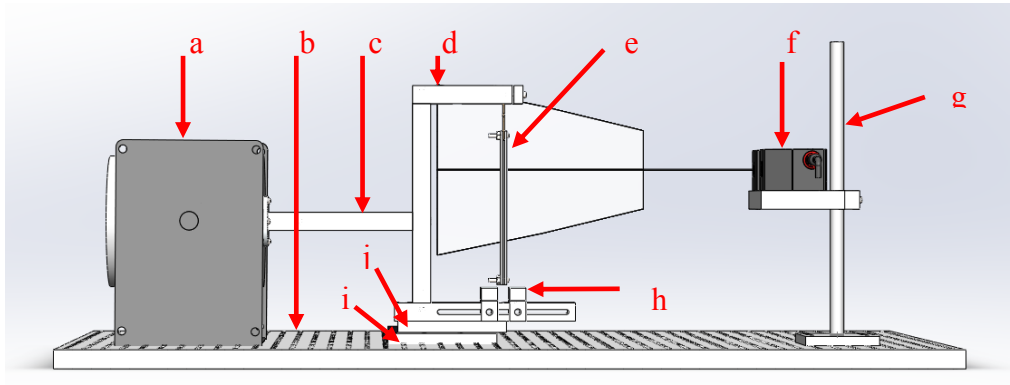


Figure 2.2. Shaker system testing apparatus: (a) VTS – 100 shaker (b) Nexus breadboard (c) 8 in aluminum connector piece (d) aluminum C – frame (e) specimen pendulum (f) LJ – V7300 Keyence laser vibrometer (g) aluminum laser stand (h) Neodymium rare earth magnets (i) aluminum linear guide conversion piece (j) AC – NMS – 4 linear guide.

A custom C-frame was machined from aluminum (see Appendix E for CAD drawings). It was mounted to an AC-NMS-4 linear guide (Del-Tron Precision, Inc., Bethel, CT) in order to minimize friction, refine the motion, and minimize wear and tear on the shaker. The shaker was a VTS-100 electromagnetic shaker (Vibration Test Systems, Aurora, Ohio) that produced sinusoidal translational motion. The shaker and the aluminum C-frame were connected with an 8 inch long aluminum bar. This length was chosen in order to have the maximum amount of distance and thus least magnetic interaction between the pendulum and the electromagnetic shaker. Separate from this apparatus, a laser vibrometer (LJ-V7300, Keyence, Elmwood Park, NJ) was placed on a stand facing the shaker system. The laser vibrometer recorded the displacement of the pendulum throughout the fatigue test. The entire system was mounted onto a vibration isolation table (Nexus Breadboard, Thorlabs, Newton, NJ) in order to isolate the system from any external vibrations.

Next, consider the pendulum. The base of the specimen was clamped between two rigid steel plates, which created a long magnetic pendulum (Figure 2.3). The top of the specimen was then clamped into the C-frame. Due to the gauge length of the test section, thickness of the specimen, rigidity of the steel plates, and top clamp, higher order modes of oscillation were prevented from contaminating the tests. Viewing the profile data and directly observing the test as it was being conducted confirmed this.

The pendulum hung above two rare-earth permanent magnets (5/8" x 5/8" Cylinders - Neodymium Rare Earth Magnets, Apex Magnets, Petersburg, WV), which were attached to the C-frame using an outer casing, saddle, and bolt, as shown in Figure 2.2. These permanent magnets were responsible for inducing a double potential well for

the pendulum. During the test, the motion of the pendulum delivered the bending load to the specimen. The double potential well provided harmonic, variable, or chaotic forcing depending on the parameters, whereas a single potential well would have provided only harmonic forcing.

To ensure the amplitude of the swings corresponded with the forcing amplitudes tested in the prior study, pilot experiments were performed to determine the optimum forcing frequency and spacing of the magnets. When the pendulum swung over both of the potential wells the tests were predominately in the large swing phase and resulted in a brittle break. When the pendulum oscillated over one potential well the tests were predominately in the small swing phase and resulted in a ductile break. Based off of this relationship, it was determined that the two experiments could be related to each other. The large swing phase in the current study corresponds to the large amplitude in the prior study, and the small swing phase in the current study corresponds to the small amplitude in the prior study. It was assumed that the offset stress present in the small swing phase did not play a major role in the fatigue process. and that Tests were run to confirm the off-set stress assumption with inconclusive results, likely due to the variability of the bone specimens.

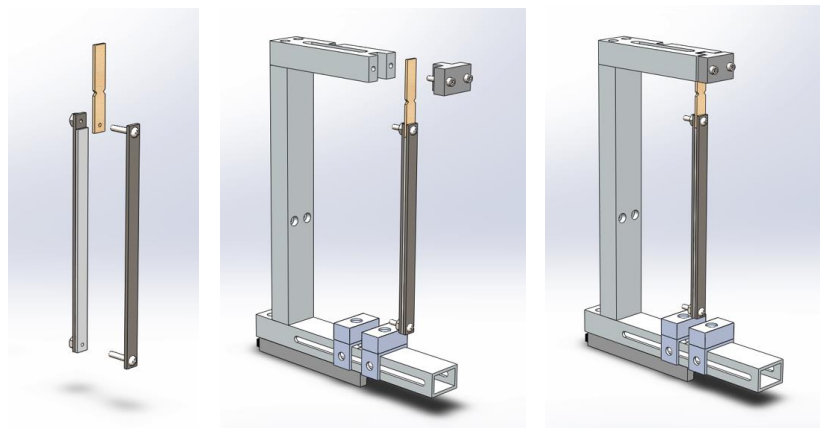


Figure 2.3. Pendulum set-up.

Lastly, a computer, amplifier (2002 XTi Series, Crown by Harman), DAQ chassis (NI cDAQ-9174), VTS blower, Keyence 24 V DC power supply and controller were placed on a table adjacent to the vibration isolation table. The blower was connected using a hose to the shaker and was responsible for keeping the shaker cool. The computer was connected to the Keyence controller. The computer was also connected to the amplifier via the analog output NI-9263 DAQ card, and the amplifier was connected to the shaker. The amplifier was set to the fourth notch. Lastly, the Keyence controller was connected to the analog input NI-9205 DAQ card, which enabled data to be collected continuously over the course of the experiment. Images of the actual testing apparatus are provided in Figure 2.4.



Figure 2.4. Photo of the shaker system testing apparatus and control table.

Software

In order to control the shaker and record the data collected by the laser, the Keyence software that came with the laser vibrometer was used in combination with 2 LabVIEW programs that were developed for this study. One LabVIEW program controlled the waveform of the shaker (WaveGeneration.vi). The 2nd program collected the step data from the Keyence laser and wrote it to a .lvm file (LASER-Voltage-ContinuousInput.vi). The Keyence software calibrated the laser output such that 1 V correlated to 1 mm of deflection, and was periodically used to collect profile data.

The waveform generation virtual instrument controlled the amplitude, waveform, and frequency of the shaker's motion. Although the amplitude could be set directly on the amplifier, the choice was made to control the amplification of the signal solely from this VI. The graphical user interface and the block diagram are provided in Figure 2.5 and Figure 2.6, respectively.

The other LabVIEW program was created to continuously record step data from the Keyence software. This was important because the Keyence software could only collect a set amount of data before its memory filled, which left periods of the fatiguing process unrecorded. The graphical user interface and the block diagram for this VI are presented in Figure 2.7 and Figure 2.8, respectively.

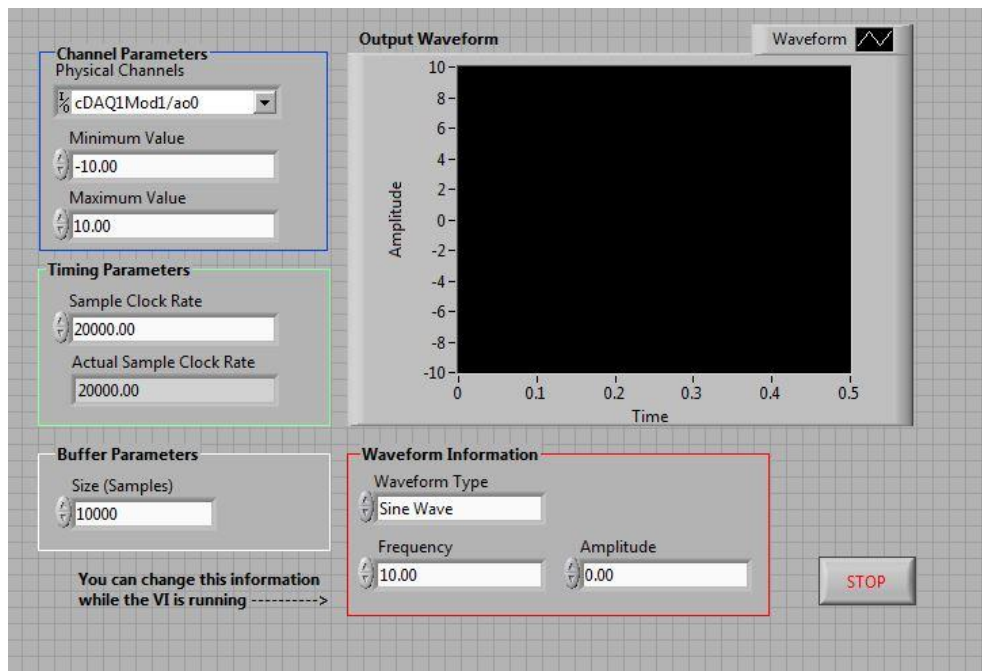
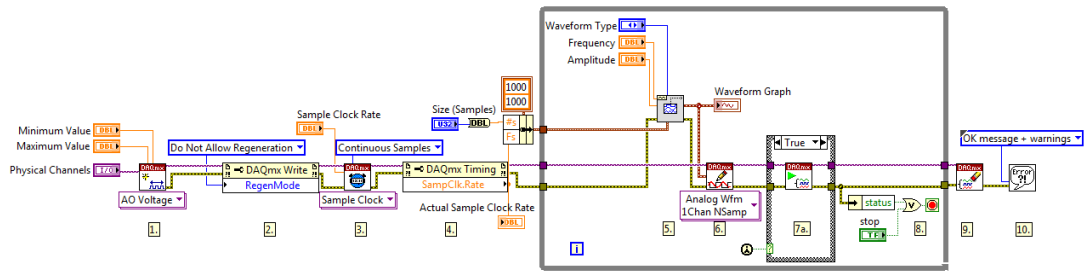


Figure 2.5. Waveform generation virtual instrument graphical user interface.



- Steps:
1. Create an Analog Output Voltage channel.
 2. Configure the task to prohibit the automatic regeneration of data.
 3. Call the DAQmx (Sample Clock) VI to set the sample clock rate. Additionally, set the sample mode to Continuous.
 4. Read the actual sample clock rate (eventually coerced depending on the hardware used).
 5. Compute the desired waveform, using the buffer size and the actual update rate. This VI keeps track of the phase of the waveform to ensure that the generated signal is continuous.
 6. Write the waveform to the output buffer.
 - 7a. Call the Start VI. This is only needed when the loop is executed for the first time.
 - 7b. Do nothing.
 8. Loop continuously until user presses the Stop button. Every iteration computes and writes a new waveform to the buffer.
 9. Call the Clear Task VI to clear the Task.
 10. Use the popup dialog box to display an error or warning if any.

Figure 2.6. Waveform generation virtual instrument block diagram.

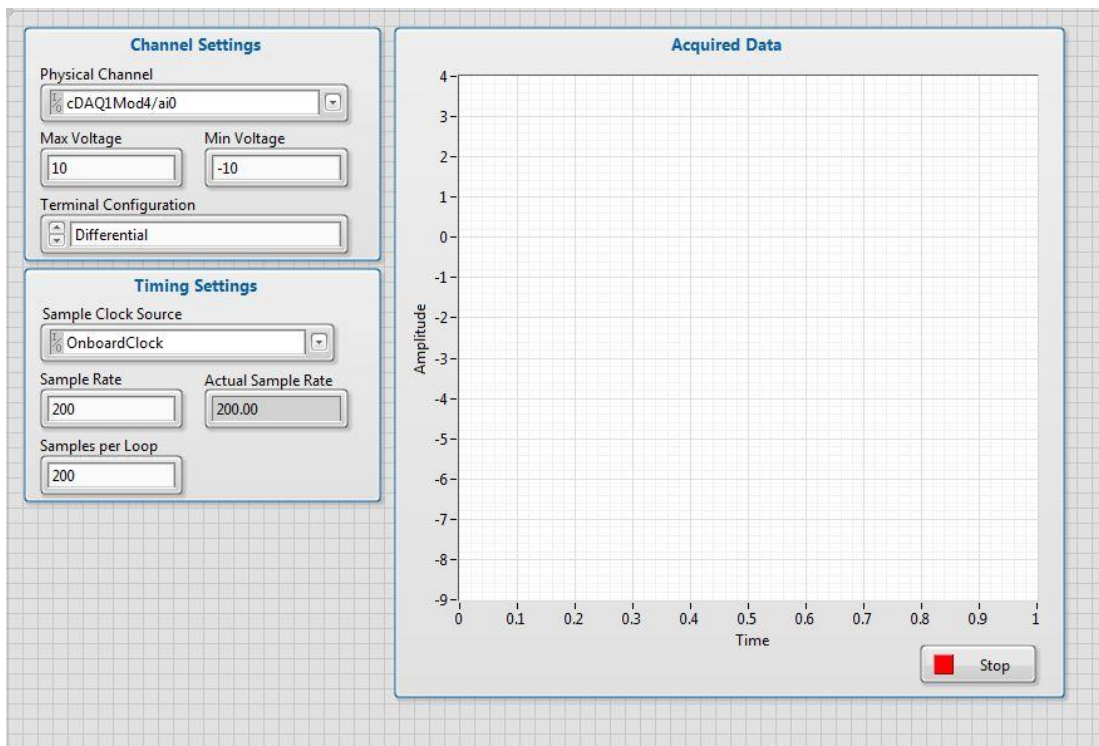


Figure 2.7. Continuous laser step data collection virtual instrument graphical user interface.

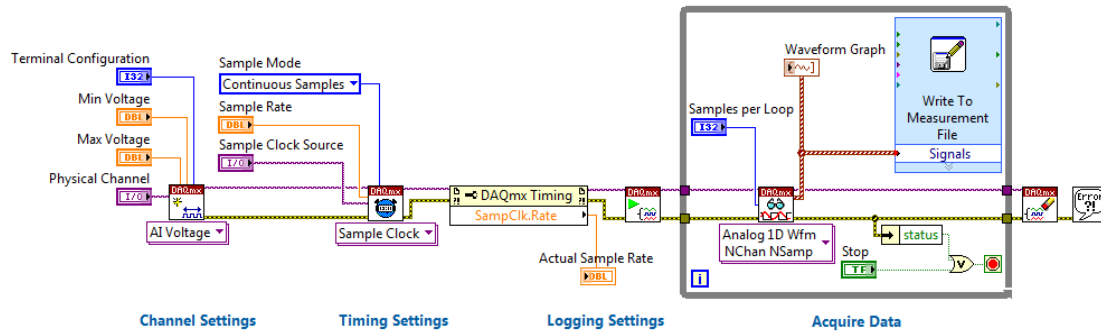


Figure 2.8. Continuous laser step data collection virtual instrument block diagram.

Experimental Method

Specimen and System Preparation

The specimen was set out to dry for 7 hours. At least 30 minutes prior to testing, the laser was turned on to warm up. The notch width and thickness of the specimen were measured with a digital micrometer and recorded. The steel pendulum plates were attached to the specimen, and the pendulum was mounted on the C-frame.

System Tuning

Once the specimen was mounted on the C-frame, the magnets were adjusted such that they had the same inward tilt and the pendulum, when hanging vertically, was centered between them. The pendulum was adjusted slightly up or down to achieve the desired frequency over each of the magnets, which was between 9 – 10 Hz. To determine the frequency, the pendulum was placed over one of the potential wells and gently tapped while the laser vibrometer collected data at 200 samples per second. That data file was then analyzed using a MATLAB program (ResonantFrequencyLVM.m) to determine the frequency over that potential well. If needed, the pendulum was adjusted up to decrease

the frequency or down to increase the frequency. Once the desired frequency was measured, the pendulum was placed over the second potential well, and the frequency over that well was measured. The goal was to tune the 2 potential wells to frequencies within 0.2 Hz of each other. If the difference in potential well frequencies were greater than 0.2 Hz, the magnet of the second potential well would be adjusted slightly in to increase the frequency or out to decrease the frequency.

Test Procedure

The frequency on the waveform generator (WaveGeneration.vi) was set to the frequency over the potential wells. If the frequencies were not equal, the average of the 2 frequencies was used. The goal was to set the forcing frequency equal to the resonant frequency over each well because the work done on the system by the applied force would cause the mechanical energy and amplitude of the system's response to increase. The energy and amplitude of the pendulum's swing would increase until it was large enough to escape the current potential well and fall into the other well.

Prior to starting the test, the amplitude on the waveform generator was set to zero. The blower was turned on. The data collection was started on the Keyence program and LabVIEW VI (LASER-Voltage-ContinuousInput.vi), and the waveform generator was started. The amplitude of the waveform was increased in increments of 0.25 until a reaching pattern was observed (see Figure 2.9, left). Then, it was increased by 0.10 until chaotic motion was initiated (see Figure 2.9, right). Finally, the amplitude was set to be 0.05 above that point for the remainder of the test. Periodically during the test, the Keyence profile data was saved, and the profile data collection was restarted.

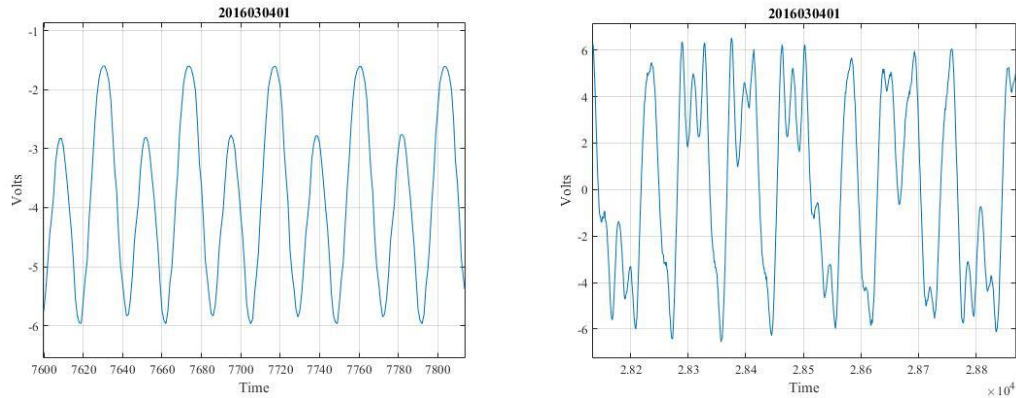


Figure 2.9. Reaching and chaotic motion: The left frame displays a reaching pattern while the right frame displays chaotic motion.

Analysis

Several MATLAB programs were developed and used to post process the data collected. These programs will be discussed in order of application, and the code is provided in Appendix D.

Resonant Frequency

The resonant frequency over each of the potential wells was determined during the tuning process. It was determined using the ResonantFrequencyLVM.m code. This code employed the pwelch (built in MATLAB) function to display a graph of the frequencies. From the graph, the resonant frequency could be identified as the largest peak.

Trim Data File

Each experiment took multiple hours to run. Since the tests ran for varying amounts of time, the system was set up to allow for the test to continue running without supervision overnight. Since it was desired to have a data file that only contained data for when the bone was fatiguing, the .lvm files collected via the LabVIEW program required trimming.

This was completed using the LaserLabViewCUT.m code. For this code, the user plotted the entire data file of amplitude versus time and manually selected the cut-off times for the desired subset of data. These times were entered by the user and the desired subset of the data was saved into a new text file.

Rainflow Counting

Next, the trimmed data was run through 2 different rainflow counting codes to determine the number of cycles at various amplitudes that were present in the data set. These codes varied only in the way they binned the data. First, the data was analyzed using rainflow_bins_mod3.m, which separated the cycle counts into 0.25 mm bins and displayed them in a histogram so the distribution could be clearly seen. Once this was done for all 10 experiments, 3 categories were defined to be the small, medium, and high amplitude bins. These 3 bins were then checked to ensure that they would correlate well with the prior study's small, medium, and large amplitude cycles. Once they were established, they were used in the second rainflow counting code, rainflow_bins_mod4.m, to determine the number of cycles at the small, medium, and high amplitudes.

Palmgren-Miner Rule

The Palmgren-Miner rule could be employed via PalmgrenMiner2.m. The total cycles to failure for the 3 different amplitudes used in this code were based on the values determined in the prior study [65] by Campbell. The uncertainty in the calculated damage accumulation parameter was determined using the standard deviation for each of the cyclic amplitude loading cycles to failure, from Campbell's study [65], and tracking the uncertainty through the damage parameter calculation. Once the damage parameter and its

uncertainty were known, the success of the PMR was evaluated for that test. If the bounds of the damage accumulation parameter encompassed 1, then the rule was said to be successful at predicting the fatigue life of the specimen because, according to the PMR, the material is said to fail when the damage accumulation parameter equals 1. Similarly, the rule was said to be unsuccessful at predicting the fatigue life of the specimen if 1 were outside the bounds of the damage accumulation parameter.

Phase Space Warping

The codes that were used in this analysis are the MATLAB programs that were developed by Dr. Chelidze from the University of Rhode Island. The series of programs were run using the main code called protocol2.m. Prior to running protocol2.m, the parameters for the PSW were set to the following: 8000 points for the reference model size, 32 boxes in the phase space, 20 points for the local linear model, a model prediction time of 1, 0 for the scalar tracking metric, and 2000 points in each record. Also, it was set such that the program preprocessed the data; the final parameter was 1. The delay time was determined using average mutual information with the following parameters: 8000 points were used in the calculation, the maximum delay parameter was set to 60, and the number of bins used in the calculation was 32. Next, the embedding dimension was determined via false nearest neighbors, which utilized the delay time, a maximum embedding dimension of 6, and it was set to use 8000 data points. These parameter values were chosen based off of Dr. Chelidze's guidance and via trial and error in order to get the clearest output for each of the experiments.

After running the PSW program, 2 types of output graphs were visually inspected and analyzed. The first plot type displayed the smooth orthogonal values (SOV), and the

individual or groupings of SOVs set apart from the continuum identified active fatigue damage modes. The second type of graph plotted the smooth orthogonal coordinates (SOC) that corresponded to the SOVs of interest. The graphs of the SOCs for each experiment were compared to each other in order to identify patterns and trends in the fatiguing process.

CHAPTER THREE

Results

The fatigue test was performed on 10 bovine bone specimens, and it was run until the specimen broke into 2 pieces. Graphs of the time series for each test are presented in Figure 3.1. The vertical axis represents the trajectory of the pendulum where 1 Volt corresponds to 1 millimeter, 0 Volts is the position between the 2 potential wells, positive voltage corresponds to the potential well furthest from the shaker, and negative voltage corresponds to the potential well closest to the shaker. After failure, the fracture surface was studied, the cycles to failure were evaluated, and the slow time dynamics of the system were analyzed.

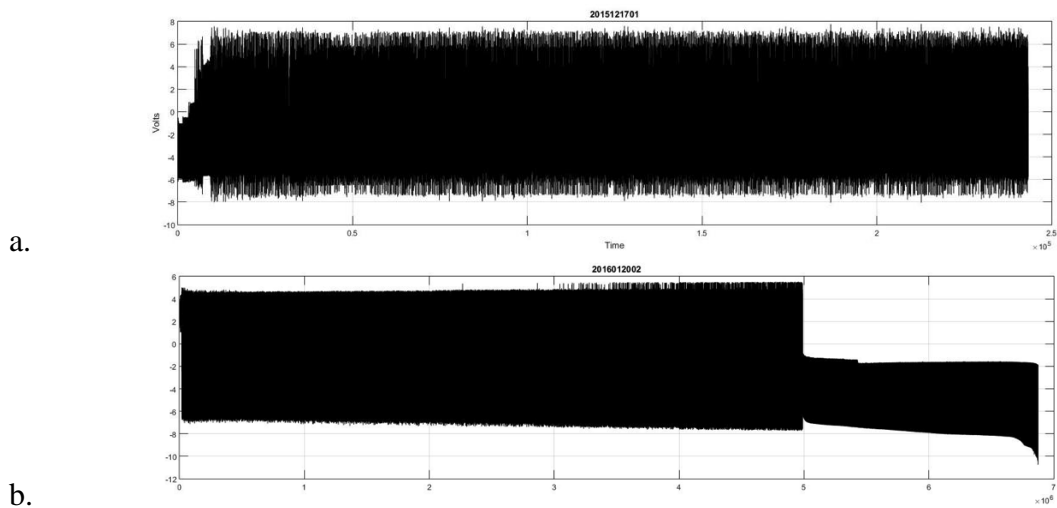
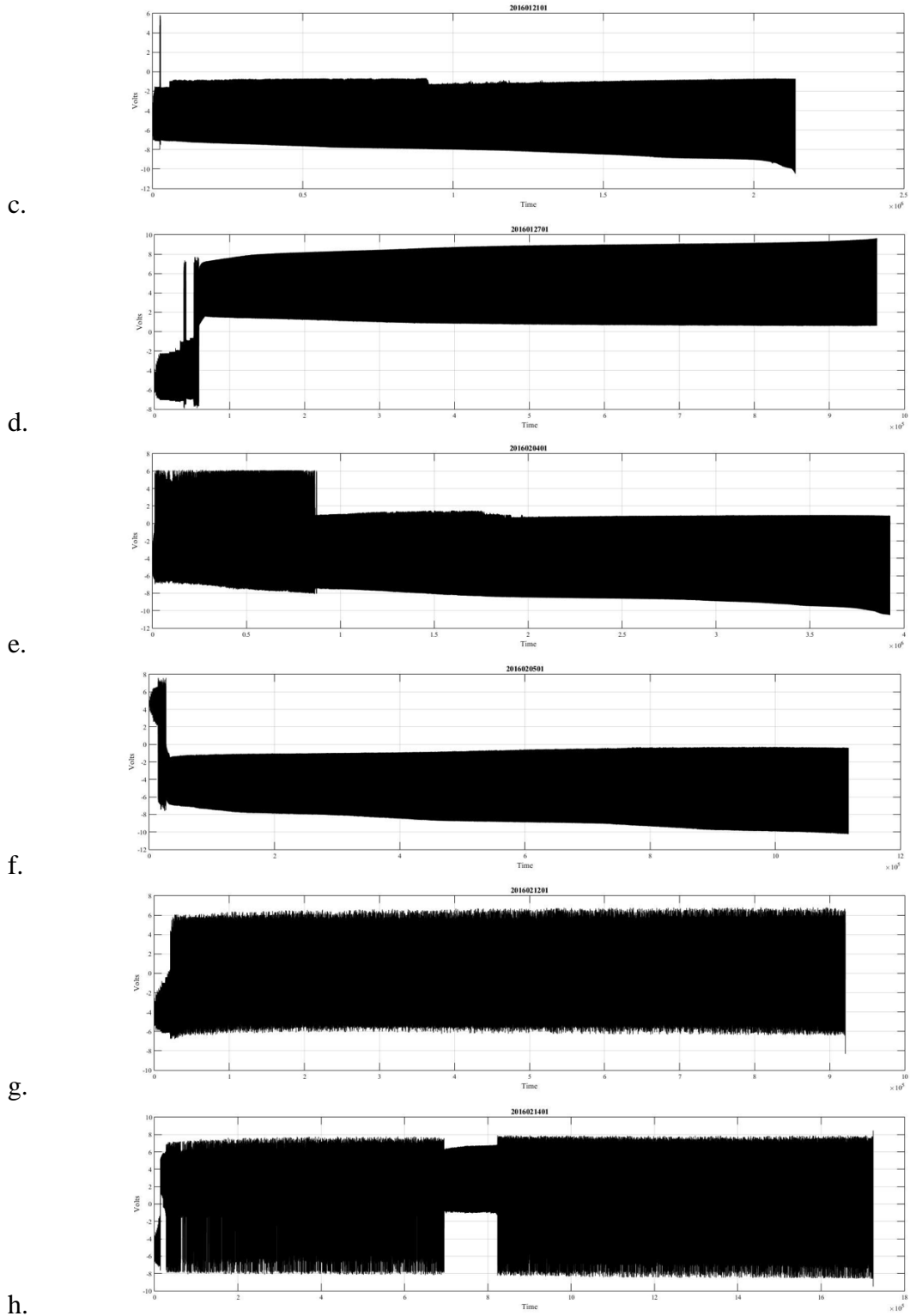


Figure 3.1. Time series: Graphs a-j correspond to specimens 1-10, respectively.



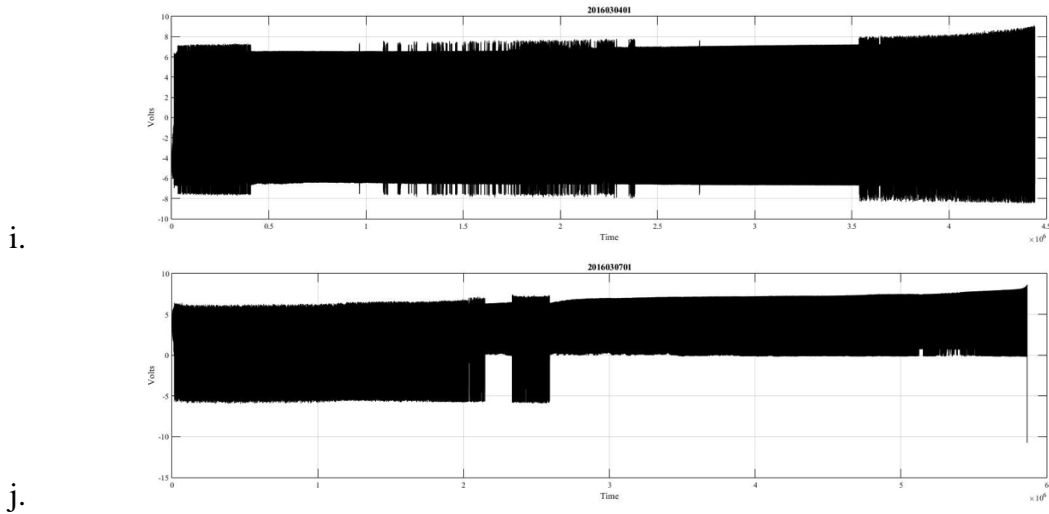


Figure 3.1 continued. Time series: Graphs a-j correspond to specimens 1-10, respectively.

Classification of Fracture Surface

First, after each specimen failed, it was visually inspected. A photograph of the fracture was taken with a 16-megapixel camera (Samsung, Gyeonggi-do, Korea). Images are provided in Appendix B. The breaks were initially classified based off of knowledge of fracture types from the prior study and the observations made from these visual inspections and images of the specimens' fracture surfaces (see Figure 3.2). It appeared as though 6 of the 10 specimens experienced a combination of ductile and brittle break, which is the type of break that was expected based off of the prior study. Of the remaining 4 specimens tested, 1 appeared to display a predominately brittle fracture and 3 a predominately ductile fracture. A brittle break was evidenced by a fast break across the specimen's test section. A ductile break was evidenced by a slow break where the crack propagation is apparent. A combination break showed evidence of a slow break leading to a fast break.

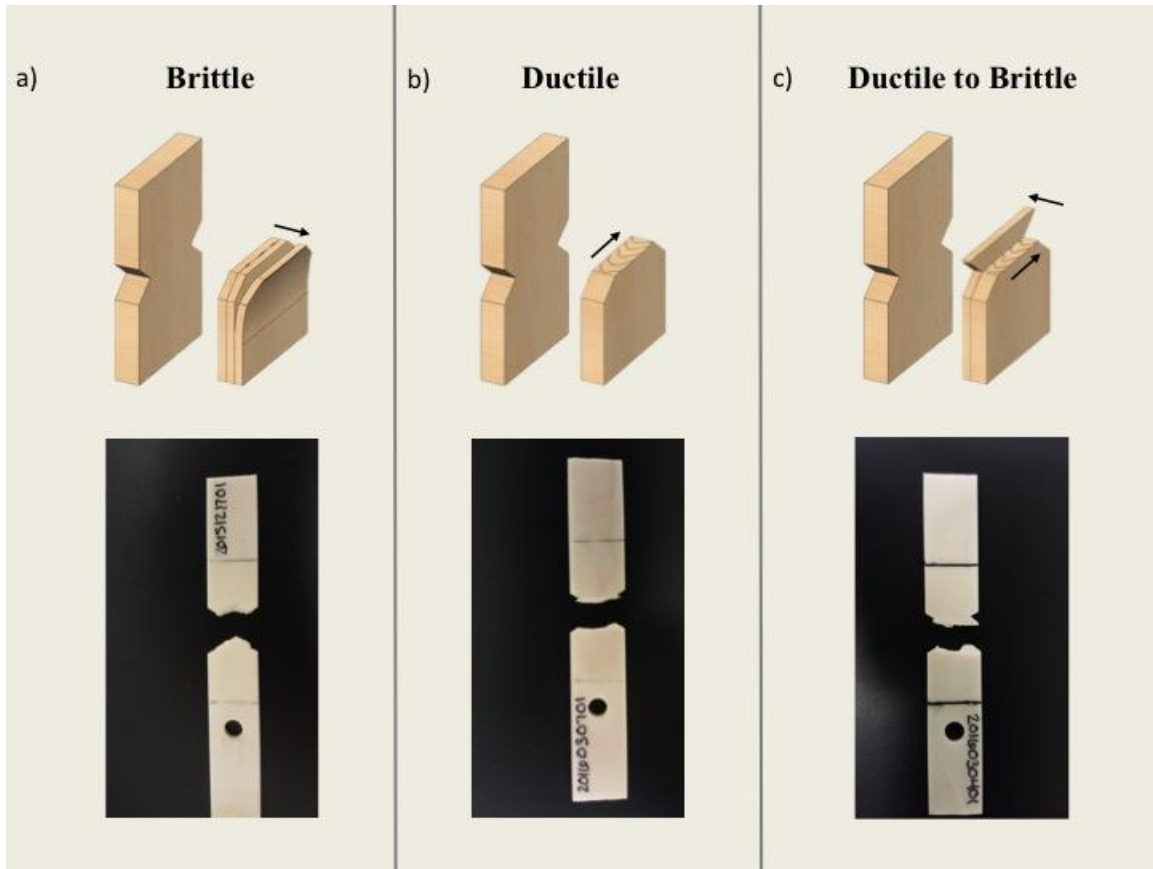


Figure 3.2. Fracture classification [65].

Additionally, the fracture surface was imaged with a scanning electron microscope, SEM (JEOL, Peabody, MA). The SEM was set to BEC (Bose-Einstein Condensate), spot size 65, and 5 kV. The fracture classification determined previously was confirmed with the SEM images. The brittle breaks displayed delamination between the layers of the bone tissue. The ductile breaks displayed beach markings and osteon pullout. The mixed mode breaks showed a combination of the three. See Figures 3.3 through 3.7 for images of brittle, ductile, and combined breaks. Table 3.1 reports the break classification.

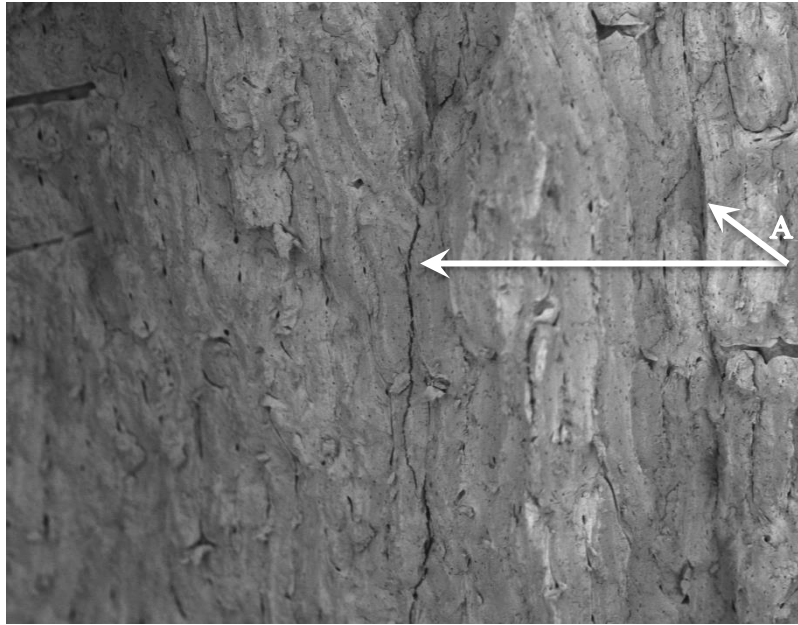


Figure 3.3. Brittle break: A brittle break is revealed via an SEM image taken with the BEC setting at 55x magnification of the fracture surface of specimen 1 (2015121701). The solid arrow points out evidence of delamination.

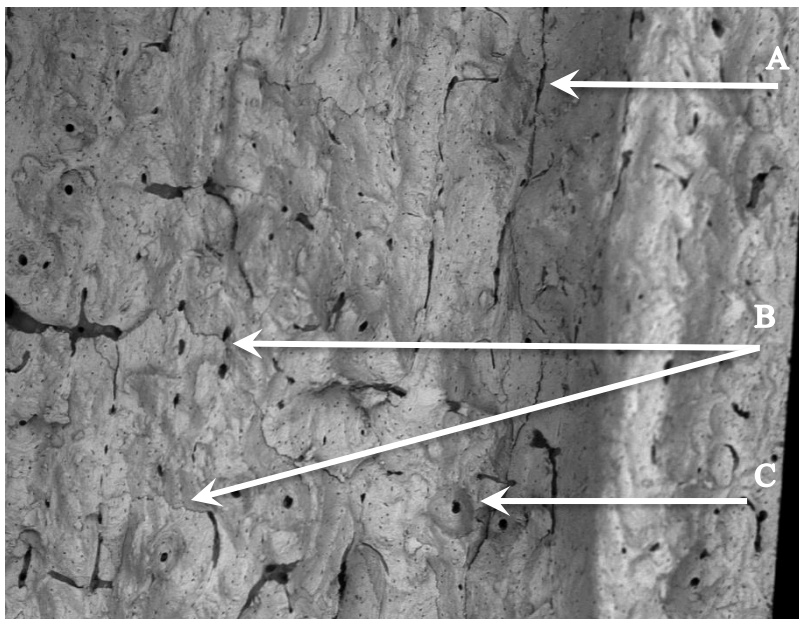


Figure 3.4. Mixed mode break: A 3 mode break is revealed via an SEM image taken with the BEC setting at 55x magnification of the fracture surface of specimen 8 (2016021401). There is evidence of (A) delamination, (B) beach markings, and (C) osteon pullout.

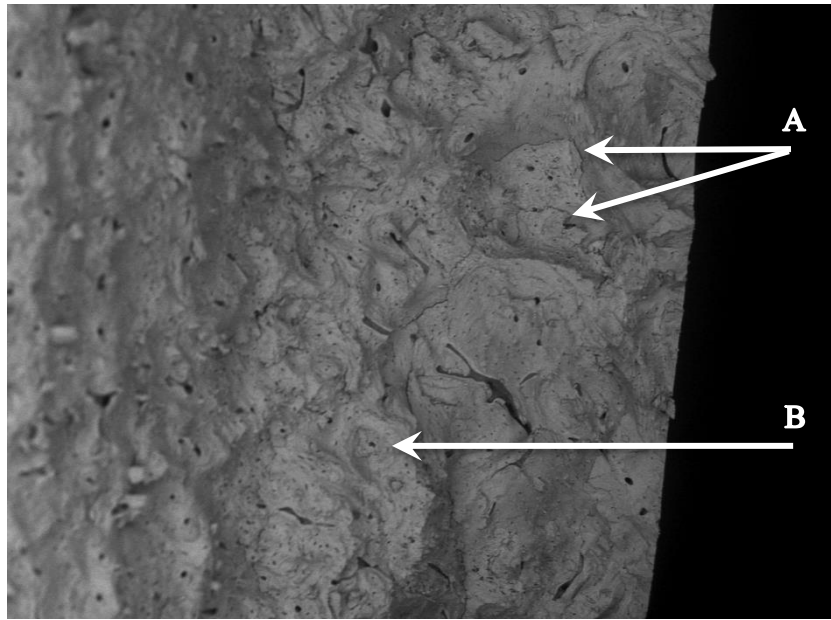


Figure 3.5. Ductile mixed mode break: A 2 mode ductile break is revealed via an SEM image taken with the BEC setting at 55x magnification of the fracture surface of specimen 4 (2016012701). There is evidence of (A) beach markings and (B) osteon pullout.

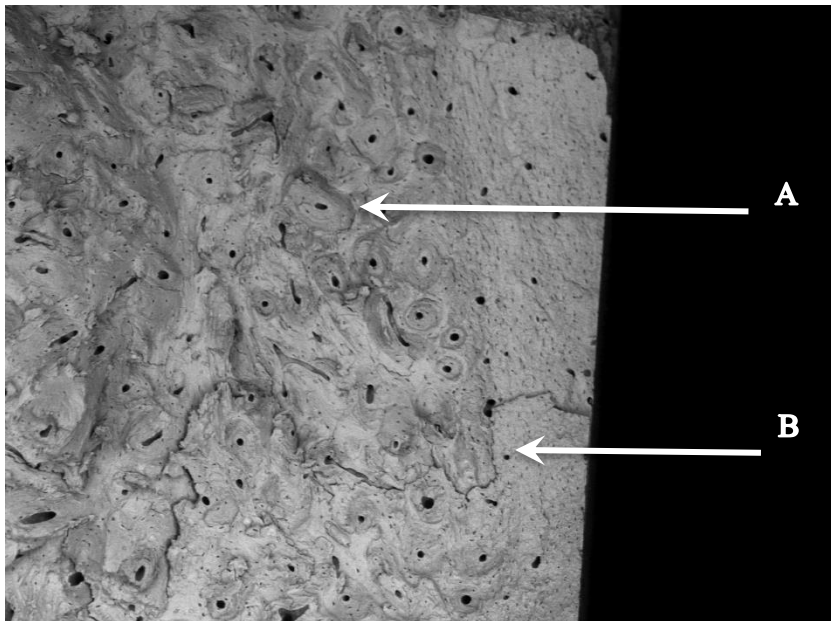


Figure 3.6. Ductile mixed mode break with osteon pullout predominant: A 2 mode ductile break is revealed via an SEM image taken with the BEC setting at 55x magnification of the fracture surface of specimen 10 (2016030701). There is evidence of (A) osteon pullout and (B) beach markings.

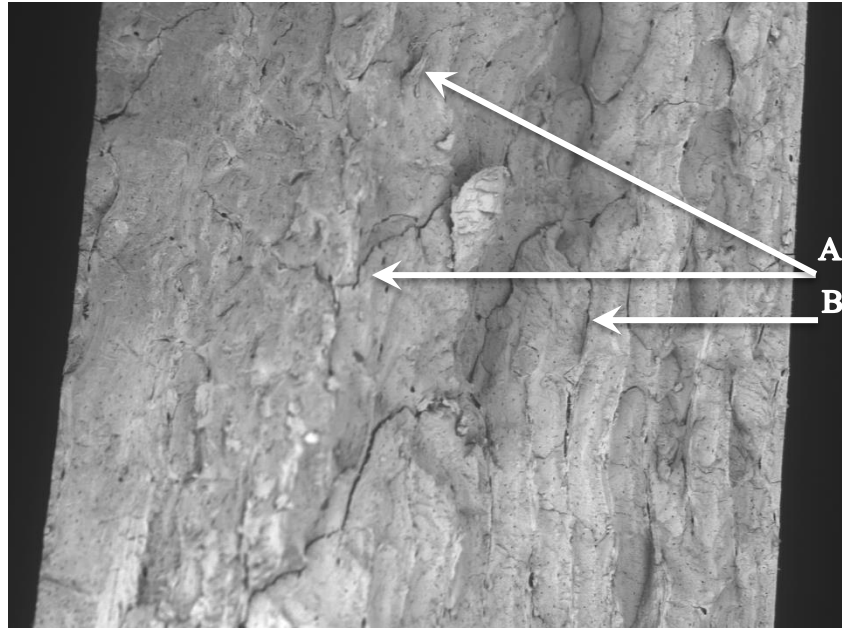


Figure 3.7. Mixed mode break: A 2 mode break is revealed via an SEM image taken with the BEC setting at 55x magnification of the fracture surface of specimen 9 (2016030401). There is evidence of (A) beach markings and (B) delamination.

Table 3.1. Break Classification.

Specimen	Specimen Label	Break Classification
1	2015121701	Brittle
2	2016012001	Ductile/Brittle
3	2016012101	Ductile/Brittle
4	2016012701	Ductile
5	2016020401	Ductile/Brittle
6	2016020501	Ductile
7	2016021201	Ductile/Brittle
8	2016021401	Ductile/Brittle
9	2016030401	Ductile/Brittle
10	2016030701	Ductile

Rainflow Counting

The method of rainflow counting was applied to the data and the cycles were binned 2 different ways as can be seen in Figure 3.8. The first binning method consisted of 0.25

mm bins in order to display the distribution of the cycle types, which can be seen in the left column of Figure 3.8. The small, medium, and large deflection amplitudes, ranges 1, 2, and 3, respectively, were determined from these histograms; the data was binned accordingly as can be seen in the right column of Figure 3.8. Based off of the prior study, range 1 corresponds to a ductile break, range 2 corresponds to a mixed ductile and brittle break, and range 3 corresponds to a brittle break [65]. Table 3.2 tells the number of cycles for the small, medium, and large deflection amplitudes, and the total number of cycles to failure for each test.

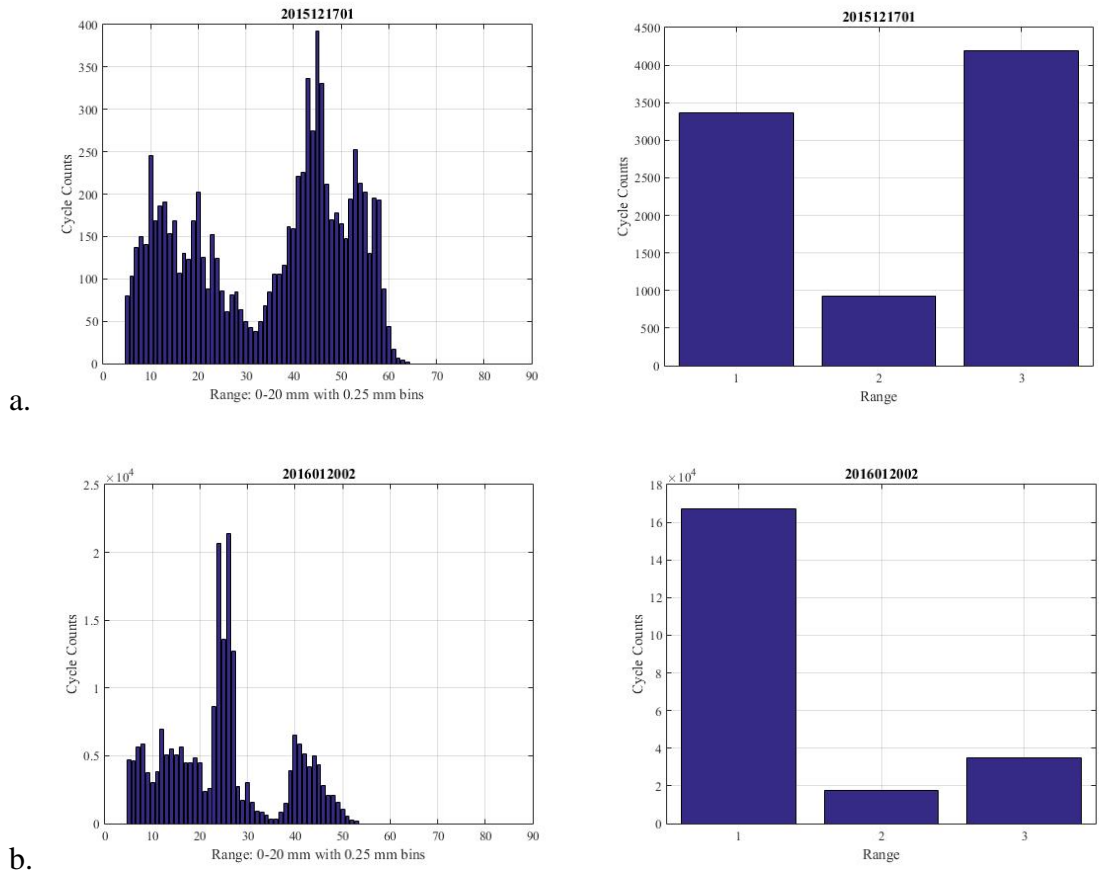
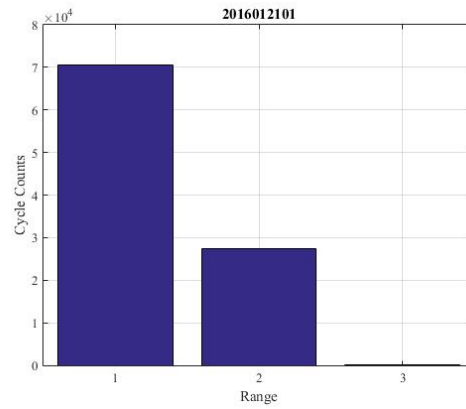
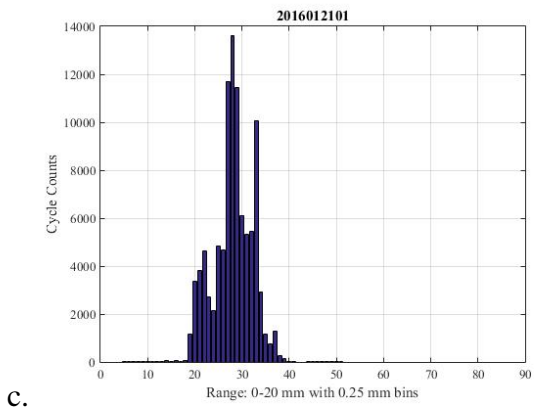
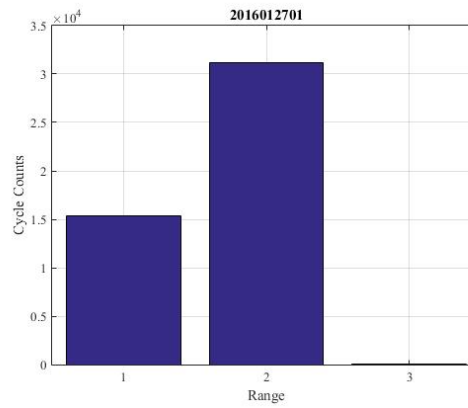
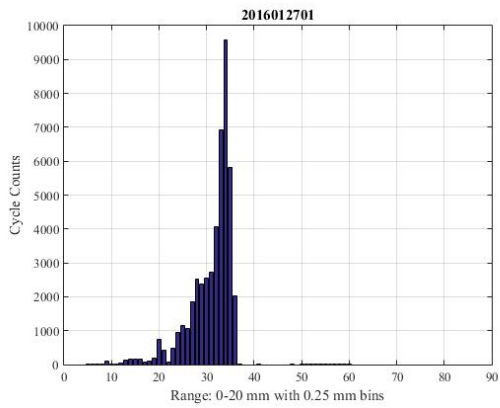


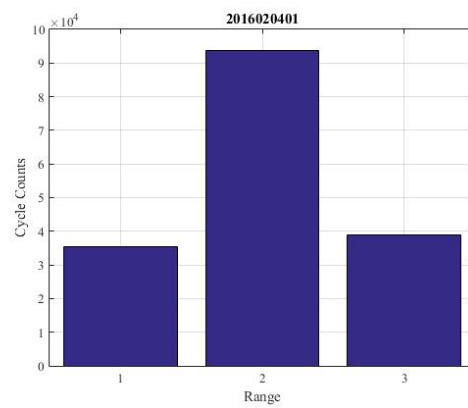
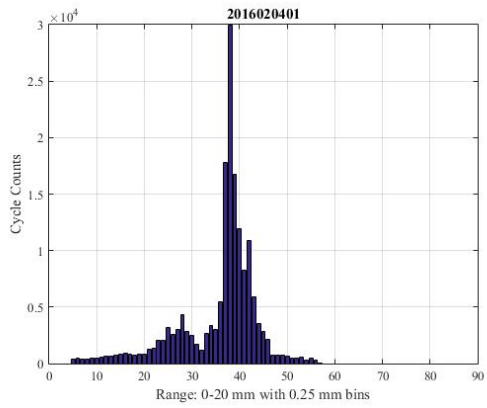
Figure 3.8. Histograms: Rows a-j correspond to specimens 1-10, respectively.



c.



d.



e.

Figure 3.8 continued. Histograms: Rows a-j correspond to specimens 1-10, respectively.

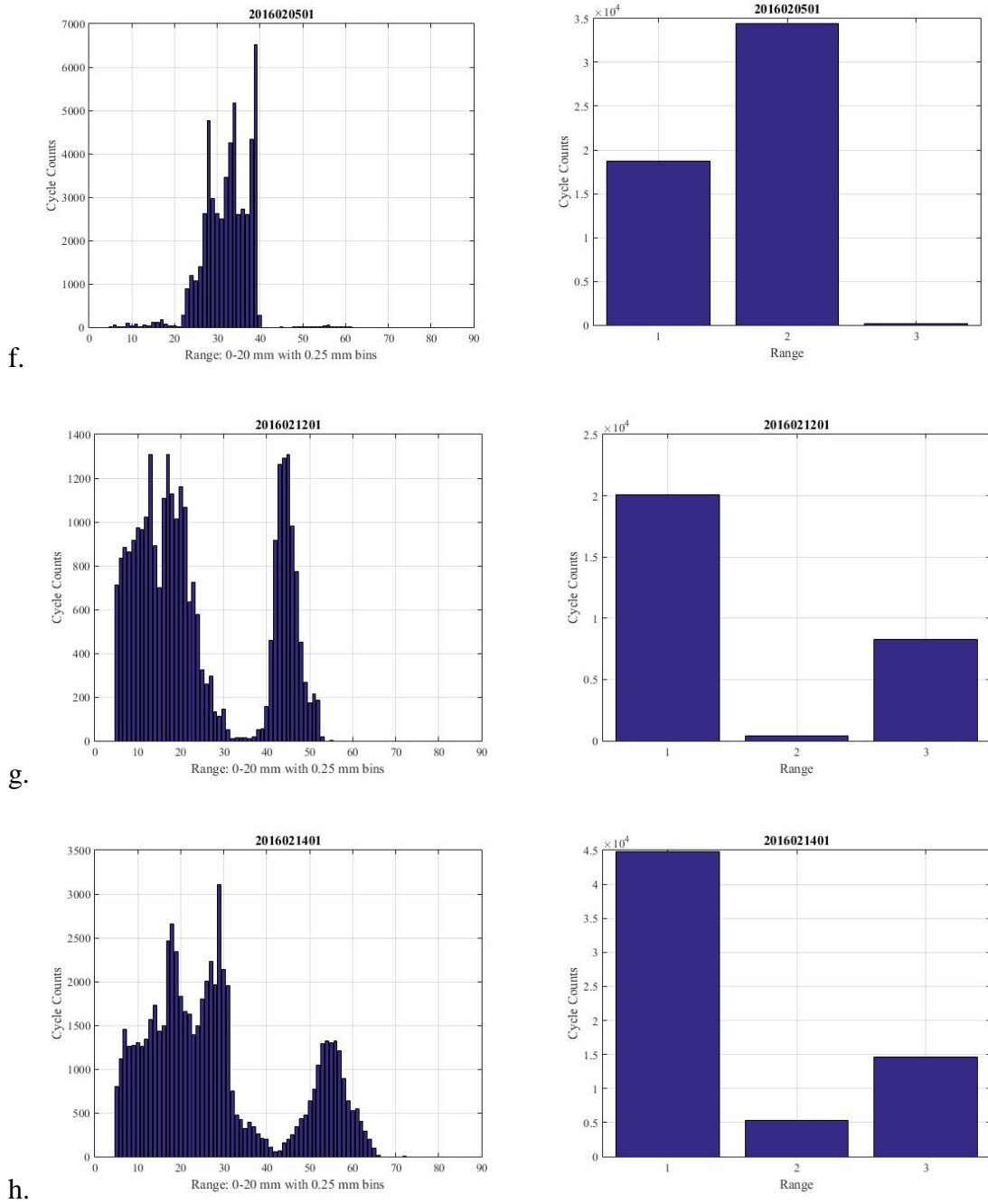


Figure 3.8 continued. Histograms: Rows a-j correspond to specimens 1-10, respectively.

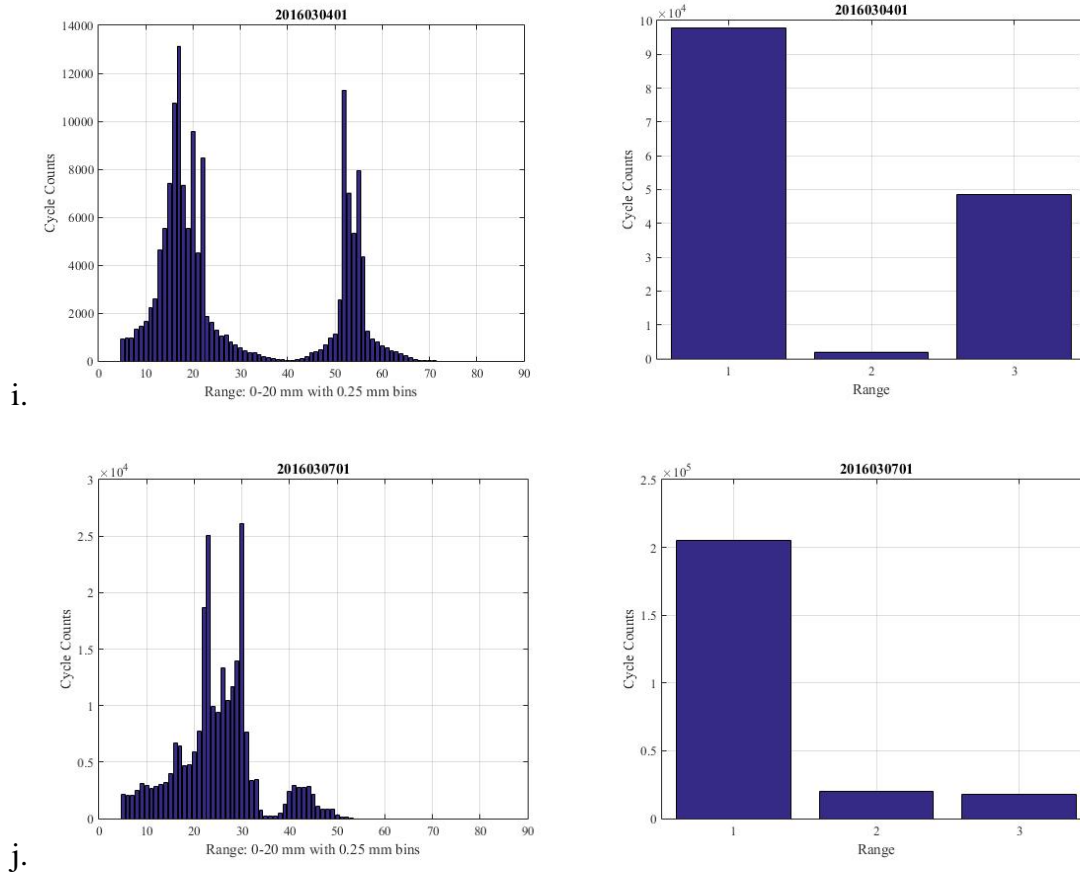


Figure 3.8 continued. Histograms: Rows a-j correspond to specimens 1-10, respectively.

Table 3.2. Rainflow Counting Cycles and Break Classification: D, DB, and B stand for ductile, mixed ductile and brittle, and brittle break types, respectively.

Specimen	Break Classification	Small Amplitude Cycles	Medium Amplitude Cycles	Large Amplitude Cycles	Total Cycles to Failure
1	B	3,368.5	928.5	4,194.0	8,491.0
2	DB	167,246.0	17,362.0	35,158.5	219,766.5
3	DB	70,507.5	27,380.0	19.5	97,907.0
4	D	15,319.5	31,140.5	97.5	46,557.5
5	DB	35,345.5	93,852.0	38,852.0	168,049.5
6	D	18,686.5	34,443.5	136.0	53,266.0
7	DB	20,066.0	393.5	8,295.0	28,754.5
8	DB	44,771.0	5,322.0	14,593.5	64,686.5
9	DB	97,899.0	1,945.5	48,546.0	148,390.5
10	D	205,378.0	20,077.0	17,521.5	242,976.5

Palmgren-Miner Rule

The damage accumulation parameter and its uncertainty are reported in Table 3.3 for each test. The predicted cycles to failure are reported for each specimen based off of the calculated damage accumulation parameter.

Table 3.3. Palmgren Miner Rule Results and Break Classification: D, DB, and B stand for ductile, mixed ductile and brittle, and brittle break types, respectively.

Specimen	Break Classification	Predominant Amplitude	Total Cycles to Failure	Predicted Cycles to Failure	Damage Accumulation	Prediction Success
1	B	Large	8,491.0	18,104.5	0.469 ± 0.191	No
2	DB	Mixed	219,766.5	42,458.8	5.176 ± 1.611	No
3	DB	Small	97,907.0	81,318.1	1.204 ± 0.254	Yes
4	D	Medium	46,557.5	51,331.3	0.907 ± 0.288	Yes
5	DB	Mixed	168,049.5	25,770.5	6.521 ± 1.971	No
6	D	Medium	53,266.0	52,324.2	1.018 ± 0.318	Yes
7	DB	Mixed	28,754.5	29,133.2	0.987 ± 0.378	Yes
8	DB	Mixed	64,686.5	33,655.8	1.922 ± 0.667	No
9	DB	Mixed	148,390.5	26,366.5	5.628 ± 2.211	No
10	D	Small	242,976.5	64,759.2	3.752 ± 0.824	No

Phase Space Warping

The phase space warping method was used to analyze 6 of the 10 data sets. The other 4 tests were discarded due to high frequency contamination. The results for the 6 uncontaminated tests can be seen in Figure 3.9. This figure shows graphs for the smooth orthogonal values (eigenvalues) in the left column, corresponding smooth orthogonal coordinates (projection of the data onto the smooth orthogonal modes) in the center and right columns. For clarity, the curves in the center column have been color-coded; black and red signify brittle and ductile mechanisms, respectively. The curves in the right column depict the first few SOM of the high frequency continuum. The time scales of the fatigue damage modes revealed by the SOVs are compared to the modes revealed by the SEM images in Table 3.4.

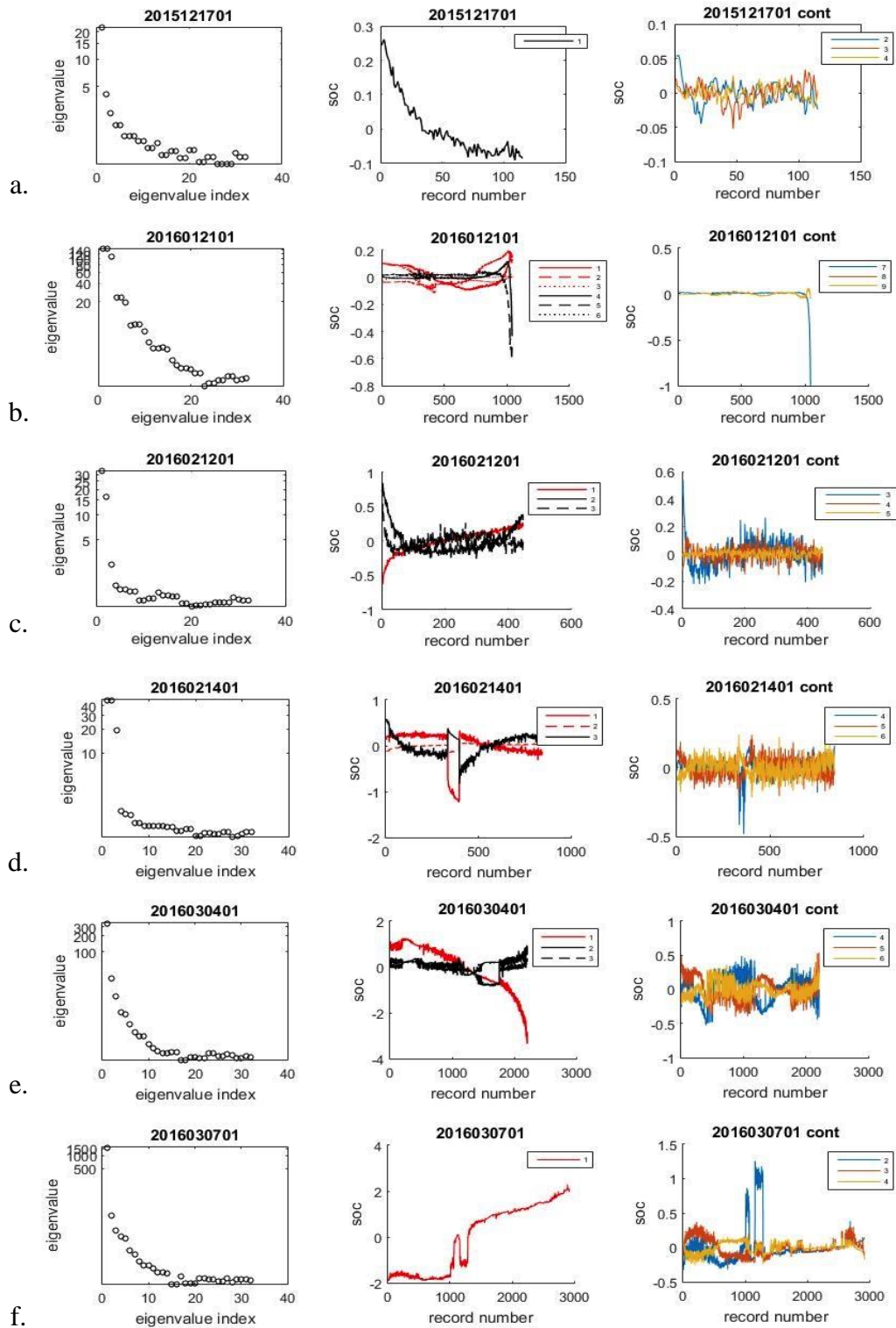


Figure 3.9. Phase space warping eigenvalue (smooth orthogonal variables, SOV) and smooth orthogonal coordinates (SOC) graphs. Rows a-f correspond to specimens 1, 3, 7, 8, 9, and 10, respectively.

Table 3.4. Phase space warping SOV chart.

Specimen	Break	
	Classification	Eigenvalues (SOV)
1	B	22.4
2	DB	--
3	DB	146.1; 108.8; 23.54; 19.54
4	D	--
5	DB	--
6	D	--
7	DB	33.4; 16.37; 2.547
8	DB	47.28; 19.52
9	DB	351.1; 31.53; 14.32
10	D	1,589

CHAPTER FOUR

Discussion and Conclusion

Discussion

The purpose of this research was to study the influence of chaotic forcing on bone fracture mechanics and evaluate the effectiveness of the Palmgren-Miner rule (PMR) and phase space warping (PSW) at monitoring the health of bone and predicting when it would fail due to fatigue. An earlier study conducted by Campbell evaluated the fracture mechanisms and the accuracy of the PMR predictions for bovine bone specimens that underwent cyclic and variable amplitude loading [65]. In the earlier study, the specimens subjected to cyclic high amplitude fatigue tests experienced a brittle fracture, those subjected to cyclic low amplitude fatigue tests experienced a ductile fracture, and those subjected to cyclic medium amplitude fatigue tests experienced a mixed ductile and brittle fracture. The specimens subjected to variable amplitude fatigue tests, which consisted of a repeating pattern of low amplitude cycles followed by high amplitude cycles, experienced a mixed ductile and brittle fracture.

When the PMR was applied to the tests completed in this study, it did not accurately predict the fatigue life for 6 of the 10 tests. The specimens broke later than the rule predicted for 5 of the 6 tests, which is the opposite of what was observed in the previous study. This may be due to the differences in the experimental set-up. In the previous study [65] by Campbell, 2 rollers were used to guide the specimen's movement and forced it to bend a set amount each time (See Appendix G). In the current study, the specimen was

allowed to freely oscillate over 2 rare earth magnets. As the specimen was fatiguing it was experiencing structural parameter changes, which would feedback to the system and affect the motion of the pendulum. It is possible the motion adjusted such that the bone experienced less stress. Additionally, the magnets contributed a tensile load on the pendulum evidenced by osteon pullout, which was not observed in the prior study. According to the work of Hiller et al. on equine metacarpal bones, the amount of osteon pullout present is dependent upon the location within the bone and the manner in which the bone was fractured [50]. In their study the specimens were tested in 4-point bending. Osteon pullout was mainly present on the tensile side of dorsal specimens that were fatigued. When the specimens in this study were in the small swing phase, there was an approximately 2 degree offset angle, which would have also increased the magnitude of the tensile load experienced on one side of the bone specimen as compared to the amount of tension experienced in the small amplitude tests of the prior study.

Of the 4 tests that the PMR successfully predicted the fatigue life of the specimen, 3 were expected because they remained mainly in the small swing phase and the SEM images showed a predominately ductile fracture pattern for each. The number of cycles to failure for these specimens agreed with the number of cycles to failure for the cyclic loading tests of the prior study, which were used as the fatigue life in this study. The SEM images for the test that the PMR unexpectedly worked for reveal the majority of the fracture surface evidences a ductile break with beach markings and osteon pullout while only a small portion evidences a brittle break with delamination. This would imply that the main fracture mode was ductile; therefore, the PMR was partially successful for predicting the failure in this test. Therefore, the results indicate that when there is only one fracture

mechanism present, the PMR is more reliable than when more than one fracture mechanism is present.

The second method that was used to analyze the damage state of the bone specimens was PSW. This study has shown that PSW is capable of distinguishing different fatigue damage modes in bone. The graphs of the smooth orthogonal values (SOV), eigenvalues equivalent to the inverse of the frequency squared ($1/\omega^2$), reveal the different damage modes and their time scales. Relevant damage modes can be identified from the individual or groupings of SOVs that are distinctly isolated from the continuum. The continuum corresponds to the high frequency noise floor. See the left column of the Figure 3.9 and Table 3.4. The frequencies that are revealed by these groupings agree with the damage types identified with the SEM images for each test. The larger eigenvalues correspond to a lower frequency of damage accumulation, while the smaller eigenvalues correspond to a higher frequency of damage accumulation. The high frequency/fast time scale for the damage acquisition corresponds to a brittle break as would be expected, and the low frequency/slow time scale for the damage acquisition corresponds to a ductile break. The division between SOV amplitudes that correspond to brittle or ductile breaks in any given experiment is clear, but the inter-experimental comparison is not. This may be because of the limited number of tests conducted and successfully evaluated in this study or due to the specific damage evolution of each specimen. There were 2 specimens for which observed frequencies were very close in value but signified different damage modes. For specimen 7 the eigenvalue of 33.4 corresponded to a ductile fracture. However, for specimen 9 the eigenvalue of 31.53 corresponded to a brittle fracture. It should be emphasized that the PSW technique was able to isolate ductile and brittle fracture

mechanics in each experiment, but more research is required to determine if there are universal relationships between SOV amplitudes or if the amplitudes are case by case dependent.

Along with the distinct time scales, each point in the separate groups of the SOVs corresponds to distinct damage coordinates and modes. Graphs of the SOCs that correspond to the significant SOVs are presented in the center column of Figure 3.9, while graphs of the SOCs that correspond to the first 3 SOVs of the continuum are presented in the right column of Figure 3.9. The graphs of the SOCs from the continuum contain a significant amount of high frequency noise; therefore, they were not used in the rest of the analysis. Additionally, there was no apparent trend in the curve paths of the SOCs that corresponded to the significant SOVs. This may be a case-by-case damage evolution detail, due to contamination from the unfiltered high frequency noise, or trends may become apparent as more samples are tested. The data from only 6 of the 10 tests was analyzed with the phase space warping method. Many more tests are required to determine if there is any pattern to the SOCs. Then it may be possible to develop new damage/fatigue laws for bone, as was successfully done when this experiment was conducted on metal. Once this is achieved, the PSW method may be used to monitor bone health and predict failure in bone.

Conclusion

Based on the results of this study and the prior study [65] by Campbell, the PMR does not provide an accurate or reliable estimation of the fatigue life of bone when there is more than one active damage mechanism. Campbell observed that the bone fractured prior to the estimated life expectancy. In the current study, the bone specimen tended to fail after

the estimated life expectancy was reached. The cause of this discrepancy is unclear; it may be due to structural parameter changes feeding back into the forcing of the current study.

To the author's knowledge, prior to this study, the method of PSW had never before been applied to bone tissue. The research conducted here indicates that the PSW method shows promise in being used as a tool to monitor bone health and predict the fatigue life of bone. It was able to clearly distinguish the various damage modes present in each test it was applied to. In a future study with a larger database, these findings can be compared to various damage laws.

Both the current study and the prior study [65] that it is based on are pilot studies intended to develop an experimental apparatus and procedure, and to demonstrate the proof of concept before pursuing experiments on large numbers of specimens. In order to gain statistical significance more tests will need to be run for both. Furthermore, some modifications of the test set up are desired in order to gain more knowledge of the fracture mechanics and to improve the data quality. These modifications are discussed in the following section on future work.

CHAPTER FIVE

Future Work

Determine Strain

Due to the methods employed in this study, the strain that the bone was subject to was unknown. Knowing the strain would help in better understanding the fatigue process and is important for being able to accurately predict the fatigue life. Therefore, more experiments need to be run that will take this into account.

At the start of these pilot studies, a strain gage was used rather than the laser vibrometer. The strain gage that was being used was a T gage that was glued to the bone specimen at the notch location. After several tests were conducted with this configuration, it was determined that the strain gage was reinforcing the bone at that location and was influencing the strain measurements. As a result, the strain gage was replaced with the laser vibrometer. Since strain is the change of length divided by the length, it was thought that the strain could be determined via post processing from the bend in the specimen. It was later determined that those values were of limited value.

To determine the strain in the future, either another tool will have to be used, a new type of strain gage and configuration will need to be employed, or the method of post processing the laser vibrometer data will need to be reevaluated and refined. The best method is currently unknown, so these various options will need to be explored. Then the best method will need to be incorporated into the shaker system testing apparatus and experimental method.

Improve Apparatus

In the current study, some of the data was contaminated by high frequency noise. This noise was likely introduced into the system upon elongating the piece that connects the shaker to the C-frame from 1.5 inches to 8 inches, which was done in order to eliminate the magnetic interference of the electromagnetic shaker with the pendulum. When the connecting piece was made longer, it caused the natural frequency of the apparatus to decrease. When the natural frequency of the apparatus was lowered, it became low enough to interfere with the frequencies of interest in the test. The manner in which the current study dealt with this issue was to utilize a low pass filter created in MATLAB during post processing; however, it would be better to complete this as the data is collected. Therefore, in order to prevent the high frequency noise being folded back over the data, a programmable low pass filter should be added to the shaker system and filter the data signal as it is collected. The SR-640 programmable 2-channel low pass filter (Stanford Research Systems, Inc., Sunnyvale, CA) has now been incorporated for this purpose.

Another area in which the system could be improved is the magnet subsystem. The changes to this subsystem are needed to increase the ease of use of the apparatus and repeatability of the experiment. Currently, the magnets are separate from each other and must be adjusted individually which takes a significant amount of time. Additionally, the distance between the magnets and the angle of the magnets may be slightly different each time the test is run. Furthermore, it is difficult to set the 0 location for the pendulum displacement once the system is tuned. The way the system is set up, the operator holds the pendulum while he or she zeros the system, which can lead to error in the 0 displacement position. Therefore, in the redesign of this subsystem, the magnets need to be set such that

there is only 1 degree of freedom in their adjustment and they may be moved together. Additionally, it would be desirable for the magnets to be able to be moved far enough apart so the pendulum can hang at the zero position for the initial zeroing of the test, and then return the magnets to the properly tuned position.

Statistical Significance

Since this study was completed as a pilot study, not enough tests were run for the results to obtain statistical significance. However, now it is known that the PSW method holds promise in being able to predict failure of bone tissue and is worth further research. Once the strain is determined and the low pass filter is installed, many more tests shall be run in order to gain statistical significance.

APPENDIX

APPENDIX A

Data Logbook

Chaotic Forcing - run until failure												
Usable Data												
Specimen Name	Thickness (in)		Notch Width (in)		Gauge Length (in)		Left Well	Right Well	Forced	Amp	Notes	
	mean	std dev	mean	std dev	mean	std dev	Frequency (Hz)	Frequency (Hz)	Frequency (Hz)			
1	2015121701	0.1039	0.000376386	0.3256	0.000376386	0.9539	0.000376386	8.984	9.082	9.03	3	Ramp: 0.5, Greatly in large swing
2	2016012002	0.0909	0.001635543	0.3246	0.001083974	0.8807	0.002387467	9.277	9.375	9.33	1.75	Ramp: 0.25, let sit at amp 1.5 for a min then increased to 1.75 to induce chaotic motion, ran overnight, Greatly in large swing phase
3	2016012101	0.0986	0.001474788	0.3507	0.001151086	0.8918	0.010431922	9.082	9.277	9.18	1.6	Ramp: 0.25, let sit at amp 1.5 for a min then (per Dr. Kuehl's prompting) touched the pendulum and induced chaotic motion for a few seconds, increased amp to 1.6 no chaotic motion but periodically would reach more towards the other well
4	2016012701	0.0906	0.001387444	0.3534	0.000821584	0.8881	0.007971825	9.668	9.766	9.72	1.9	Ramp: 0.25 until 1.5, then 0.1 to 1.8, then 0.05 to 1.9... 1 min at amp 1.5, 30 sec at each subsequent increase. Tapped specimen at 1.8 to incite chaotic motion - didn't really work so increased amp. At amp 1.9 there was chaotic motion
5	2016020401	0.0951	0.001083974	0.3696	0.00065192	0.9125	0.022948311	9.18	9.082	9.14	1.8	Ramp: 0.25 until 1.5, 0.1 until 1.6, 0.05 until 1.8. Chaotic motion began at 1.7
6	2016020501	0.092	0.000935414	0.3558	0.001350926	0.8584	0.012121262	9.57	9.668	9.62	2	Ramp: 0.25 until 1.5, 0.1 until 1.9, 0.05 until 2.0. Chaotic motion began at 1.9. After brought up to 2.0 the chaotic motion persisted for a couple of minutes and then promptly died down to periodic over one potential well
7	2016021201	0.0957	0.000758288	0.3954	0.003361547	0.8698	0.01196662	9.473	9.473	9.47	1.85	Ramp: up from 0 to 1.5 by 0.25, 0.1 until 1.6, 0.05 until 1.85 (chaotic motion observed at 1.80). Test ran at 1.85 until break
8	2016021401	0.09482	0.001435967	0.3746	0.00341687	0.8949	0.00922903	9.668	9.668	9.67	2.2	Ramp: 0.25 until 1.5, 0.05 until 1.7 (showed reaching pattern), 0.1 until 2.0 (because regular periodic motion over other potential well), 0.05 until 2.20 (chaotic motion began at 2.15)
9	2016030401	0.0812	0.00130384	0.357	0.001767767	0.8693	0.017939482	9.227	9.227	9.23	2	Ramp: 0.25 until 1.5 (displayed reaching pattern), 0.05 until 2.0 (chaotic motion began at 1.9)
10	2016030701	0.0943	0.000570088	0.3799	0.002459675	0.8782	0.022041438	9.57	9.668	9.61	1.8	Ramp: 0.25 until 1.5, 0.1 until 1.7 (reaching), 0.05 until 1.8 (1.75 chaotic motion began)

Figure A.1. Data Logbook

APPENDIX B

Fracture Surface Images Taken with 16 Megapixel Camera



Figure B.1. Specimen 1 (2015121701)



Figure B.2. Specimen 2 (2016012002)

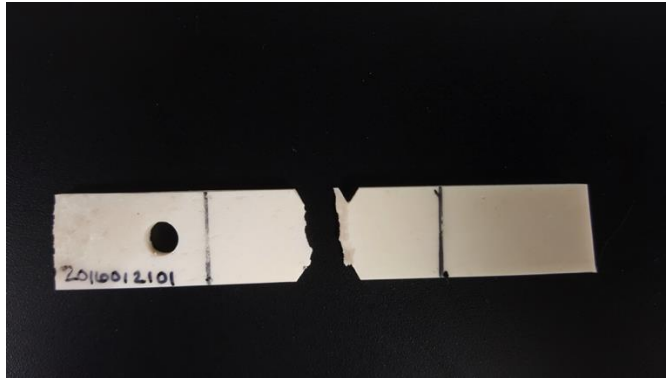


Figure B.3. Specimen 3 (2016012101)



Figure B.4. Specimen 4 (2016012701)



Figure B.5. Specimen 5 (2016020401)

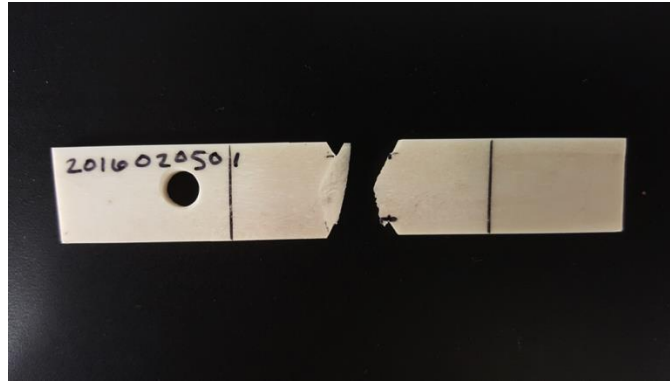


Figure B.6. Specimen 6 (2016020501)



Figure B.7. Specimen 7 (2016021201)



Figure B.8. Specimen 8 (2016021401)

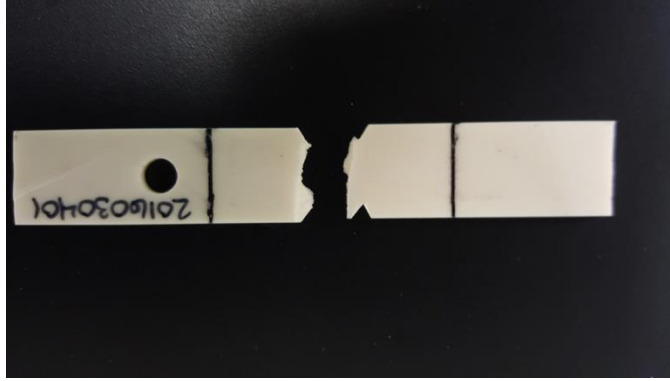


Figure B.9. Specimen 9 (2016030401)

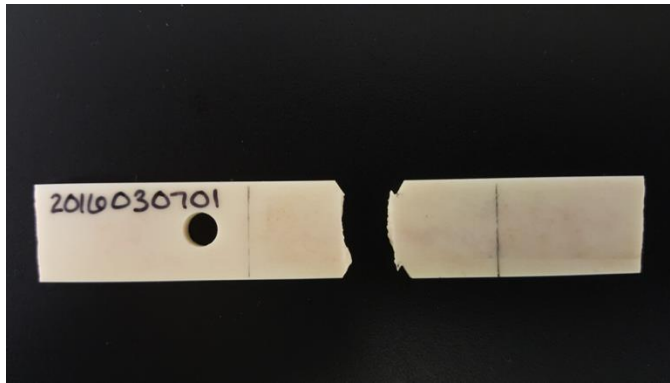


Figure B.10. Specimen 10 (2016030701)

APPENDIX C

Data Summaries

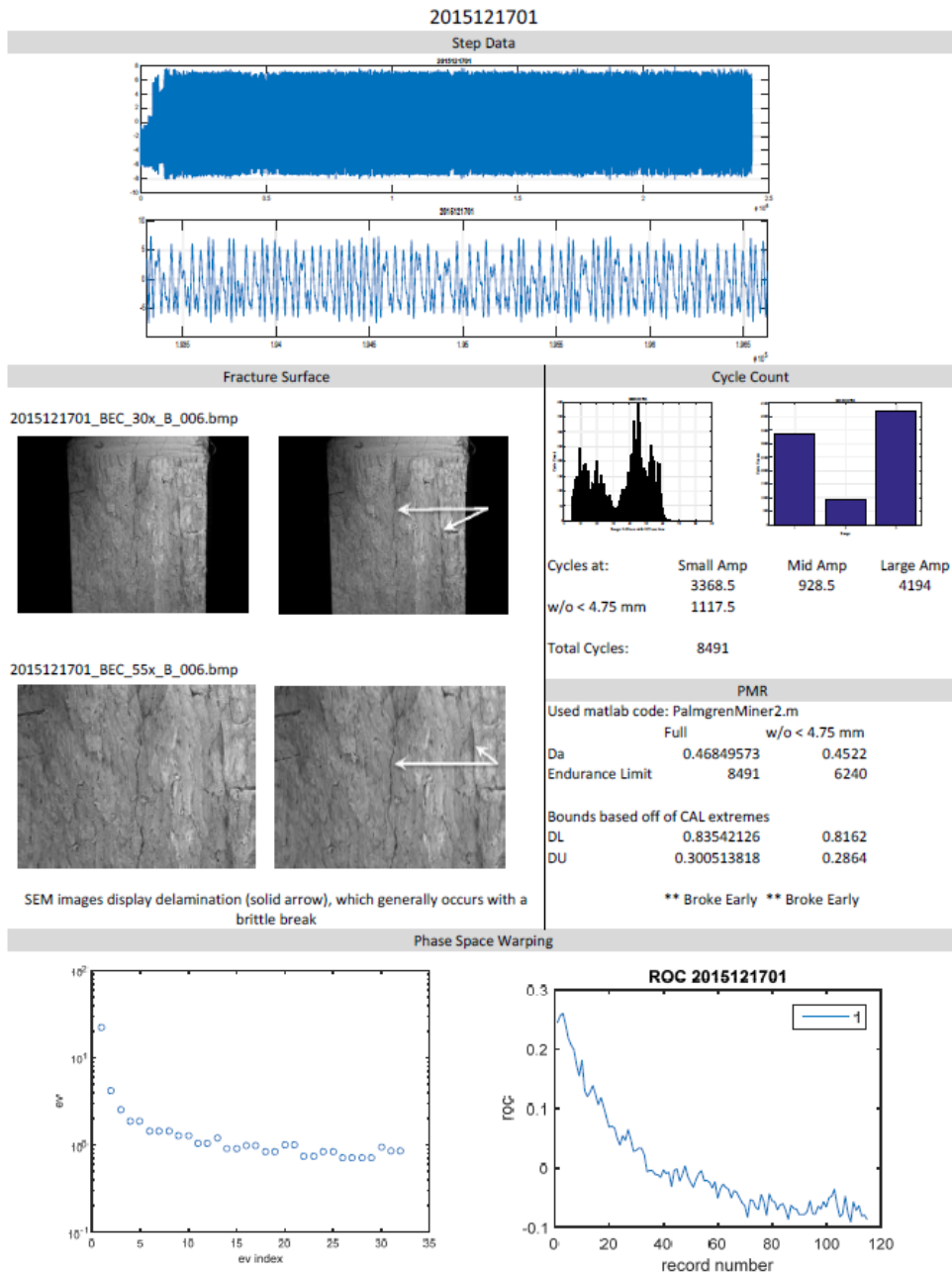
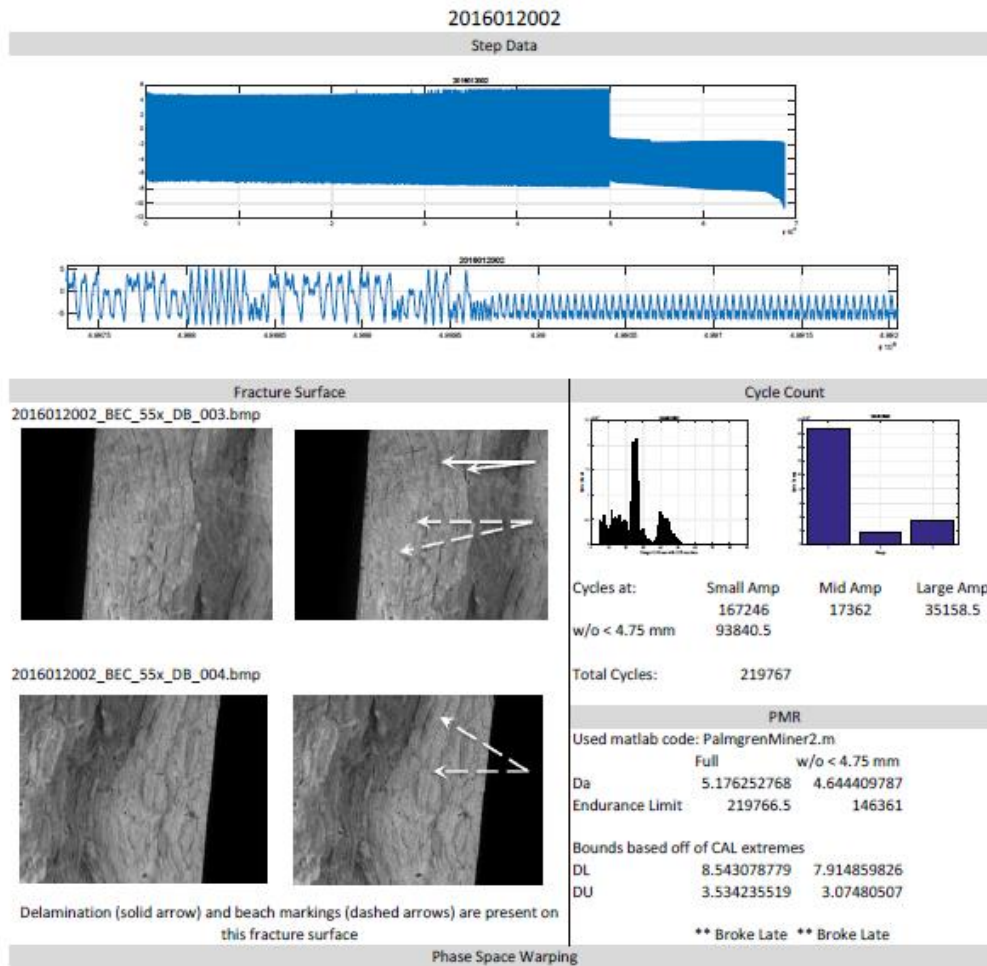


Figure C.1. Specimen 1 (2015121701) Summary



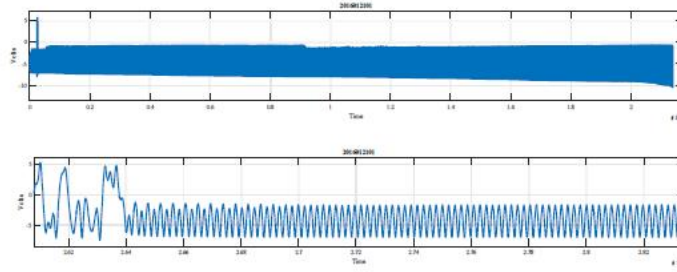
NA

* psw codes wouldn't run because ami did not produce a first minimum - data contaminated

Figure C.2. Specimen 2 (2016012002) Summary

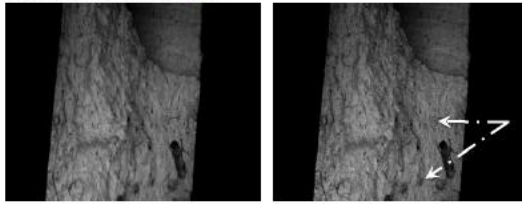
2016012101

Step Data and RFC cycles

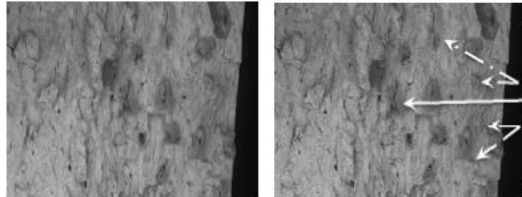


Fracture Surface

2016012101_BEC_30x_001.bmp

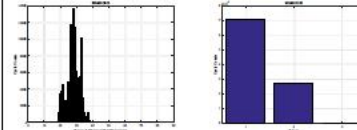


2016012101_BEC_55x_OPO_003.bmp



Osteonal pullout (dash and dot arrow) and beach markings (dashed arrow) are predominately present. There is some evidence of delamination (solid arrow)

Cycle Count



Cycles at:	Small Amp	Mid Amp	Large Amp
w/o < 4.75 mm	70507.5	27380	19.5
	69060		
Total Cycles:	97907		

PMR

Used matlab code: PalmgrenMiner2.m

	Full	w/o < 4.75 mm
Da	1.203657917	1.1932
Endurance Limit	97907	96460
Bounds based off of CAL extremes		
DL	1.60763105	1.5952
DU	0.856991726	0.8479

** Rule worked ** Rule worked

Phase Space Warping

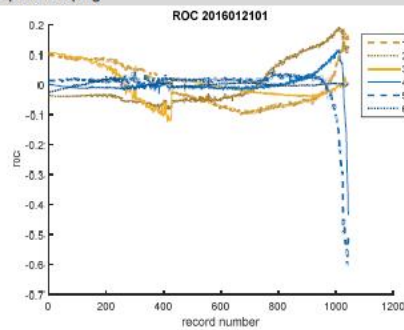
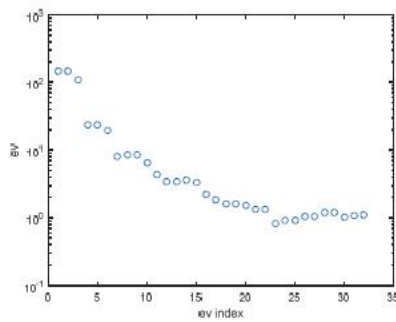
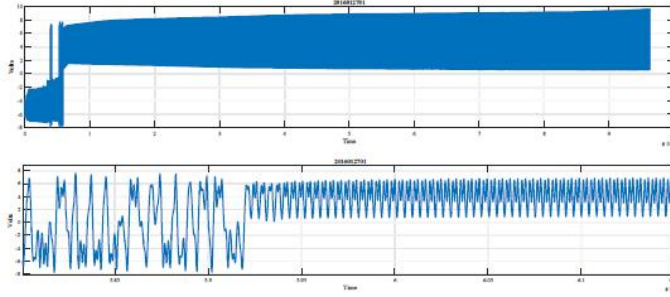


Figure C.3. Specimen 3 (2016012101) Summary

2016012701
Step Data and RFC cycles



Fracture Surface		Cycle Count																	
2016012701_BEC_55x_OPO_001.bmp																			
2016012701_BEC_55x_D_005L.bmp		<table border="1"> <tr> <td>Cycles at:</td> <td>Small Amp</td> <td>Mid Amp</td> <td>Large Amp</td> </tr> <tr> <td></td> <td>15319.5</td> <td>31140.5</td> <td>97.5</td> </tr> <tr> <td>w/o < 4.75 mm</td> <td>14182.5</td> <td></td> <td></td> </tr> <tr> <td>Total Cycles:</td> <td colspan="3">46557.5</td> </tr> </table>		Cycles at:	Small Amp	Mid Amp	Large Amp		15319.5	31140.5	97.5	w/o < 4.75 mm	14182.5			Total Cycles:	46557.5		
Cycles at:	Small Amp	Mid Amp	Large Amp																
	15319.5	31140.5	97.5																
w/o < 4.75 mm	14182.5																		
Total Cycles:	46557.5																		
PMR																			
Used matlab code: PalmgrenMiner2.m																			
	Full	w/o < 4.75 mm																	
Da	0.906514637	0.8983																	
Endurance Limit	46557.5	45421																	
Bounds based off of CAL extremes																			
DL	1.287121146	1.2774																	
DU	0.573441112	0.5663																	
Osteonal pullout (dash and dotted arrow) and beach markings (dashed arrow) are apparent		** Rule worked ** Rule worked																	

Phase Space Warping

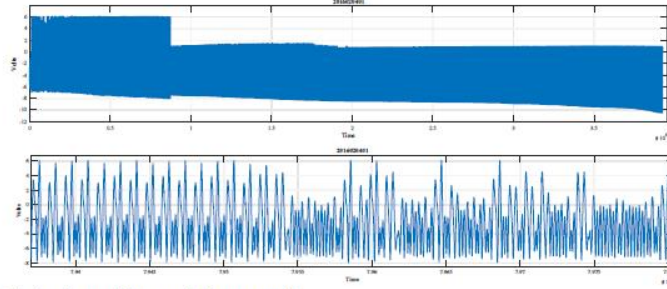
NA

* psw codes ran, but the data was clearly contaminated

Figure C.4. Specimen 4 (2016012701) Summary

2016020401

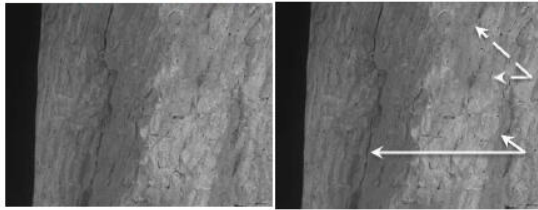
Step Data



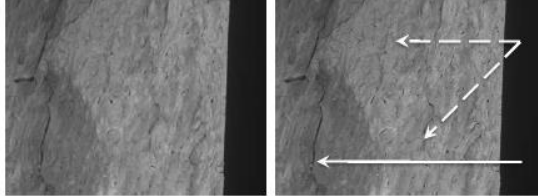
Note: 2nd graph is before the pendulum settled into one well

Fracture Surface

2016020401_BEC_55x_007.bmp

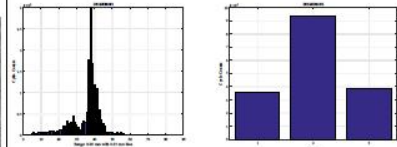


2016020401_BEC_55x_006.bmp



Delamination (solid arrow) and Beach markings (dashed arrow) are present. Also a "swirling pattern" perhaps indicative of a ductile break.

Cycle Count



Cycles at:	Small Amp	Mid Amp	Large Amp
	35345.5	93852	38852
w/o < 4.75 mm	26061.5		

Total Cycles: 168049.5

PMR

Used matlab code: PalmgrenMiner2.m

	Full	w/o < 4.75 mm
Da	6.521064909	6.4538
Endurance Limit	168049.5	158765.5

Bounds based off of CAL extremes

DL	10.89008174	10.8106
DU	4.100272378	4.0422

** Broke late ** Broke late

Phase Space Warping

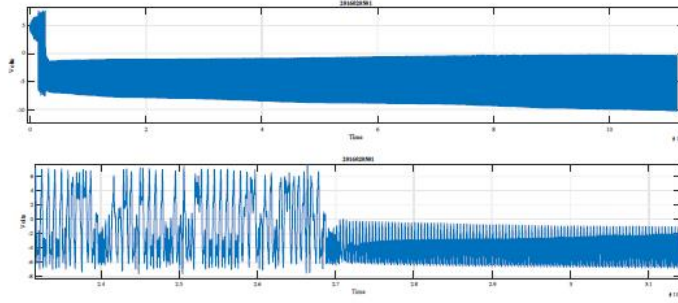
NA

* psw would not run due to no initial minimum with ami... data contaminated

Figure C.5. Specimen 5 (2016020401) Summary

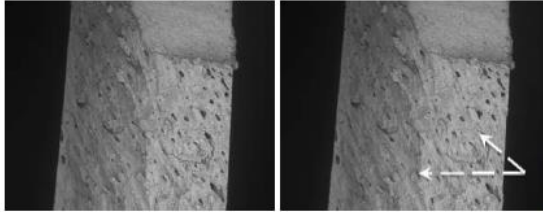
2016020501

Step Data

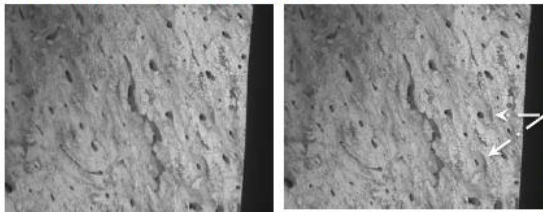


Fracture Surface

2016020501_BEC_35x_DB_006.bmp

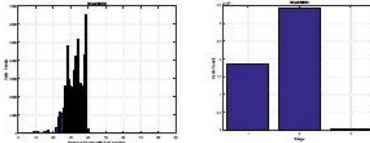


2016020501_BEC_55x_CFB_OPO_005.bmp



Beach markings (dashed arrow) and osteonal pullout (dash and dotted arrow) are present. Break angle in upper image suggest a fast/brittle break.

Cycle Count



Cycles at:	Small Amp	Mid Amp	Large Amp
w/o < 4.75 mm	18686.5	34443.5	136

Total Cycles: 53266

PMR

Used matlab code: PalmgrenMiner2.m

	Full	w/o < 4.75 mm
Da	1.018112805	0.993076759
Endurance Limit	53266	49810.5

Bounds based off of CAL extremes

DL	1.443739906	1.414167045
DU	0.646949831	0.625322543

** Rule worked ** Rule worked

Phase Space Warping

NA

* psw code ran, but the data was clearly contaminated

Figure C.6. Specimen 6 (2016020501) Summary

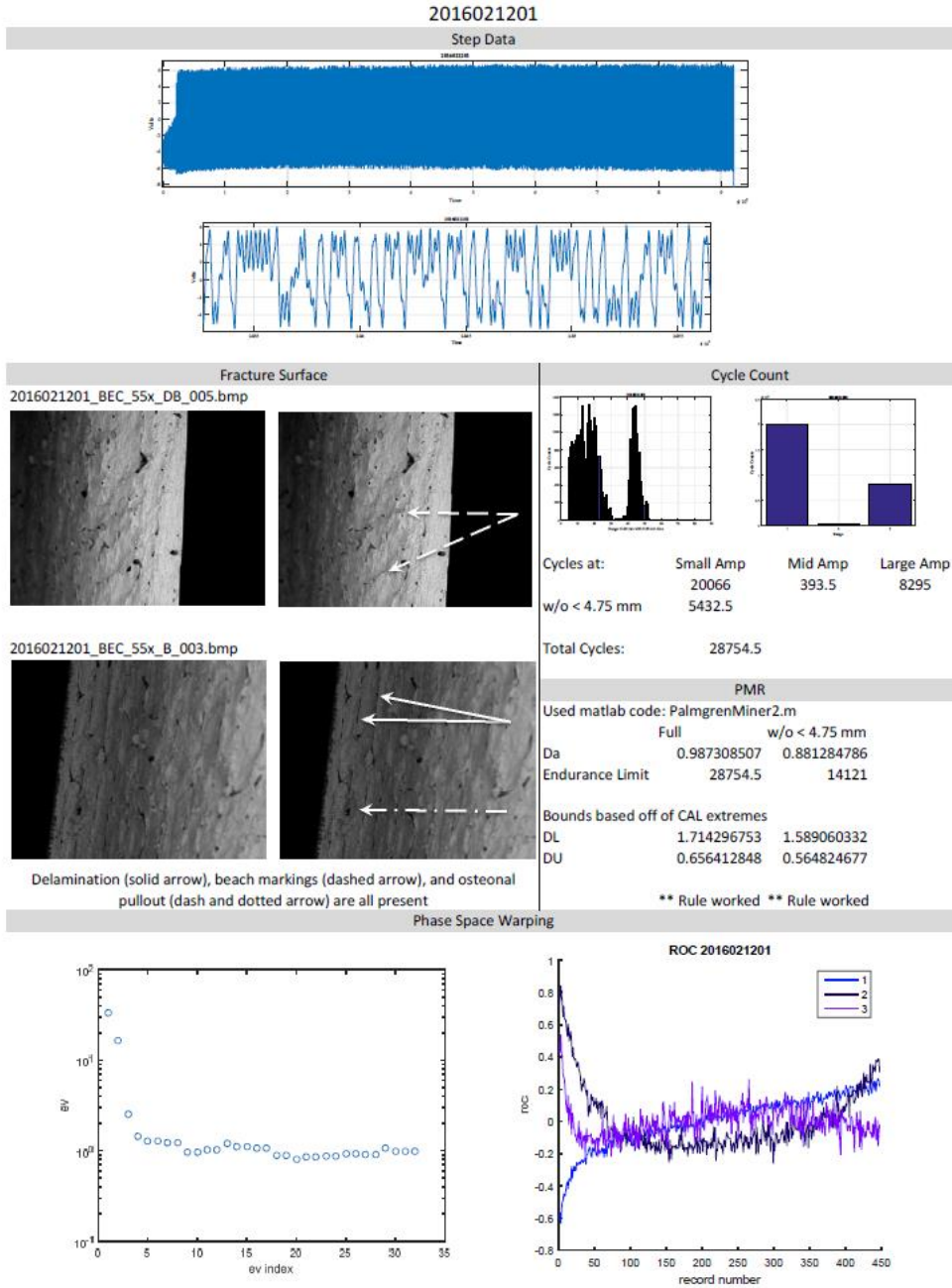


Figure C.7. Specimen 7 (2016021201) Summary

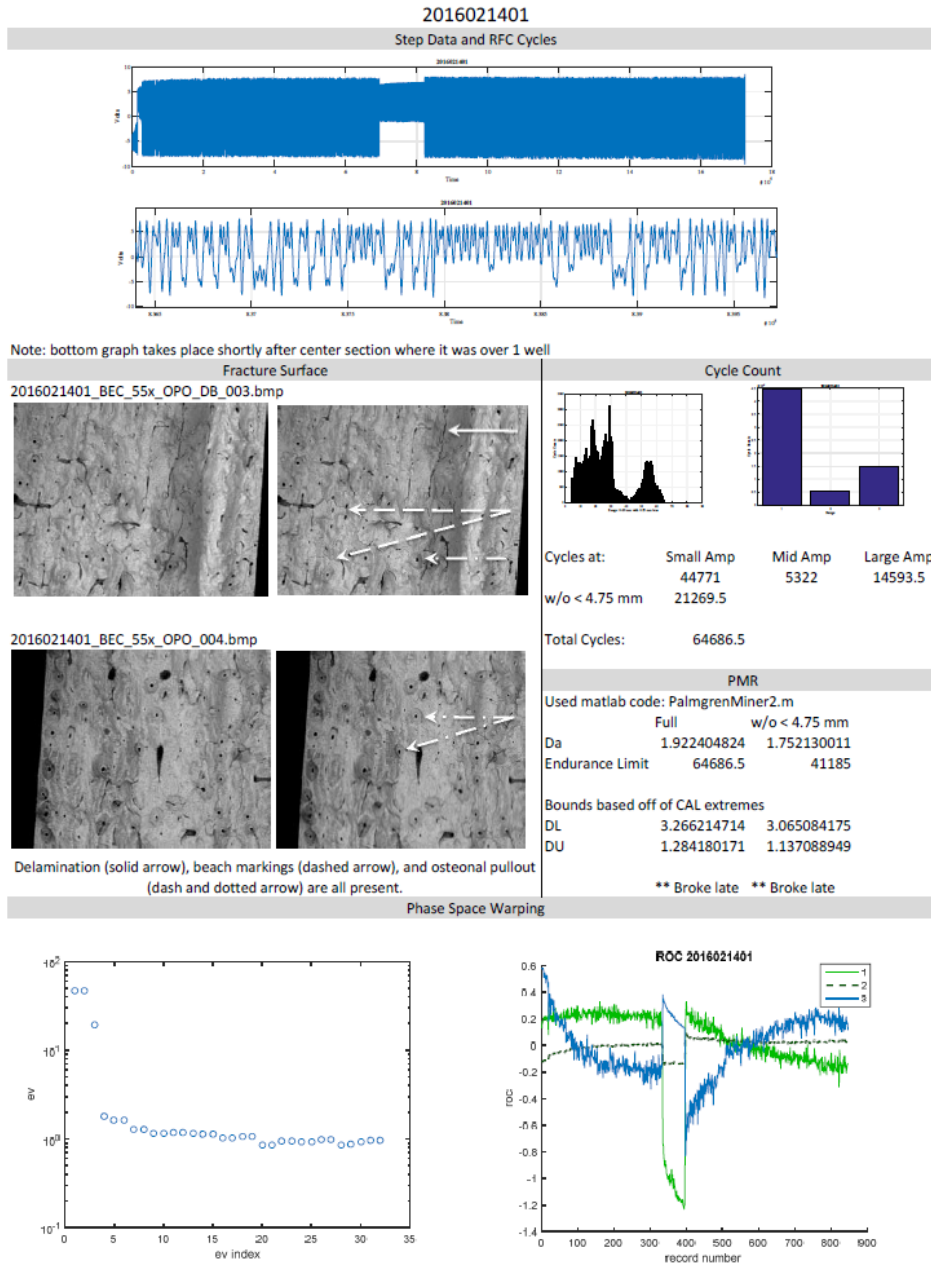
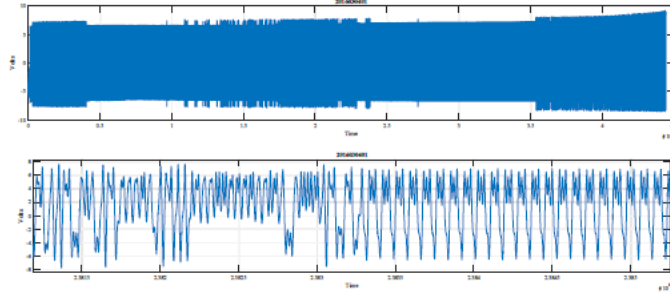


Figure C.8. Specimen 8 (2016021401) Summary

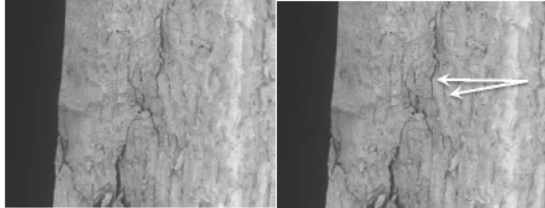
2016030401

Step Data

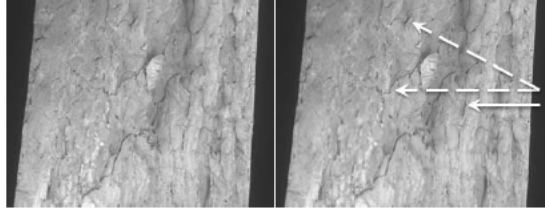


Fracture Surface

2016030401_BEC_55x_DB_002.bmp

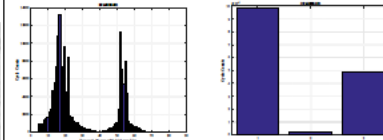


2016030401_BEC_55x_DB_005.bmp



Delamination (solid arrow) and Beach markings (dashed arrow) are present

Cycle Count



Cycles at:	Small Amp	Mid Amp	Large Amp
	97899	1945.5	48546
w/o < 4.75 mm	31494.5		

Total Cycles: 148390.5

PMR

Used matlab code: PalmgrenMiner2.m

	Full	w/o < 4.75 mm
Da	5.627601849	5.146483033
Endurance Limit	148390.5	81986

Bounds based off of CAL extremes

DL	9.852564531	9.284261536
DU	3.713934442	3.298321862

** Broke late ** Broke late

Phase Space Warping

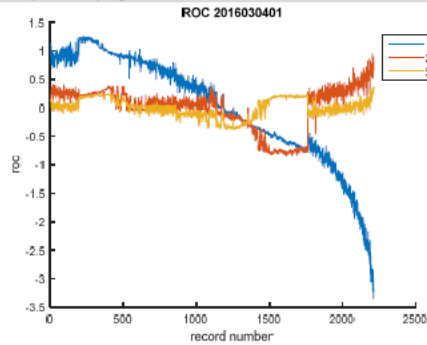
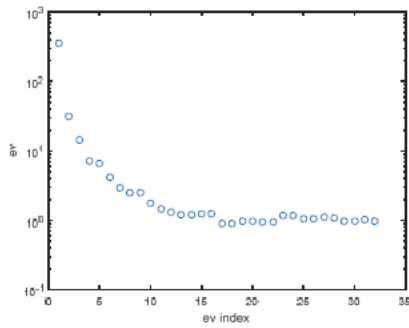
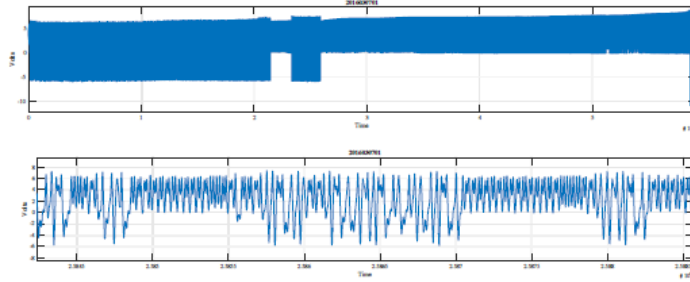


Figure C.9. Specimen 9 (2016030401) Summary

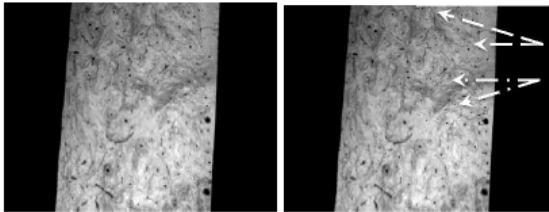
2016030501

Step Data

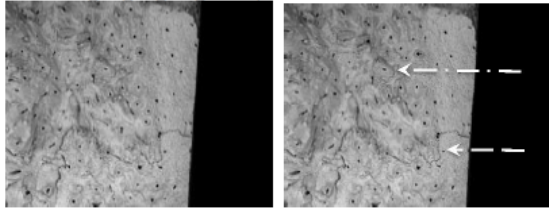


Fracture Surface

2016030701_BEC_30x_003.bmp

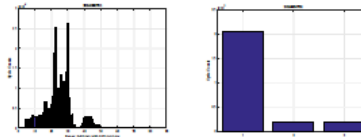


2016030701_BEC_55x_OPO_002.bmp



Beach markings (dashed arrow) and Osteonal pullout (dash dotted arrow) are present

Cycle Count



Cycles at:	Small Amp	Mid Amp	Large Amp
	205378	20077	17521.5
w/o < 4.75 mm	152390		

Total Cycles: 242976.5

PMR

Used matlab code: PalmgrenMiner2.m

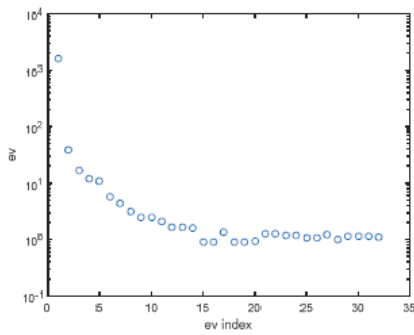
	Full	w/o < 4.75 mm
Da	3.752027793	3.3681152
Endurance Limit	242976.5	189988.5

Bounds based off of CAL extremes

DL	5.719378559	5.265896656
DU	2.698011219	2.366369848

** Broke late ** Broke late

Phase Space Warping



ROC 2016030701

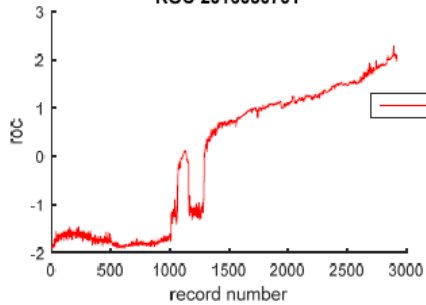


Figure C.10. Specimen 10 (2016030701) Summary

APPENDIX D

MATLAB Code

Resonant Frequency

```
%This program plots the frequency of the .lvm file outputted by LabView  
%It uses the 'RFreadColData.m' file to call in the data file
```

```
clear  
clc
```

```
%Define file you want to call  
fname=input('Laser Data File Name ');
```

```
%Call text and dat files  
%LTo is the Laser original time, Volt is the laser voltage  
[labels,LTo,Volt] = readColData(fname,2,0,0);
```

```
Fs=200;  
t=0:1/Fs;  
x=Volt;  
figure  
pwelch(x,[],[],[],Fs,'onesided');
```

Trim Data File

```
clc
clear all
close all

%Define file you want to call
fname=input('Laser .lvm Data File Name ');
%Define file you want to save
filename = input('Trimmed file .txt Name ');

%Call .lvm file
%LTo is the Laser original time, Volt is the laser voltage
[labels,LTo,Volt] = readColData(fname,2,0,0);

%Set Laser actual time (LT)
%LT is the Laser zeroed time
for x=1:length(LTo)
    LT(x)=LTo(x)-LTo(1);
end

%Zero the voltage outputted by the laser
for x=1:length(Volt)
    V(x)=Volt(x)-Volt(1);
end

VV=reshape(V,length(V),1);

%Graph all figures
figure;
%Plot
plot(LT,VV,'r');
xlabel('Time (sec)');
ylabel('Volt');
title('Volt vs Time');
axis tight;

%What needs to be trimmed?
Dbefore = input('Delete data before time ');
Dafter = input('Delete data after time ');

%Trim using index
[~,idxDb] = ismember(Dbefore,LTo); [~,idxDa] = ismember(Dafter,LTo);
LT = LTo(idxDb:idxDa)';
TVolt = Volt(idxDb:idxDa)';
Data = [LT; TVolt];

%Save as .txt file
fid=fopen(filename,'w');
fprintf(fid,'%12.3f %12.6f\r\n',Data);
fclose(fid);
```

Retrieve Column Data from File

```
function[labels,LTo,Volt] = readColData(fname,ncols,nhead,nlrows)
% readColData reads data from a file containing data in columns
%           that have text titles, and possibly other header text
%
% Synopsis:
%   [labels,x,y] = readColData(fname)
%   [labels,x,y] = readColData(fname,ncols)
%   [labels,x,y] = readColData(fname,ncols,nhead)
%   [labels,x,y] = readColData(fname,ncols,nhead,nlrows)
%
% Input:
%   fname = name of the file containing the data (required)
%   ncols = number of columns in the data file. Default = 2.
%           A value of ncols is required only if nlrows is also
%           specified.
%   nhead = number of lines of header information at the very top of
%           the file. Header text is read and discarded. Default = 0
%           A value of nhead is required only if nlrows is also
%           specified.
%   nlrows = number of rows of labels. Default = 1
%
% Output:
%   labels = matrix of labels. Each row of labels is a different
%           label from the columns of data. The number of columns
%           in the labels matrix equals the length of the longest
%           column heading in the data file. More than one row of
%           labels is allowed. In this case the second row of
%           column headings begins in row ncol+1 of labels. The
%           third row column headings begins in row 2*ncol+1 of
%           labels, etc.
%
%           NOTE: Individual column headings must not contain blanks
%
%   x = column vector of x values
%   y = matrix of y values. y has length(x) rows and ncols columns
%
% Author:
%   Gerald Recktenwald, gerry@me.pdx.edu
%   Portland State University, Mechanical Engineering Department
%   24 August 1995
%
% Modified by: Abbey Campbell and Shelly Cler 2015
%
% process optional arguments
if nargin < 4
    nlrows = 0; % default
    if nargin < 3
        nhead = 0; % default
        if nargin < 2
            ncols = 2; % default
        end
    end
end
end
```

```

% open file for input, include error handling
fin = fopen(fname,'r');
if fin < 0
    error(['Could not open ',fname,' for input']);
end

% Preliminary reading of titles to determine number of columns
% needed in the labels matrix. This allows for an arbitrary number
% of column titles with unequal (string) lengths. We cannot simply
% append to the labels matrix as new labels are read because the first
% label might not be the longest. The number of columns in the labels
% matrix (= maxlen) needs to be set properly from the start.

% Read and discard header text one line at a time
for i=1:nhead, buffer = fgetl(fin); end

maxlen = 0;
for i=1:nlrows
    buffer = fgetl(fin);           % get next line as a string
    for j=1:ncols
        [next,buffer] = strtok(buffer);       % parse next column label
        maxlen = max(maxlen,length(next));   % find the longest so far
    end
end

end

% Set the number of columns in the labels matrix equal to the length
% of the longest column title. A complete preallocation (including
% rows) of the label matrix is not possible since there is no string
% equivalent of the ones() or zeros() command. The blank() command
% only creates a string row vector not a matrix.
labels = blanks(maxlen);

frewind(fin); % rewind in preparation for actual reading of labels
and data

% Read and discard header text on line at a time
for i=1:nhead, buffer = fgetl(fin); end

% Read titles for keeps this time
for i=1:nlrows

    buffer = fgetl(fin);           % get next line as a string
    for j=1:ncols
        [next,buffer] = strtok(buffer);       % parse next column label
        n = j + (i-1)*ncols;                 % pointer into the label
array for next label
        labels(n,1:length(next)) = next;     % append to the labels
matrix
    end
end

% Read in the x-y data. Use the vetorized fscanf function to load all
% numerical values into one vector. Then reshape this vector into a
% matrix before copying it into the x and y matrices for return.

```

```

data = fscanf(fin, '%f'); % Load the numerical values into one long
vector

nd = length(data);      % total number of data points
nr = nd/ncols;         % number of rows; check (next statement) to
make sure
if nr ~= round(nd/ncols)
    fprintf(1, '\ndata: nrow = %f\tncol = %d\n', nr, ncols);
    fprintf(1, 'number of data points = %d does not equal
nrow*ncol\n', nd);
    error('data is not rectangular')
end

data = reshape(data,ncols,nr)'; % notice the transpose operator

LTo = data(:,1);
Volt = data(:,2);

% end of readColData.m

```

Rainflow Counting with 0.25 mm Bins

```
% This code creates the histogram with 0.1 mm bin sizes
%Creator info
%
% rainflow_bins.m ver 2.1 September 20, 2013
% by Tom Irvine Email: tom@vibrationdata.com
% ASTM E 1049-85 (2005) Rainflow Counting Method
%
% What follows is a modified version of Mr. Irvine's code
%
close all;
clear all;
%
%To know how long the code took to run
tic
%
fig_num=1;
%
%Define file you want to call
fname = input('Laser Data File Name ');
fname2 = fname(1:10);
%Call .lvm file
[labels,LTo,Volt] = readColData(fname,2,0,0);
    %LTo is the Laser original time, Volt is the laser voltage
%
y=double(Volt);
m=length(y)-1;
a=zeros(m,1); % max and mins
t=zeros(m,1); % loc a
a(1)=y(1);
t(1)=1;
k=2;
%
%Slope calculation
% TO SPEED UP MAYBE CHANGE TO DIFF( <-----
-----
slope1=(y(2)-y(1));
for i=2:m
    slope2=(y(i+1)-y(i));
    if((slope1*slope2)<=0)
        a(k)=y(i);
        t(k)=i;
        k=k+1;
    end
    slope1=slope2;
end
%
a(k)=y(m+1);
t(k)=t(k-1)+1;
k=k+1;
%
clear temp;
temp(1:k-1)=a(1:k-1);
clear a;
```

```

a=temp;
%
clear temp;
temp(1:k-1)=t(1:k-1);
clear t;
t=temp;
%
% ensuring column vector
sza=size(a);
if(sza(2)>sza(1))
    a=a';
end
szt=size(t);
if(szt(2)>szt(1))
    t=t';
end
aa=[t a];
%
%%%%%%%%%%%%%%%%%%%%%%%%%%%%%%%%%%%%%%%%%%%%%%%%%%%%%%%%%%%%%%%%%%%%%%%%
%%
% Rules for this method are as follows: let X denote
% range under consideration; Y, previous range adjacent to X
%%%%%%%%%%%%%%%%%%%%%%%%%%%%%%%%%%%%%%%%%%%%%%%%%%%%%%%%%%%%%%%%%%%%%%%%
%%
%
n=1;
i=1;
j=2;
%
aamax=0;
B=zeros(m,4);
a_mean=zeros(m,2);
kv=1;
msa_orig=max(size(aa));
% matrix of cycles
while(1)
    msa=max(size(aa)); % # rows in aa (continually
decreasing)...
%
    if((j+1)>=msa) % 1 value at start or at the
        break;
end --> exit loop
end
    if((i+1)>=msa)
        break;
    end
%
    Y=(abs(aa(i,2)-aa(i+1,2))); % Prev. R
    X=(abs(aa(j,2)-aa(j+1,2))); % Consider
%
    if(Y<=1) % clear noise
        aa(i,:)=[];
        i=1;
        j=2;
    else
        if(X<=1)
            aa(j:j+1,:)=[];

```

```

        i=1;
        j=2;
    else                                     % create matrix for bin sorting
        B(kv,2)=0.5;
        am=[aa(i,2) aa(i+1,2)];
        B(kv,3)=am(1);
        B(kv,4)=am(2);
        aa(1,:)=[];
        B(kv,1)=Y;
        if(Y>aamax)
            p1=aa(i,2);
            p2=aa(i+1,2);
            tp1=aa(i,1);
            tp2=aa(i+1,1);
            aamax=Y;
        end
        kv=kv+1;
        i=1;
        j=2;
    end
end
end
%
% Count each range that has not been previously counted
%
N=max(size(aa));
disp(' ');
for i=(N-1)
    Y=(abs(aa(i,2)-aa(i+1,2)));
    %
    if(Y>1)
        B(kv,1)=Y;
        B(kv,2)=0.5;
        am=[aa(i,2) aa(i+1,2)];
        B(kv,3)=am(1);
        B(kv,4)=am(2);
        if(Y>aamax)
            p1=aa(i,2);
            p2=aa(i+1,2);
            tp1=aa(i,1);
            tp2=aa(i+1,1);
            aamax=Y;
        end
        kv=kv+1;
    end
end
end
%
%Bin sorting
% amax=max(B(:,1));
% recall, 1 V = 1 mm
L = [0:0.25:20];
%
num=max(size(L))-1;
C=zeros(num,1);
%
AverageMean=zeros(num,1);
MaxMean=ones(num,1);

```

```

MinMean=ones (num, 1);
%
MaxPeak=ones (num, 1);
MinValley=ones (num, 1);
%
MaxAmp=zeros (num, 1);
AverageAmp=zeros (num, 1);
%
kvn=kv-1;
%
for i=1:kvn
    for ijk=1:num
        Y=B(i, 1);
        if(Y>=L(ijk) && Y<=L(ijk+1))
            C(ijk)=C(ijk)+B(i, 2);
            bm=(B(i, 3)+B(i, 4))/2;
            if(B(i, 3)>MaxPeak(ijk))
                MaxPeak(ijk)=B(i, 3);
            end
            if(B(i, 4)>MaxPeak(ijk))
                MaxPeak(ijk)=B(i, 4);
            end
            if(B(i, 3)<MinValley(ijk))
                MinValley(ijk)=B(i, 3);
            end
            if(B(i, 4)<MinValley(ijk))
                MinValley(ijk)=B(i, 4);
            end
        end
        %
        AverageAmp(ijk)=AverageAmp(ijk)+B(i, 1)*B(i, 2);
        AverageMean(ijk)=AverageMean(ijk)+bm*B(i, 2);
        %
        if( bm > MaxMean(ijk))
            MaxMean(ijk)=bm;
        end
        if( bm < MinMean(ijk))
            MinMean(ijk)=bm;
        end
        %
        if(B(i, 1)>MaxAmp(ijk))
            MaxAmp(ijk)=B(i, 1);
        end
    end
end
for ijk=1:num
    if( C(ijk)>0)
        AverageAmp(ijk)=AverageAmp(ijk)/C(ijk);
        AverageMean(ijk)=AverageMean(ijk)/C(ijk);
    end
end
%
N=max(size(C));
BIG=zeros(N, 10);
disp(' ');
disp('      Range = (peak-valley) ');
disp(' Amplitude = (peak-valley)/2 ');

```

```

disp(' ');
disp('          Range Limits          Cycle          Average          Max
Min      Average  Max  Min      Max ');
disp('          (units)          Counts          Amp          Amp
Mean      Mean      Mean Valley Peak');
%
MaxAmp=MaxAmp/2;
AverageAmp=AverageAmp/2;
%
for i=1:N
    j=N+1-i;
%
    if(C(j)==0)
        AverageAmp(j)=0.;
        MaxAmp(j)=0.;
        MinMean(j)=0.;
        AverageMean(j)=0.;
        MaxMean(j)=0.;
        MinValley(j)=0.;
        MaxPeak(j)=0.;
    end
%
    out1=sprintf('\t %7.4g to %7.4g \t %g \t %6.3g \t %6.3g \t
%6.3g\t %6.3g\t %6.3g\t %6.3g\t
%6.3g',L(j),L(j+1),C(j),AverageAmp(j),MaxAmp(j),MinMean(j),AverageMean(
j),MaxMean(j),MinValley(j),MaxPeak(j));
%
    disp(out1);
    BIG(i,1)=L(j);
    BIG(i,2)=L(j+1);
    BIG(i,3)=C(j);
    BIG(i,4)=AverageAmp(j);
    BIG(i,5)=MaxAmp(j);
    BIG(i,6)=MinMean(j);
    BIG(i,7)=AverageMean(j);
    BIG(i,8)=MaxMean(j);
    BIG(i,9)=MinValley(j);
    BIG(i,10)=MaxPeak(j);
end
%
out1=sprintf('\n Max Range=%6.3g ',aamax);
disp(out1);
%
TC=sum(C);
%
out1=sprintf('\n Total Cycles =%g \n',TC);
disp(out1);
disp(' ');
%
fig_num=1;
figure(fig_num);
fig_num=fig_num+1;
plot(y);
grid on;
%
figure(fig_num);
fig_num=fig_num+1;

```

```
h=bar(C);
grid on;
title(fname2);
ylabel('Cycle Counts');
xlabel('Range: 0-20 mm with 0.25 mm bins');
set(gca, 'FontName', 'Times New Roman');
%
toc
```

Rainflow Counting with 3 Amplitude Bins

```
% This code creates the histogram with 3 bins
close all;
clear all;
%Creator info
%
% rainflow_bins.m ver 2.1 September 20, 2013
% by Tom Irvine Email: tom@vibrationdata.com
% ASTM E 1049-85 (2005) Rainflow Counting Method
%
% What follows is a modified version of Mr. Irvine's code
%
close all;
clear all;
%
%To know how long the code took to run
tic
%
fig_num=1;
%
%Define file you want to call
fname = input('Laser Data File Name ');
filename = fname(1:10);
%Call .lvm file
[labels,LTo,Volt] = readColData(fname,2,0,0);
    %LTo is the Laser original time, Volt is the laser voltage
%
y=double(Volt);
m=length(y)-1;
a=zeros(m,1); % for max and mins
t=zeros(m,1); % for loc a
a(1)=y(1);
t(1)=1;
k=2;
%
%Slope calculation
% TO SPEED UP MAYBE CHANGE TO DIFF( <-----
-----
slope1=(y(2)-y(1));
for i=2:m
    slope2=(y(i+1)-y(i));
    if((slope1*slope2)<=0)
        a(k)=y(i); % max and mins
        t(k)=i; % loc a
        k=k+1;
    end
    slope1=slope2;
end
%
a(k)=y(m+1);
t(k)=t(k-1)+1;
k=k+1;
%
clear temp;
```

```

temp(1:k-1)=a(1:k-1);
clear a;
a=temp;
%
clear temp;
temp(1:k-1)=t(1:k-1);
clear t;
t=temp;
%
% ensuring column vector
sza=size(a);
if(sza(2)>sza(1))
    a=a';
end
szt=size(t);
if(szt(2)>szt(1))
    t=t';
end
aa=[t a];
%
%{
%%%%%%%%%%%%%%%%%%%%%%%%%%%%%%%%%%%%%%%%%%%%%%%%%%%%%%%%%%%%%%%%%%%%%%%%
%}
figure(fig_num);
fig_num=fig_num+1;
hold on;
%plot(y);
% temp figure to check how the code is working!!!
plot(a, '-o');
hold off;
grid on;
%%%%%%%%%%%%%%%%%%%%%%%%%%%%%%%%%%%%%%%%%%%%%%%%%%%%%%%%%%%%%%%%%%%%%%%%
%}
%
% Rules for this method are as follows: let X denote
% range under consideration; Y, previous range adjacent to X
%
n=1;
i=1;
j=2;
%
aamax=0;
B=zeros(m,4);
a_mean=zeros(m,2);
kv=1;
msa_orig=max(size(aa));
% matrix of cycles
while (1)
    msa=max(size(aa)); % # rows in aa (continually
decreasing)...
%
    if((j+1)>=msa) % 1 value at start or at the
        break;
end --> exit loop
end
if((i+1)>=msa)

```

```

        break;
    end
%
Y=(abs(aa(i,2)-aa(i+1,2)));           % Prev. R
X=(abs(aa(j,2)-aa(j+1,2)));         % Consider
%
    if Y<=1
        aa(i+1,:)=[];                % clear noise
        i=1;
        j=2;
    else
        if X<=1
            aa(j:j+1,:)=[];
            i=1;
            j=2;
        else
            % create matrix for bin sorting
            B(kv,2)=0.5;
            am=[aa(i,2) aa(i+1,2)];
            B(kv,3)=am(1);
            B(kv,4)=am(2);
            aa(1,:)=[];
            B(kv,1)=Y;
            if(Y>aamax)
                p1=aa(i,2);
                p2=aa(i+1,2);
                tp1=aa(i,1);
                tp2=aa(i+1,1);
                aamax=Y;
            end
            kv=kv+1;
            i=1;
            j=2;
        end
    end
end
end
%
%
% Count each range that has not been previously counted
%
N=max(size(aa));
disp(' ');
for i=(N-1)
    Y=(abs(aa(i,2)-aa(i+1,2)));
%
    if(Y>1)
        B(kv,1)=Y;
        B(kv,2)=0.5;
        am=[aa(i,2) aa(i+1,2)];
        B(kv,3)=am(1);
        B(kv,4)=am(2);
        if(Y>aamax)
            p1=aa(i,2);
            p2=aa(i+1,2);
            tp1=aa(i,1);
            tp2=aa(i+1,1);
            aamax=Y;
        end
    end
end

```

```

        kv=kv+1;
    end
end
%}
%
%Bin sorting
% amax=max(B(:,1));
% recall, 1 V = 1 mm
L = [1 7.5 10 20];
%
num=max(size(L))-1;
C=zeros(num,1);
%
AverageMean=zeros(num,1);
MaxMean=ones(num,1);
MinMean=ones(num,1);
%
MaxPeak=ones(num,1);
MinValley=ones(num,1);
%
MaxAmp=zeros(num,1);
AverageAmp=zeros(num,1);
%
kvn=kv-1;
%
for i=1:kvn
    for ijk=1:num
        Y=B(i,1);
        if(Y>=L(ijk) && Y<=L(ijk+1))
            C(ijk)=C(ijk)+B(i,2);
            bm=(B(i,3)+B(i,4))/2;
            if(B(i,3)>MaxPeak(ijk))
                MaxPeak(ijk)=B(i,3);
            end
            if(B(i,4)>MaxPeak(ijk))
                MaxPeak(ijk)=B(i,4);
            end
            if(B(i,3)<MinValley(ijk))
                MinValley(ijk)=B(i,3);
            end
            if(B(i,4)<MinValley(ijk))
                MinValley(ijk)=B(i,4);
            end
        end
%
        AverageAmp(ijk)=AverageAmp(ijk)+B(i,1)*B(i,2);
        AverageMean(ijk)=AverageMean(ijk)+bm*B(i,2);
%
        if( bm > MaxMean(ijk))
            MaxMean(ijk)=bm;
        end
        if( bm < MinMean(ijk))
            MinMean(ijk)=bm;
        end
%
        if(B(i,1)>MaxAmp(ijk))
            MaxAmp(ijk)=B(i,1);
        end
    end
end

```

```

        end
    end
end
for ijk=1:num
    if( C(ijk)>0)
        AverageAmp(ijk)=AverageAmp(ijk)/C(ijk);
        AverageMean(ijk)=AverageMean(ijk)/C(ijk);
    end
end
%
N=max(size(C));
BIG=zeros(N,10);
disp(' ');
disp('      Range = (peak-valley) ');
disp('  Amplitude = (peak-valley)/2 ');
disp(' ');
disp('      Range Limits          Cycle          Average          Max
Min   Average   Max   Min       Max ');
disp('      (units)          Counts          Amp          Amp
Mean   Mean       Mean Valley Peak');
%
MaxAmp=MaxAmp/2;
AverageAmp=AverageAmp/2;
%
for i=1:N
    j=N+1-i;
%
    if(C(j)==0)
        AverageAmp(j)=0.;
        MaxAmp(j)=0.;
        MinMean(j)=0.;
        AverageMean(j)=0.;
        MaxMean(j)=0.;
        MinValley(j)=0.;
        MaxPeak(j)=0.;
    end
%
    out1=sprintf('\t %7.4g to %7.4g \t %g \t %6.3g \t %6.3g \t
%6.3g\t %6.3g\t %6.3g\t %6.3g\t
%6.3g',L(j),L(j+1),C(j),AverageAmp(j),MaxAmp(j),MinMean(j),AverageMean(
j),MaxMean(j),MinValley(j),MaxPeak(j));
%
    disp(out1);
    BIG(i,1)=L(j);
    BIG(i,2)=L(j+1);
    BIG(i,3)=C(j);
    BIG(i,4)=AverageAmp(j);
    BIG(i,5)=MaxAmp(j);
    BIG(i,6)=MinMean(j);
    BIG(i,7)=AverageMean(j);
    BIG(i,8)=MaxMean(j);
    BIG(i,9)=MinValley(j);
    BIG(i,10)=MaxPeak(j);
end
%
out1=sprintf('\n Max Range=%6.3g ',aamax);
disp(out1);

```

```

%
TC=sum(C);
%
out1=sprintf('\n Total Cycles =%g \n',TC);
disp(out1);
disp(' ');
%
figure(fig_num);
fig_num=fig_num+1;
plot(y);
title(filename);
xlabel('Time');
ylabel('Volts');
set(gca, 'FontName', 'Times New Roman');
grid on;
%
figure(fig_num);
fig_num=fig_num+1;
h=bar(C);
grid on;
title(filename);
ylabel('Cycle Counts');
xlabel('Range');
set(gca, 'FontName', 'Times New Roman');
%
toc

```

Palmgren-Miner Rule

```
%Three different swing amplitudes
% they correlate to the previously completed research amplitudes, which
were
% related to the percent of the max stress (Smax)
% S1=0.9*Smax
% S2=0.85*Smax
% S3=0.65*Smax
%
clear all; clc;
%
%Cycles to failure at different amplitudes determined via CAL tests
%N1=Number of cycles to failure under S1
N1=9970;
%N2=Number of cycles to failure under S2
N2=39632;
%N3=Number of cycles to failure under S3
N3=138021;
%
%Cycles at each amplitude during the test with chaotic loading
%n1=Number of cycles under S1
n1=input('Number of cycles run at S1 (Large) ');
%n2=Number of cycles under S2
n2=input('Number of cycles run at S2 (Medium) ');
%n3=Number of cycles under S3
n3=input('Number of cycles run at S3 (Small) ');
%
%Da=sumation of ni/Ni---At the average Endurance Limit
Da=(n1/N1)+(n2/N2)+(n3/N3)
EnduranceLimit=(n1+n2+n3)

% Uncertainty
n1u = (n1/N1)*(4527/N1);
n2u = (n2/N2)*(14517/N2);
n3u = (n3/N3)*(18686/N3);
delDa = sqrt(n1u^2+n2u^2+n3u^3)
```

Phase Space Warping Protocol Code

```
% protocol
%%
% load data and assign it to x
% Define file you want to call
fname = input('Laser Data File Name          ');
filename = fname(1:10);
% Call .lvm file
[labels,LTo,Volt] = readColData(fname,2,0,0);
% remove mean
x1 = Volt-mean(Volt);
% filter signal
d = designfilt('lowpassfir', 'FilterOrder', 100, ...
              'CutoffFrequency', 15, 'SampleRate', 200, ...
              'Window', 'hamming');
x = filtfilt(d,x1);
%
% average mutual information to get delay time
figure
ami(x,8000,60,32); % get delay time
disp(' ')
disp('Assign delay.') % determined from 1st minimum in ami
m = input('enter 1st minimum value          ');
disp(' ')
%
% false nearest neighbors search to get embedding dimension
figure
fnns(x, m, 6, 8000); % get embedding dimension
disp(' ')
disp('Assign embedding dimension.')
d = input('enter dimension when fnns=0      ');
disp(' ')
%
%%
%%%%%%%%%%%%%%%%%%%%%%%%%%%%%%%%%%%%%%%%%%%%%%%%%%%%%%%%%%%%%%%%%%%%%%%%%% Where do these values come
from???
nm = 8000; % decide the reference model size
nb = 32; % decide how many boxes you need in the phase space
nn = 20; % decide how many points to use for local linear model
step = 1; % model prediction time
mtr = 0; % use scalar tracking metric
rl = 2000; % decide how many points you need in each record
n = length(x); % total number of points in your data set (reconstructed
phase space)
nr = floor(n/rl); % decide how many records you need overall
prpr = 1; % 0 if no preprocessing needed, otherwise 1
%
% now get the tracking matrix
Y = psw_cont(x, m, d, nm, nb, nn, step, mtr, rl, nr, prpr);
%
% now analyze tracking matrix using new method
DY = diff(Y);
Y = Y(1:end-1,:);
for k = 1:size(Y,2)
```

```

        Y(:,k) = Y(:,k) - mean(Y(:,k));
        DY(:,k) = DY(:,k) - mean(DY(:,k));
    end
    Syy = Y.'*Y/(size(Y,1)-1);
    Sydy = Y.'*DY/(size(Y,1)-1);
    [P,E] = eig(Syy,Sydy);
    ev = diag(E);
    k = 1;
    Pn = P;
    while k < size(E,2)
        if ~isreal(ev(k))
            Pn(:,k) = (P(:,k) + P(:,k+1))/2;
            Pn(:,k+1) = (P(:,k) - P(:,k+1))/2/1i;
            k = k + 2;
        else
            k = k + 1;
        end
    end
    roc = Y*Pn;
    figure
    semilogy(abs(ev), 'o'), xlabel('ev index'), ylabel('ev')
    figure
    for i = 1:16
        subplot(4,4,i)
        plot(roc(:,i)), xlabel('record number'), ylabel(['roc '
num2str(i)])
        axis tight
    end

    % old analysis
    [U,V,X,C,S] = gsvd(Y,DY);
    soc = fliplr(U*C);
    sov = flipud(diag(C'*C)./diag(S'*S));
    figure
    semilogy(sov, 'o'), xlabel('soc index'), ylabel('sov')
    figure
    for i = 1:16
        subplot(4,4,i)
        plot(soc(:,i)), xlabel('record number'), ylabel(['soc '
num2str(i)])
        axis tight
    end

    %}

```

Phase Space Warping Code Set

The PSW codes developed by Dr. Chelidze with the University of Rhode Island may be accessed at the following website: <http://egr.uri.edu/nld/software/>

APPENDIX E

CAD Drawings

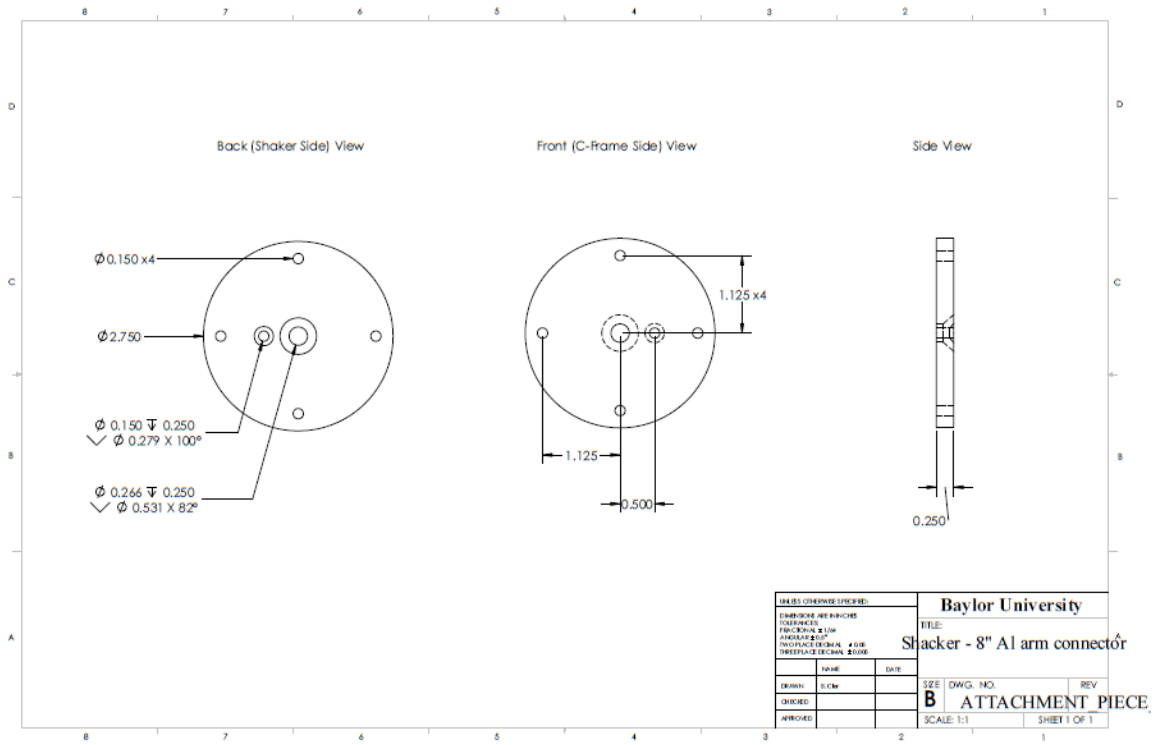


Figure E.1. Shaker converter piece

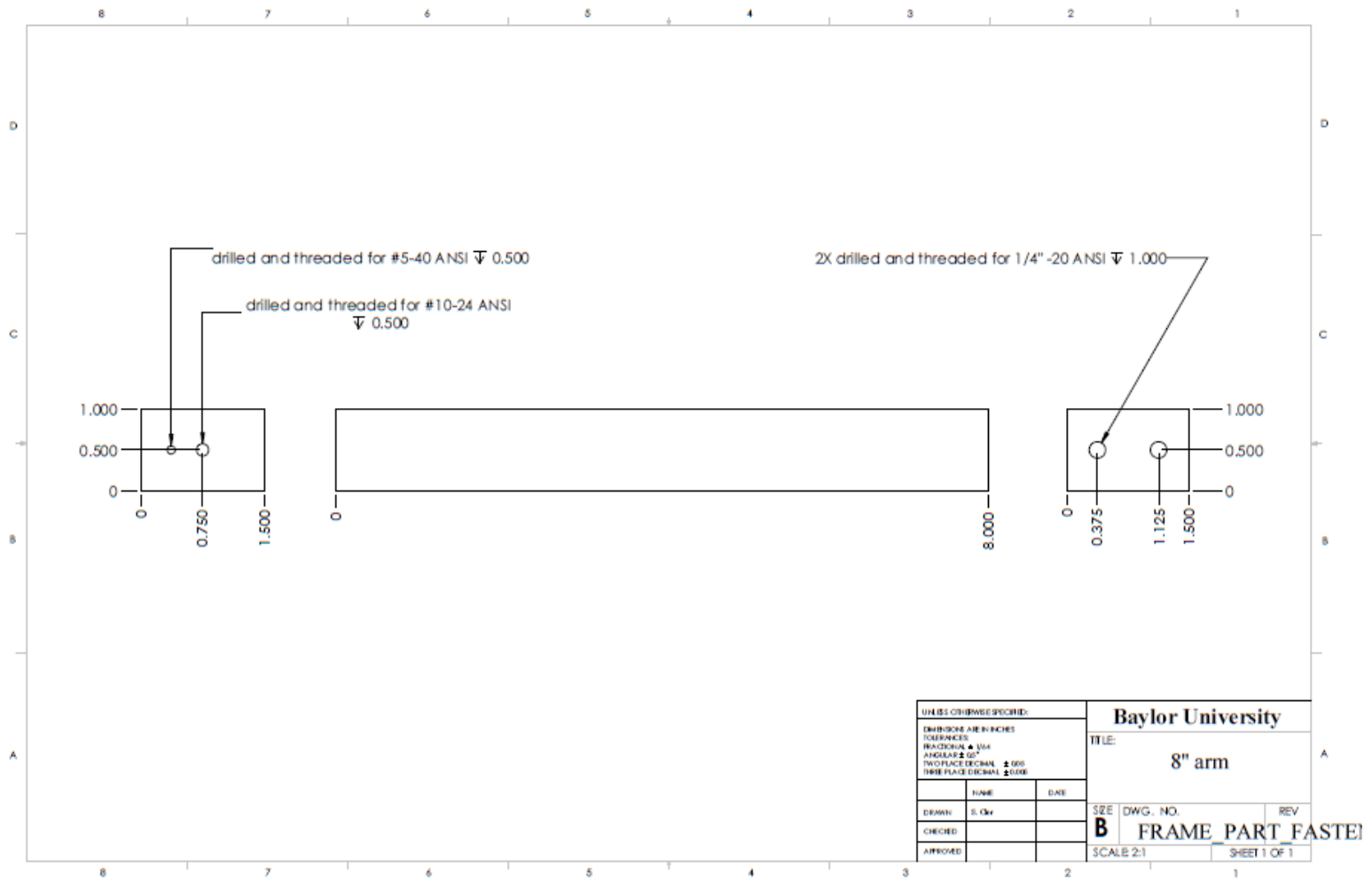


Figure E.2. 8 inch connector arm

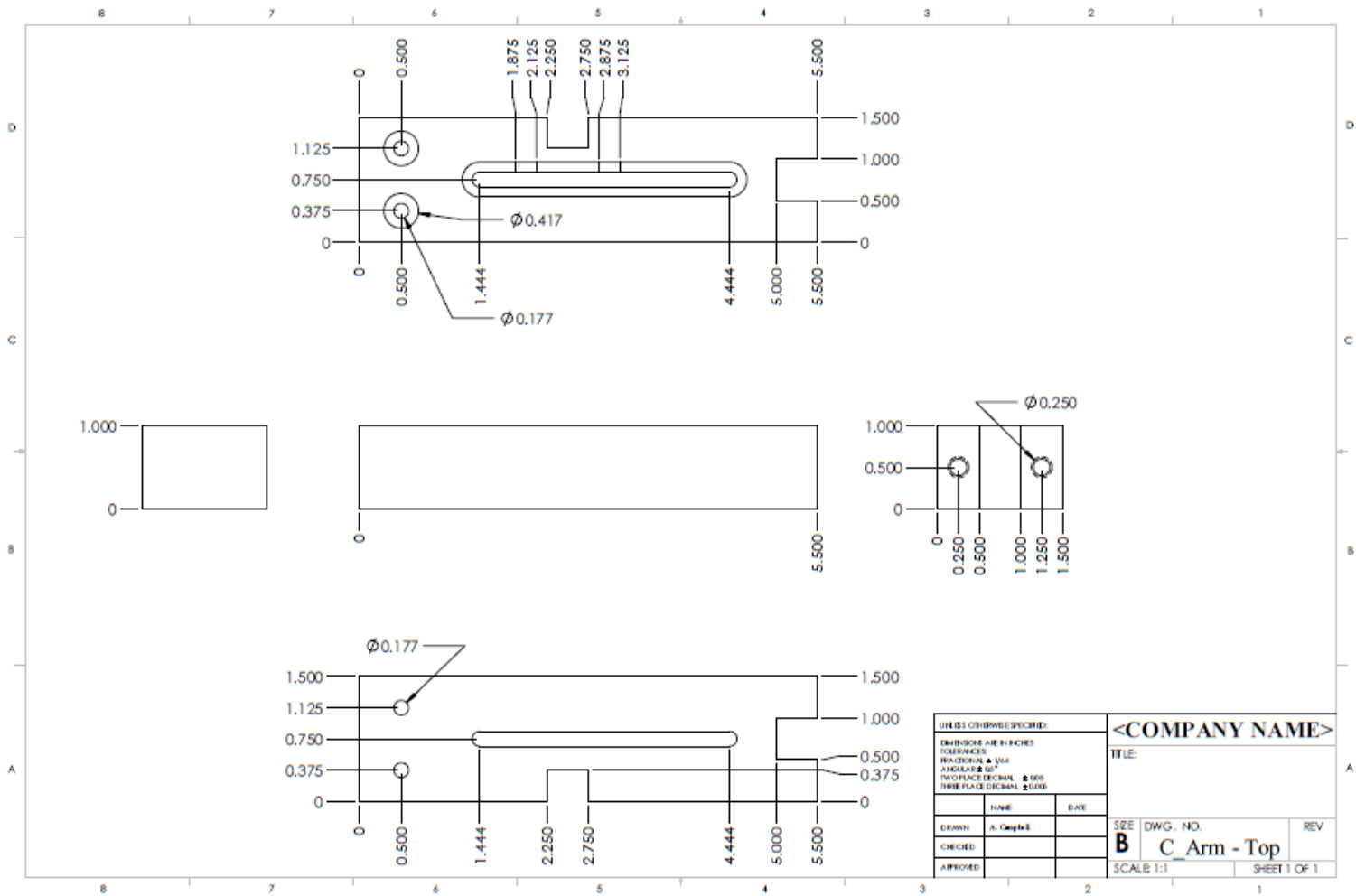


Figure E.3. C-frame top arm

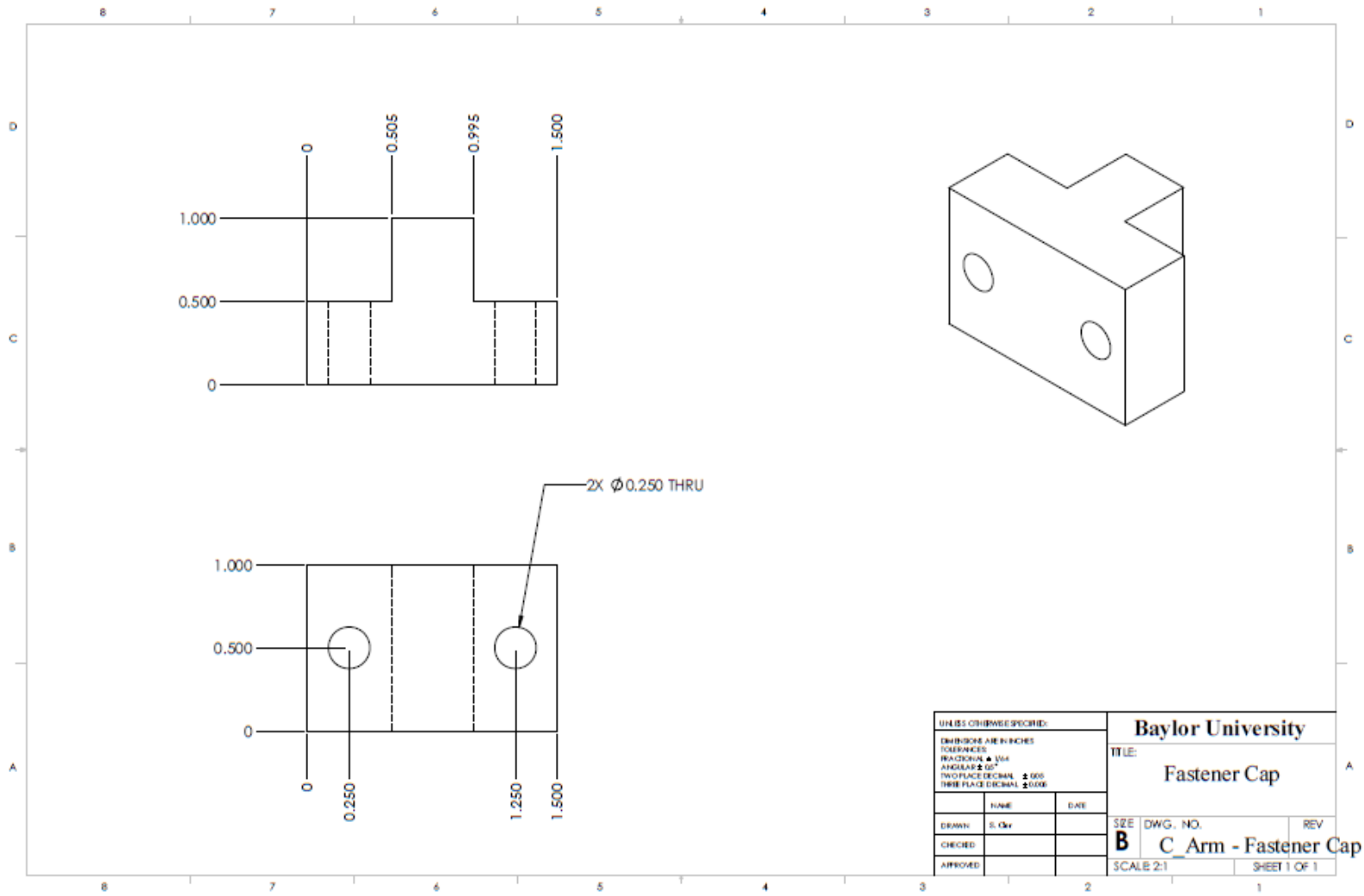


Figure E.4. Fastener cap

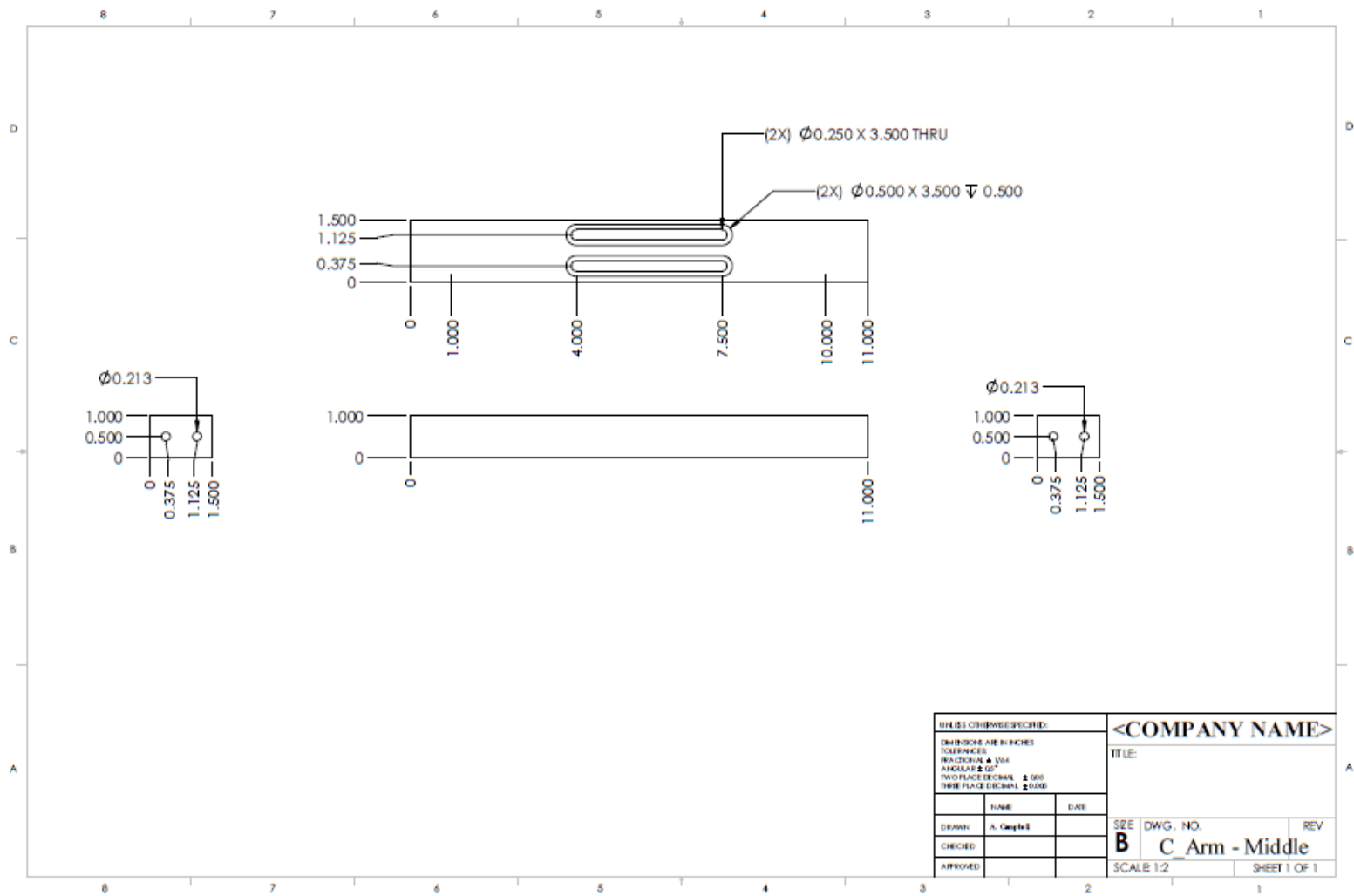


Figure E.5. C-Frame vertical arm

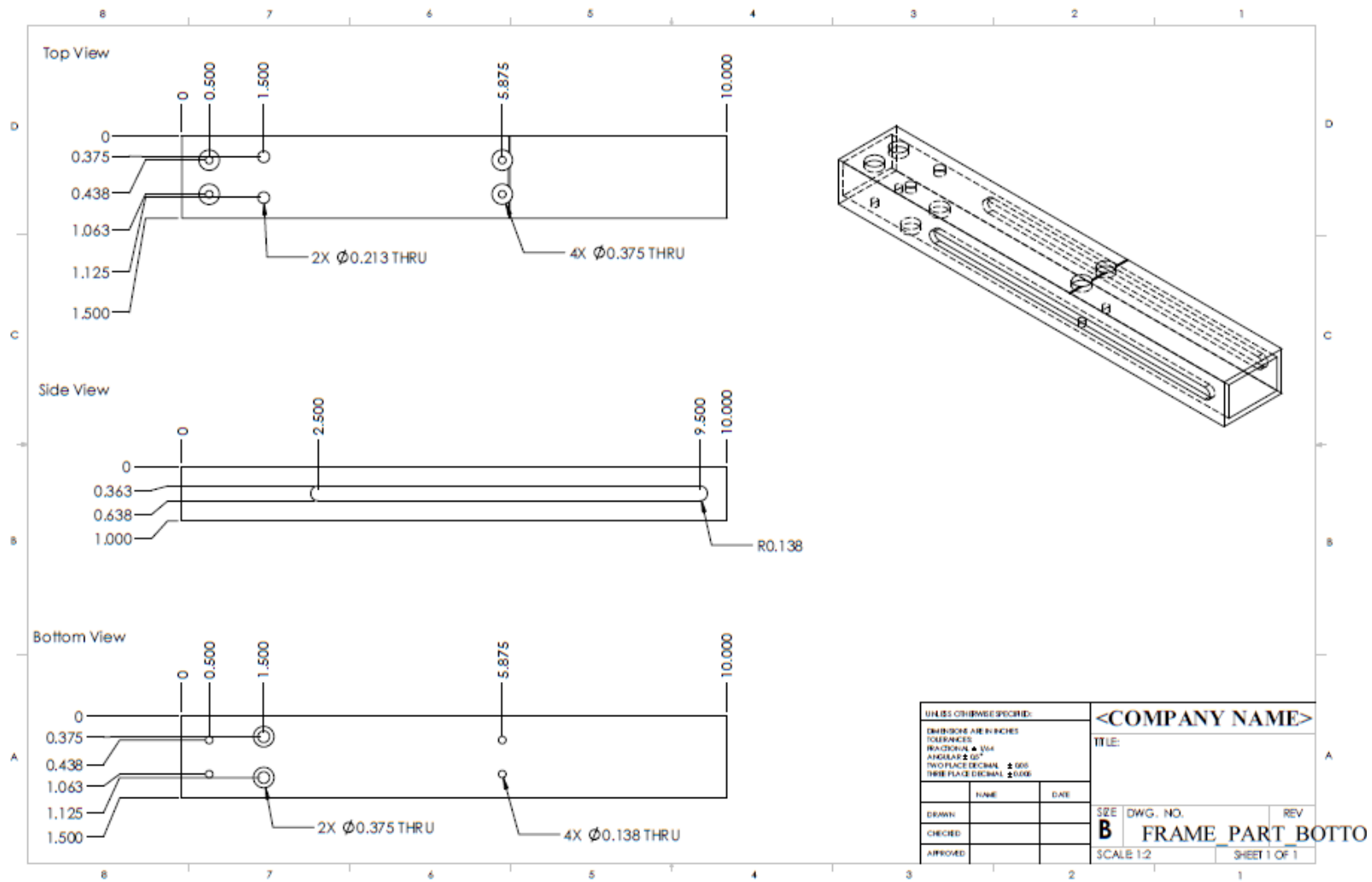


Figure E.6. C-frame base arm

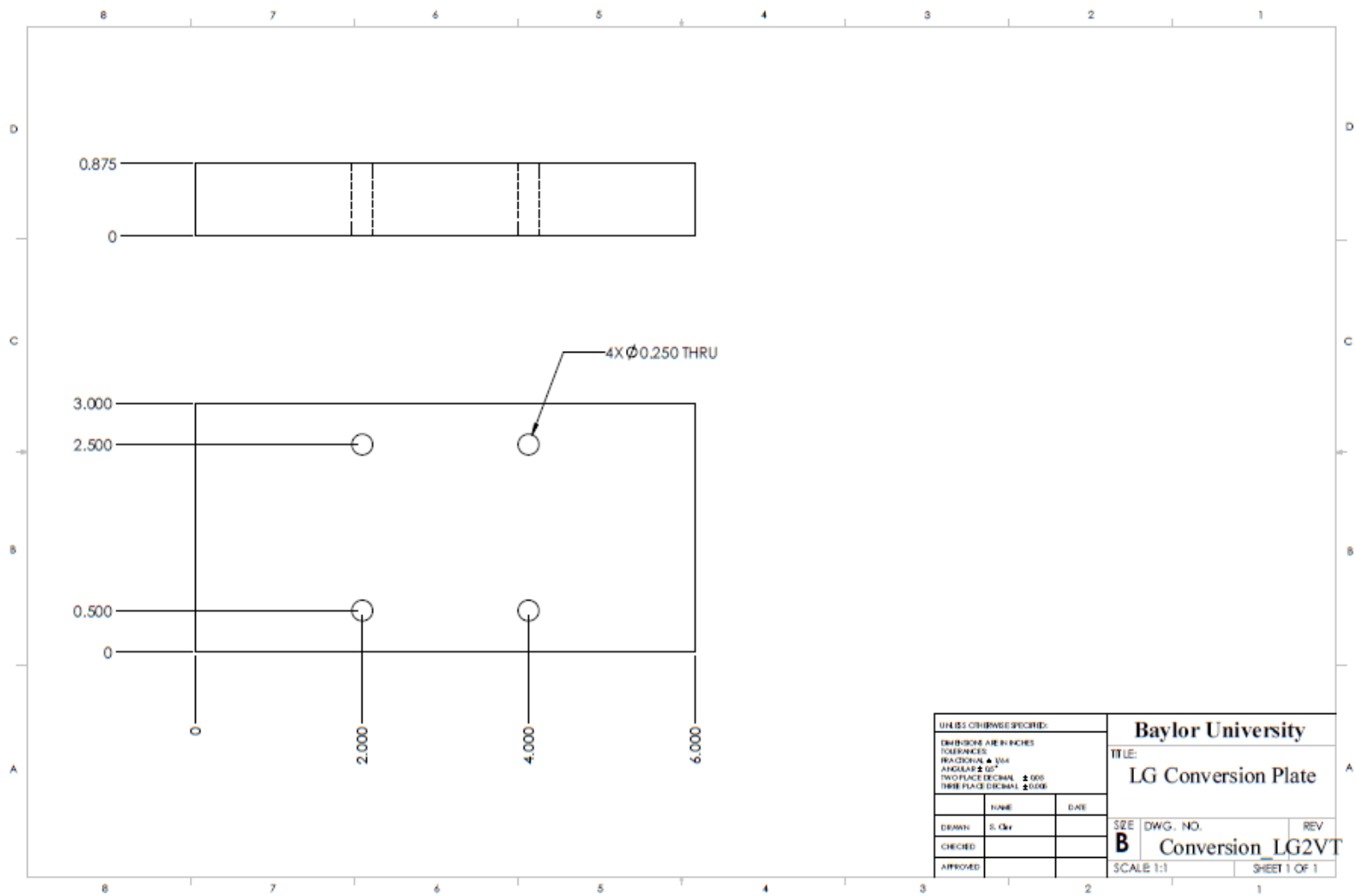


Figure E.7. Linear guide conversion piece

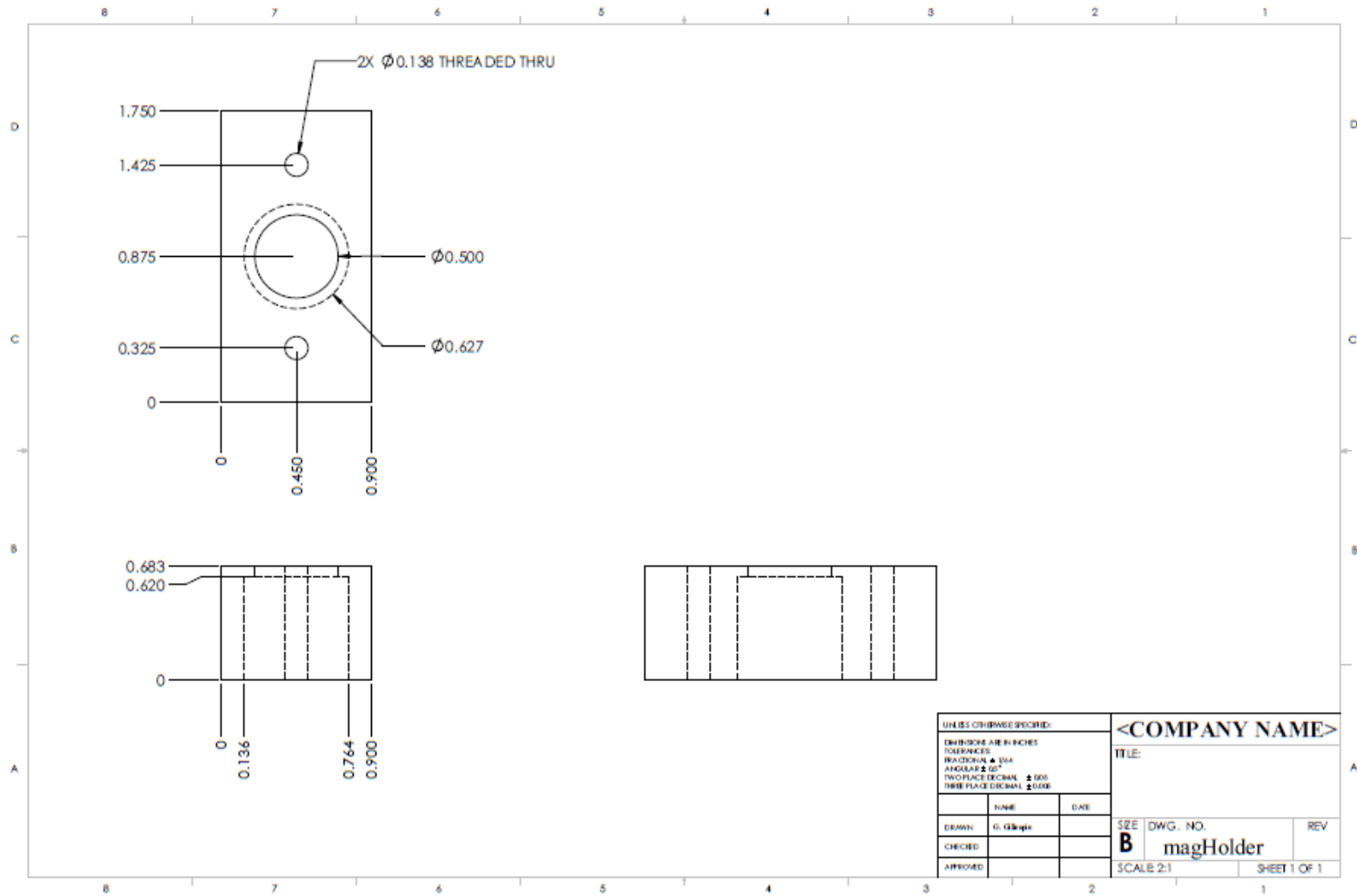


Figure E.8. Magnet holder cap

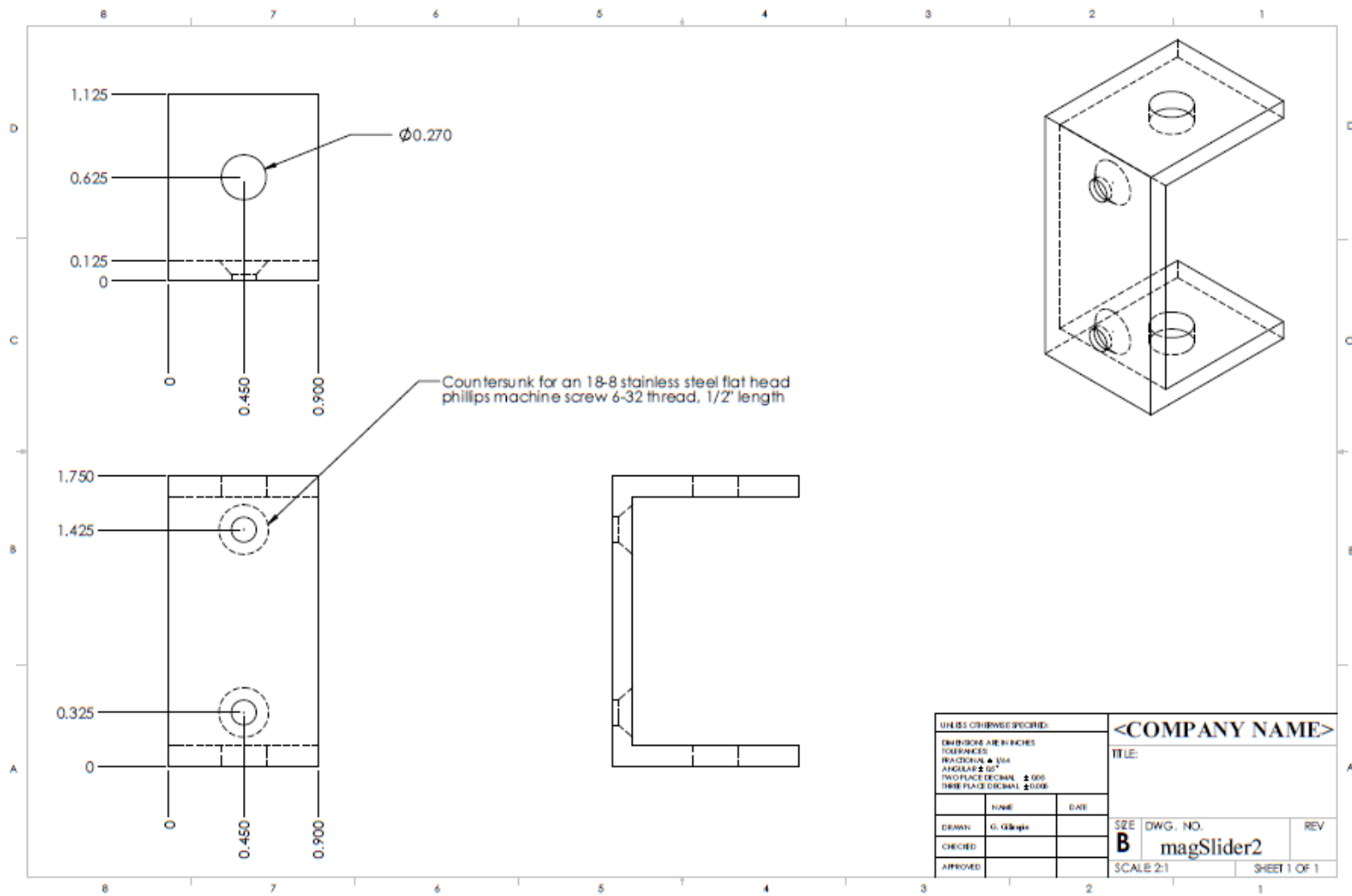


Figure E.9. Magnet holder slider

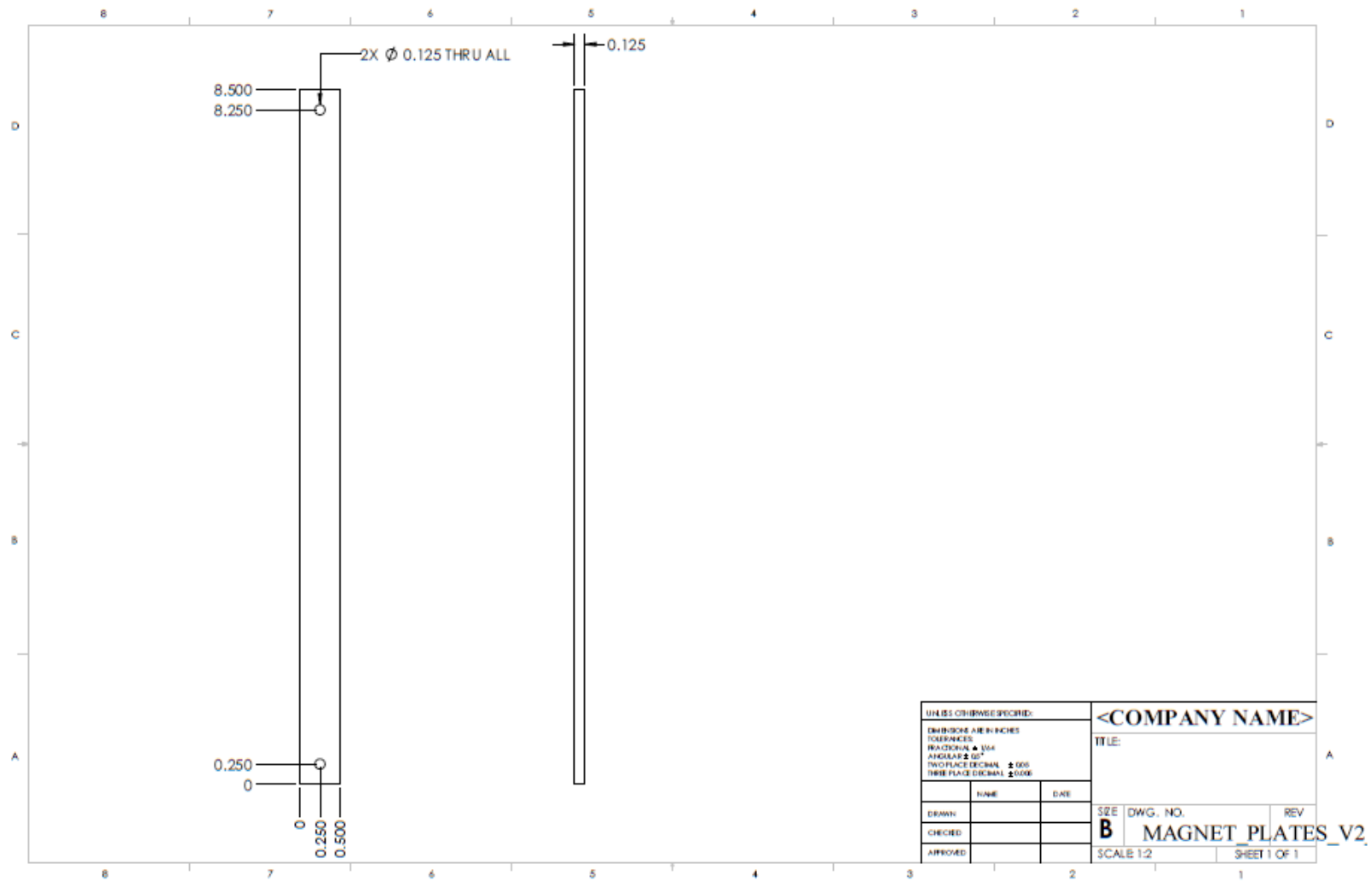


Figure E.10. Pendulum metal plates

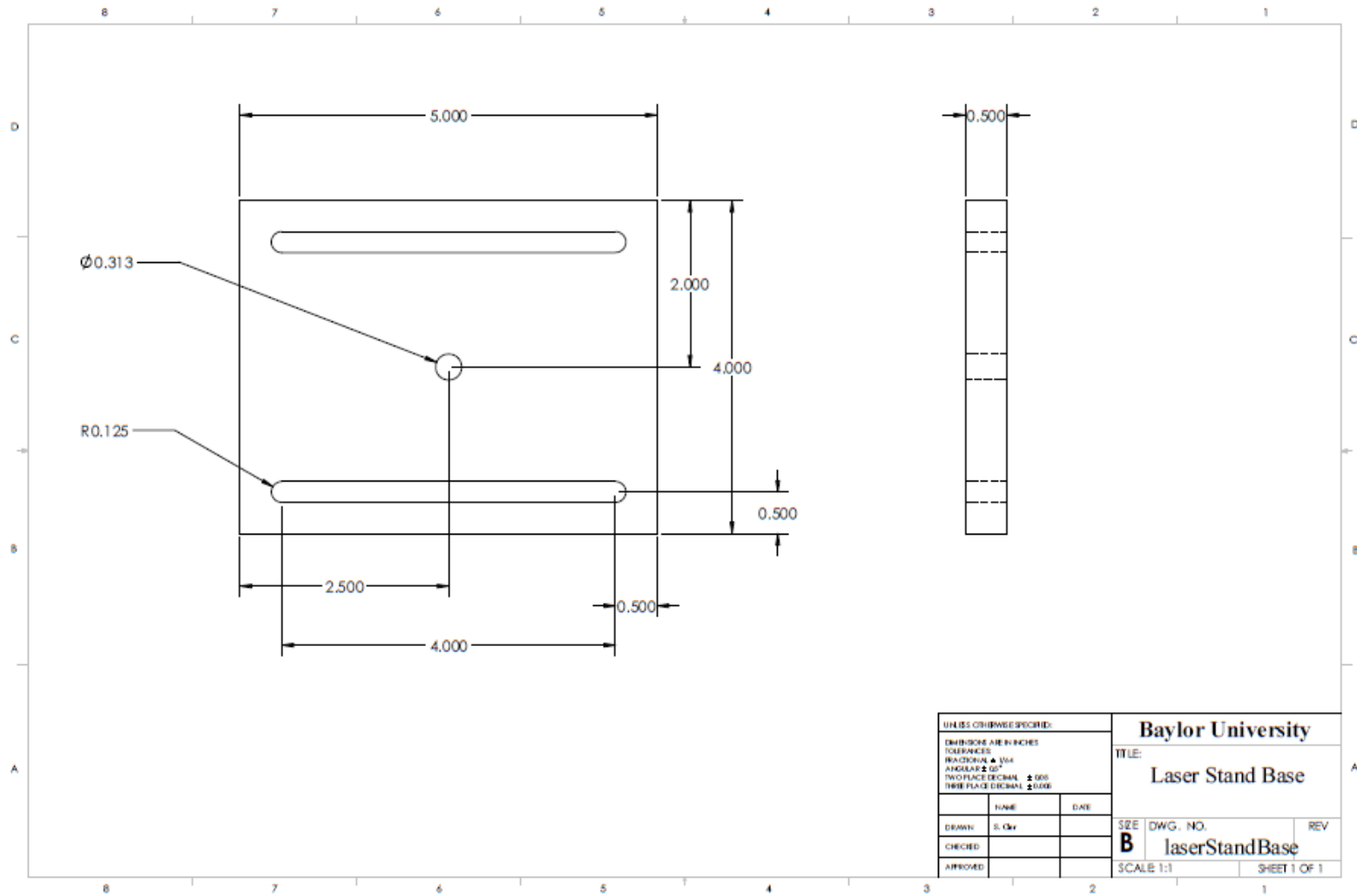
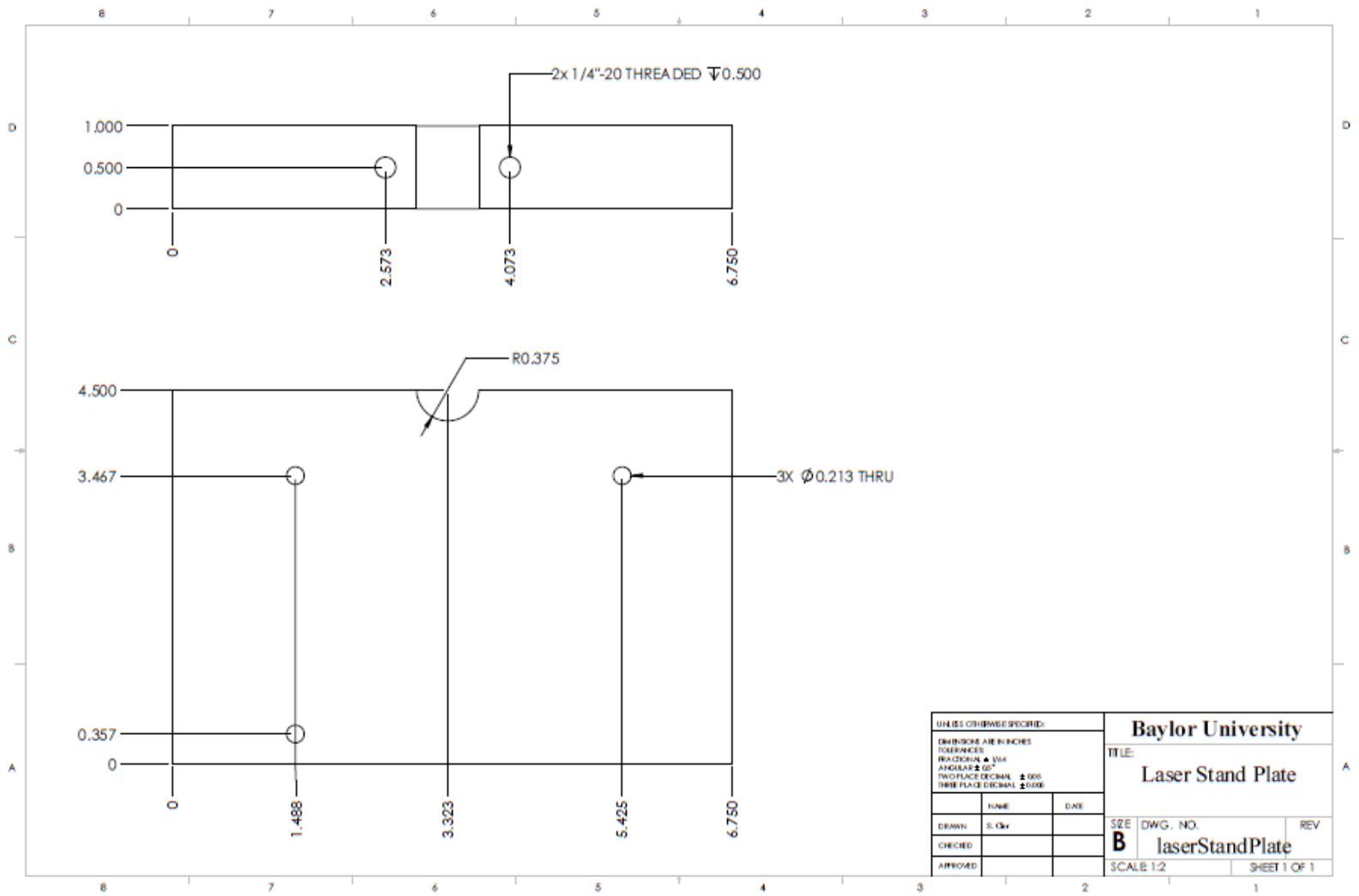
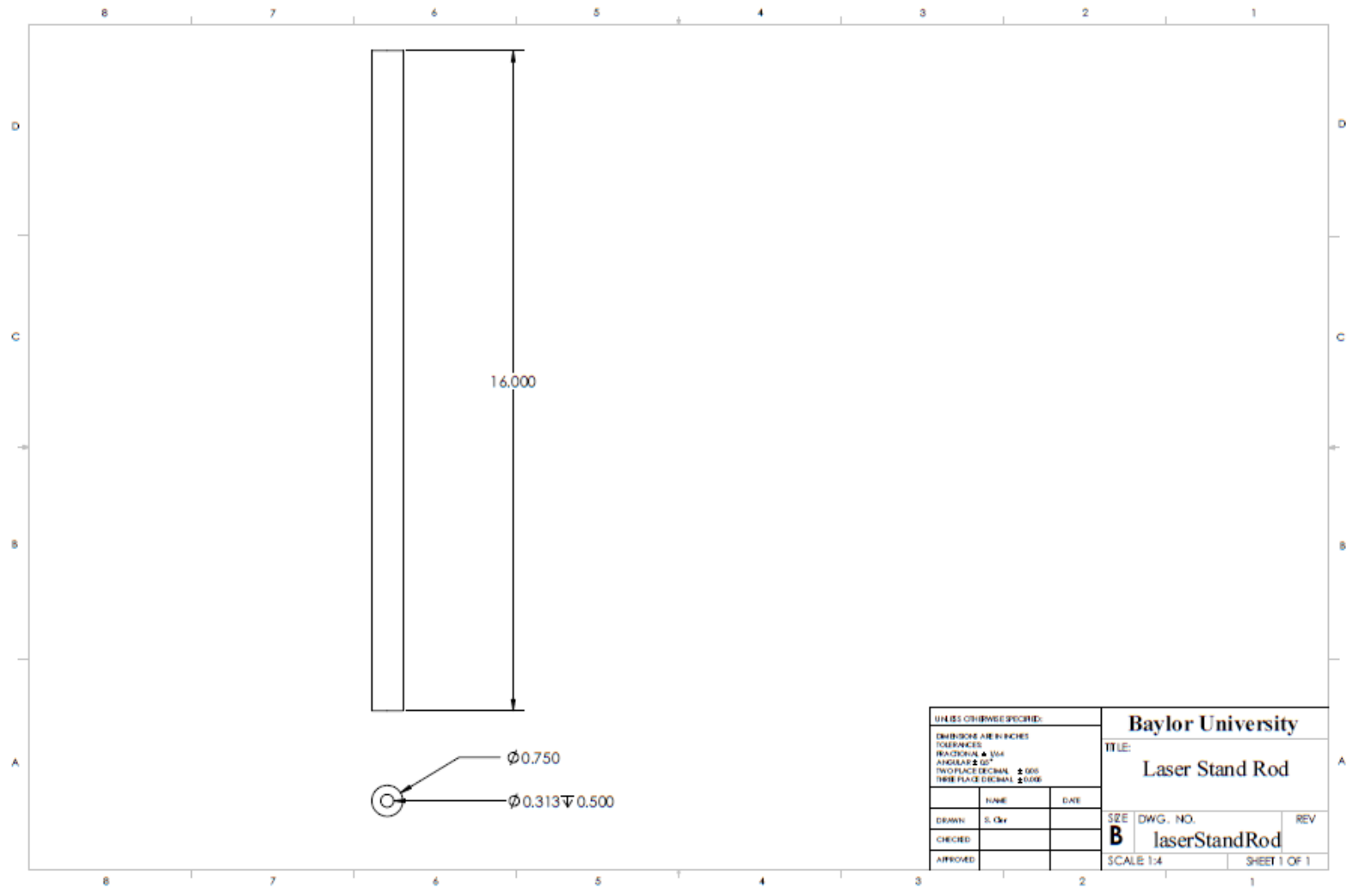


Figure E.11. Laser stand base



UNLESS OTHERWISE SPECIFIED: DIMENSIONS ARE IN INCHES TOLERANCES FRACTIONAL \pm 1/64 ANGULAR \pm 0.5° SURFACE DECIMAL \pm 0.005 THREE PLACE DECIMAL \pm 0.000			Baylor University		
			TITLE: Laser Stand Plate		
	DATE	DATE	SIZE	DWG. NO.	REV
DRAWN	S. Okr		B	laserStandPlate	
CHECKED			SCALE 1:2		SHEET 1 OF 1
APPROVED					

Figure E.12. Laser stand plate



UNLESS OTHERWISE SPECIFIED:			Baylor University		
DIMENSIONS ARE IN INCHES			TITLE:		
TOLERANCES			Laser Stand Rod		
FRACTIONAL \pm 1/64			SIZE	DWG. NO.	REV
ANGULAR \pm 0.01°			B	laserStandRod	
TWO PLACE DECIMAL \pm 0.005			SCALE 1:4		SHEET 1 OF 1
THREE PLACE DECIMAL \pm 0.0005					
	NAME	DATE			
DRAWN:	S. Okr				
CHECKED:					
APPROVED:					

Figure E.13. Laser stand vertical rod

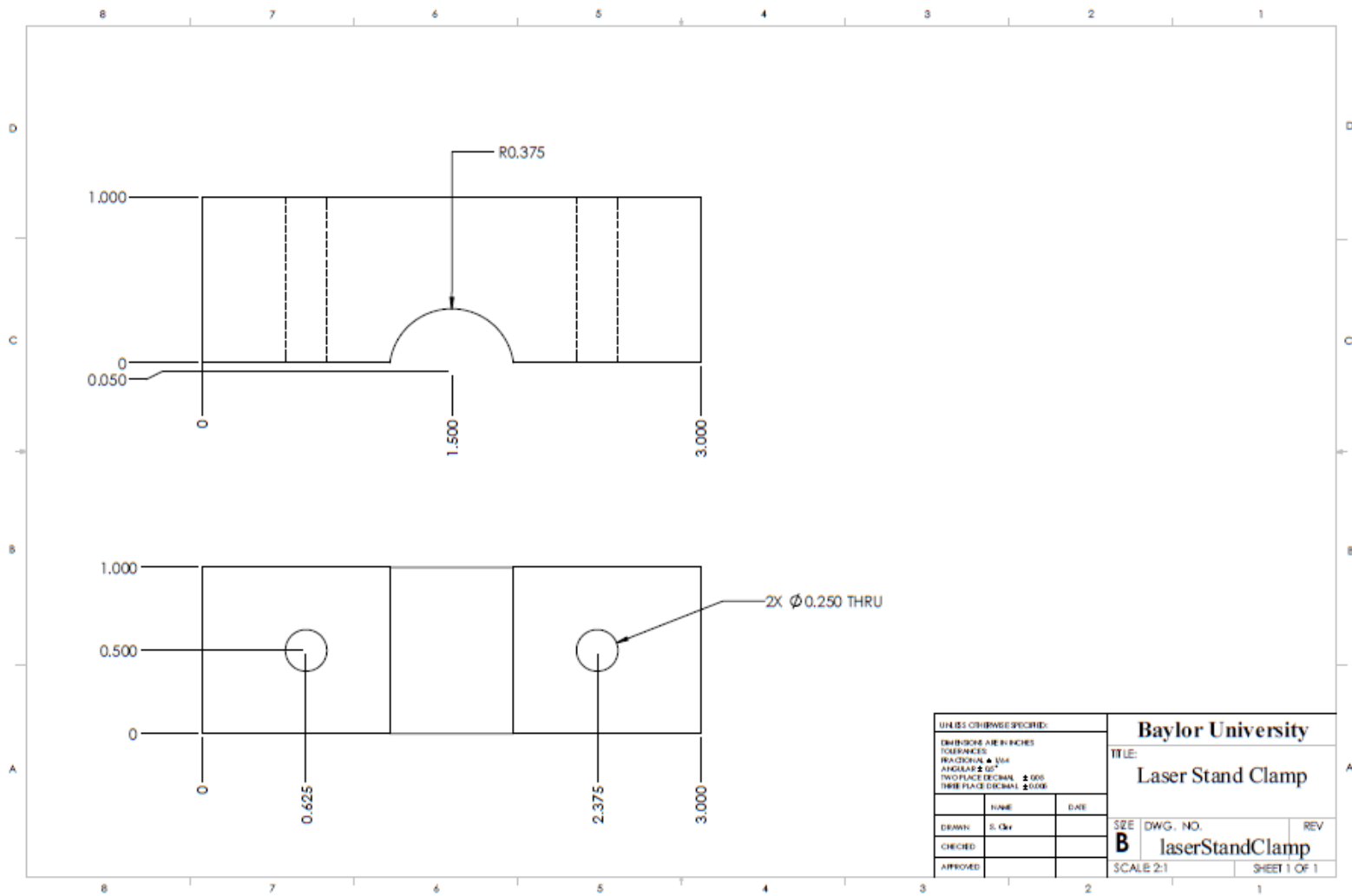


Figure E.14. Laser stand fastener

APPENDIX F

Specifications

Amplifier

XTi 2 Series



XTi 1002, 2002, 4002



XTi 6002

Power Matrix

Model	Channels	2Ω Dual	4Ω Dual	8Ω Dual	4Ω Bridged	8Ω Bridged
1002	2	700W	500W	275W	1400W	1000W
2002	2	1000W	800W	475W	2000W	1600W
4002	2	1600W	1200W	650W	3200W	2400W
6002	2	3000W	2100W	1200W	6000W	4200W

*1kHz, 20ms burst, both channels driven

Figure F.1. Amplifier specifications part 1

Amplifier Performance Specifications	XTi 1002	XTi 2002	XTi 4002	XTi 6002
Sensitivity (for full rated power at 4Ω)	1.4V			
Rated Power Output (per Channel at 4Ω)	500W Stereo	800W Stereo	1200W Stereo	2100W Stereo
Signal to Noise Ratio (below rated 1 kHz power at 8Ω)	100 dB (A Weighted)	100 dB (A Weighted)	100 dB (A Weighted)	103 dB (A Weighted)
Total Harmonic Distortion	<0.5%			
Damping Factor 20 Hz to 1 kHz	>500			
Frequency Response (at 1W, 20 Hz to 20 kHz)	+0 dB, -1 dB			
Crosstalk (below rated power) 20 Hz to 1 kHz	>70 dB			
Input Impedance	20kΩ balanced, 10kΩ unbalanced			
Physical Specifications				
Width	19 in. (48.3cm)			
Height	3.5 in. (8.9cm)			
Depth	12.25 in. (31.1 cm)	12.25 in. (31.1 cm)	12.25 in. (31.1 cm)	16.2 in. (41.1 cm)
Net Weight	18.5 lbs (8.4kg)	18.5 lbs (8.4kg)	18.5 lbs (8.4kg)	24 lbs (10.9kg)
Shipping Weight	21.5 lbs (9.75kg)	21.5 lbs (9.75kg)	21.5 lbs (9.75kg)	30 lbs (13.6kg)

Figure F.2. Amplifier specifications part 2

Laser Vibrometer

Table F.1. Laser Vibrometer Specifications

Model		LJ-V7300	
Light source	Type	Blue semiconductor laser	
	Wavelength	405 nm (visible beam)	
	Laser class	Class 2 Laser Product (IEC60825-1, FDA(CDRH) Part 1040.10 ^{*1})	
	Output	4.8 mW	
Measuring range	Z-axis (Height)	±145 mm 5.71" (F.S.=290 mm 11.42")	
	X-axis (Width)	Near	110 mm 4.33"
		Reference distance	180 mm 7.09"
		Far	240 mm 9.45"
Repeatability	Z-axis (Height)	5 μm 0.000197"	
	X-axis (Width)	60 μm 0.002363"	
Profile data interval		300 μm 0.012"	
Linearity Z-axis (Height)		±0.05 to ^{*2} ±0.15% of F.S.	
Mounting conditions		Diffuse reflection	
Reference distance		300 mm 11.81"	
Spot shape (at reference distance)		Approx 240 mm x 610 μm 9.45" x 0.024016"	
Sampling cycle (trigger interval)		Top speed: 16 μs (high-speed mode) Top speed: 32 μs (advanced function mode)	
Temperature characteristics		0.01% of F.S./°C	
Enclosure rating		IP67 (IEC60529)	
Environmental resistance	Operating ambient luminance	Incandescent lamp: 10000 lux max	
	Operating temperature range	0 to +45°C 32 to 113°F	
	Operating ambient humidity	20 to 85% RH (No condensation)	
	Shock resistance	15 G/6 msec	
	Vibration	10 to 57 Hz, 1.5 mm 0.06" double amplitude in X, Y, and Z directions, 3 hours respectively	
Material		Aluminum	
Weight		Approx 1000 g	
^{*1} The laser classification for FDA(CDRH) is implemented based on IEC60825-1 in accordance with the requirements of Laser Notice No. 50. ^{*2} The linearity will differ depending on the measurement area.			

Linear Guide

A custom slide was ordered. In addition to the specifications listed below, the slide is made of nonmagnetic materials. The Model name is S1-4AC-NMS.

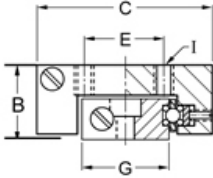
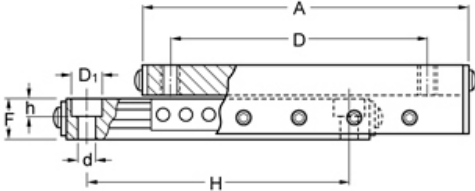


Anti-Creep Linear Slides - Inch
 Family: S1-AC
 Model: S1-4AC
 Price: \$ 144.00

The standard finish is a clear anodize carriage and black anodize base. Other finishes are available on request.

Add to cart

Carriage 4 Holes (I)	6-32 UNC-2B Thread
Base Hole d	.157
Base Hole D ₁	.244
Base Hole h	.150
Counter Bore Screw Size	#6

Custom slides available. Please call to learn more.

All dimensions in inches unless otherwise specified													
Model	Price \$	Travel	Load (lbs)	Weight (oz)	Length A	Height B	Width C	Carriage Hole Spacing		Base Dimensions			Accuracy (in/in of travel)
								D	E	F	G	H	
S1-4AC	144.00	4	35	8.2	6.00	0.62	1.50	5.375	0.625	0.340	0.750	4.000	.0005

https://www.deltron.com/search/Slides_Ball_Crossed_Roller_Model.aspx?pkid=3023

Figure F.3. Linear guide specifications

114

Shaker



PERMANENT MAGNET SHAKER SYSTEMS

Small Permanent Magnet Systems	VTS 40	VTS 65	VTS 80	VTS 100	VTS 150
LOW COST, LOW FORCE VIBRATION SYSTEMS					
Peak Sine	40 lbf	65 lbf	80 lbf	100 lbf	150 lbf
Amplifier Cooling Fan	INCLUDED				
Vibrator Cooling Fan	N/A	INCLUDED			
Stroke (p-p)	.75"	.75"	.75"	.75"	1.0"
Velocity	35 ips	70 ips	80 ips	100 ips	70 ips
Max. Acceleration (bare table)	60g	100g	115g	150g	210g
Armature Weight	.66 lbs	.66 lbs	.70 lbs	.66 lbs	.71 lbs
Suspension Stiffness	40 lbs./in (options available for larger payloads)				
First Major Resonance	4500 Hz	4500 Hz	7000 Hz	4500 Hz	5400 Hz
Frequency Range	2-6500 Hz				2-8500 Hz
Nominal Impedance	6 Ohms				
Power Requirements	4A/120V 2A/240V	14A/120V 8A/240V	18A/120V 10A/240V	18A/120V 10A/240V	28A/120V 15A/240V

Figure F.4. Shaker specifications

APPENDIX G

Testing Apparatus of Prior Study

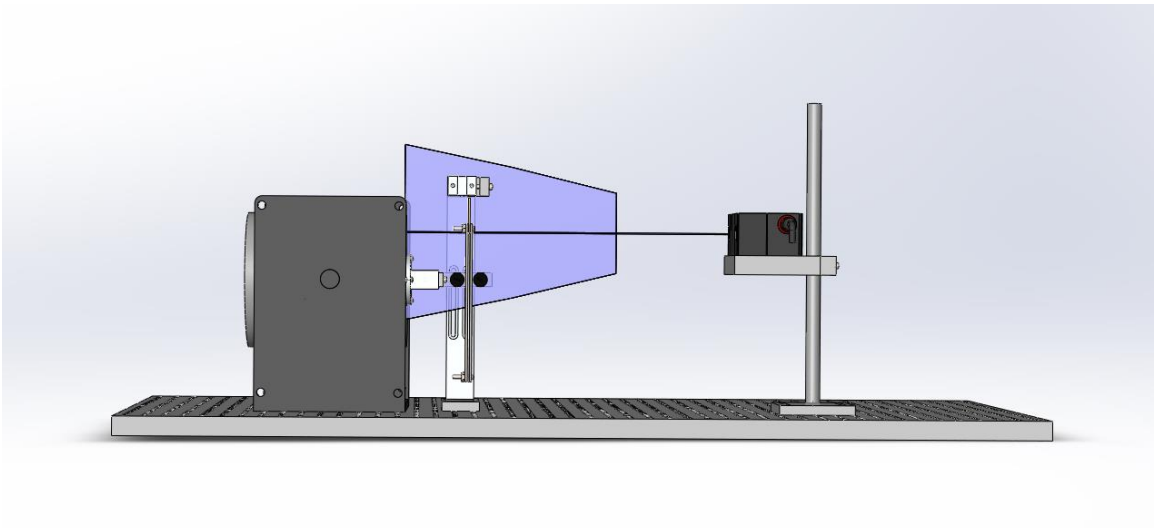


Figure G.1. Testing apparatus used in previous study

APPENDIX H

Bill of Materials

Table H.1. Bill of Materials

Division of Work/Machine	Name of Item	Company Purchased From	Location
Specimens and prep	Bovine bone-4 Femurs	Animbal Technologies	Tyler, TX
	Bandsaw	Craftsman	
	IsoMet 1000 Precision Saw	Buehler	41 Waukegan Road, Lake Bluff,
	114276 : IsoMet Wafering Blades - 15 LC, 6 X 0.020 in	Buehler	Illinois 60044
	106001: Cool 3	Buehler	
	Ziploc bags (gallon)	N/A	
	File for notches	Lowes	
	13" Drill press-11/64" bit	Central Machinery	
	SP6001 : Scout Pro Digital Scale	Ohaus Corporation	7 Campus Drive, Suite 310, Parsippany, NJ 07054
	Machine - Pendulum Assembly	Aluminum Plate (Spacer); 5" x 1/2" x 1/8"	Lowes
Weldable Flat Bar			
Magnetic Plates (2); 9 1/4" x 1/2" x 1/8"		Lowes	
Weldable Flat Bar			
Attachment Piece to Shaker; Multipurpose 6061 Aluminum Alloy; Rectangular Bar, 1/8" x 2-1/2", 6" Long		McMaster-Carr	6100 Fulton Industrial Blvd. SW, Atlanta, GA 30336-2853
Bottom Arm; Multipurpose 6061 Aluminum Alloy; Tube, 1/8" Wall Thickness, 1" x 1-1/2", 1' Length		McMaster-Carr	
Top Arm & Fastener Cap, Vertical Bar; Multipurpose 6061 Aluminum Alloy; 1" Thick, 1- 1/2" Width, 3' Length		McMaster-Carr	
Linear Guide Conversion Piece; 0.875" Thick, 3" Wide and 6" Long		N/A	
Nexus Vibration Isolation Table		Thorlabs	56 Sparta Ave., Newton, NJ 07860
Anticreep, non-magnetic, linear slide; S1-4AC- NMS		Del-Tron Precision, Inc.	5 Trowbridge Dr., P.O. Box 505, Bethel, CT 06801
Cam Followers (2)- 3/4" diameter		MSC Industrial Supply Co.	75 Maxess Road, Melville, NY 157 RMX Way, Petersburg, WV 26847
5/8"x5/8" Cylinders - 2 Neodymium Rare Earth Magnets		Apex Magnets	
Machine - Laser Stand		Base Plate-Aluminum 1/2" Thick, 5" Width, 4" Length	N/A
	Beam-Aluminum 3/4" Diameter, 16-1/2" Length	N/A	
	Stage-Aluminum 1" Thick, 6-3/4" Width, 5-1/2" Length	N/A	
Machine-linear guide, shaker, blower, laser vibrometer, amplifier	VTS-100	Vibration Test Systems, Inc.	10246 Clipper Cove, Aurora, OH 44202
	VTS blower	Vibration Test Systems, Inc.	
	VTS shaker-blower hose	Vibration Test Systems, Inc.	
	Laser vibrometer: LJ-V7300	Keyence	1100 North Arlington Heights Road, Suite210, Itasca, IL 60143
	Laser vibrometer: DC24V Power source	Keyence	
	Laser vibrometer: Controller	Keyence	
	Laser vibrometer: Head cable	Keyence	
2002 XTiSeries Amplifier	Crown Audio	1718 W. Mishawaka Road, Elkhart, IN 46517	
Electrical - DAQ Related	9205 32-Channel +/-10 V, 250 kS/s, 16-Bit Analog Input Module	National Instruments Corporation	11500 N Mopac Expwy, Austin, TX 78759-3504
	NI 9201 Screw Terminal, +/- 10 V, 12-Bit, 500 KS/S , 8-CH, AI C Series Module	National Instruments Corporation	

Table H.1 continued. Bill of Materials

	9263 Screw Terminal, +/-10V, 16-Bit, 100 bS/s/ch, 4-ch, Simult AO C Series Module cDAQ-9174, CompactDAQ chassis (4 slot USB)	National Instruments Corporation National Instruments Corporation	
	Power Cord, AC, US, 120 VAC, 2.3 meters	National Instruments Corporation	
Black box	Black felt	JoAnns Fabric	4633 Jack Kultgen Fwy #104, Waco, TX 76706
	Black thread	JoAnns Fabric	
	Velcro	JoAnns Fabric	
	Fabric glue	JoAnns Fabric	
	XE25W3 : Quick corner cube for 25 mm Rails	Thorlabs, Inc.	56 Sparta Ave., Newton, NJ 07860
	XE25A90 : Right-Angle Bracket for 25 mm Rails	Thorlabs, Inc.	
	SH25LP38 : 1/4"-20 Low-Profile Channel Screws (100 Screws/Box)	Thorlabs, Inc.	
	XE25T1 : Drop-In T-Nut, 1/4"-20 Tapped Hole, Qty: 10	Thorlabs, Inc.	
	XE25L48 : 25 mm Construction Rail, L = 48"	Thorlabs, Inc.	
	XE25L24 : 25 mm Construction Rail, L = 24"	Thorlabs, Inc.	
	XE25L28 : 25 mm Construction Rail, L = 28"	Thorlabs, Inc.	
Fasteners	Round-Head Machine Screw Phillips (4) #10-32 x 3/4"	N/A	
	Round-Head Combo Machine Screw (2) #10-24 tpi x 1"	Home Depot	
	Socket Head Cap Screw (22) 1/4" - 20 tpi x 1"	N/A	
	Hex head bolts (3)	Keyence	1100 North Arlington Heights Road, Suite210, Itasca, IL 60143

BIBLIOGRAPHY

- [1] K. Verheyen, J. Price, L. Lanyon, and J. Wood, "Exercise distance and speed affect the risk of fracture in racehorses," *Bone*, vol. 39, no. 6, pp. 1322–1330, Dec. 2006.
- [2] K. L. Bennell, S. A. Malcolm, S. A. Thomas, J. D. Wark, and P. D. Brukner, "The Incidence and Distribution of Stress Fractures in Competitive Track and Field Athletes: A Twelve-Month Prospective Study," *Am. J. Sports Med.*, vol. 24, no. 2, pp. 211–217, Mar. 1996.
- [3] D. S. Patel, M. Roth, and N. Kapil, "Stress Fractures: Diagnosis, Treatment, and Prevention," *Am. Fam. Physician*, vol. 83, no. 1, pp. 39–46, Jan. 2011.
- [4] B. W. Sanderlin and R. F. Raspa, "Common Stress Fractures," *Am. Fam. Physician*, vol. 68, no. 8, pp. 1527–1532, 2003.
- [5] J.-Y. Rho, L. Kuhn-Spearing, and P. Zioupos, "Mechanical properties and the hierarchical structure of bone," *Medical Engineering & Physics*, vol. 20, no. 2, pp. 92–102, Mar. 1998.
- [6] S. A. Wainwright, W. D. Briggs, J. D. Currey, and J. M. Gosline, *Mechanical Design in Organisms*. Princeton, New Jersey: Princeton University Press, 1982.
- [7] V. C. Mow and W. C. Hayes, *Basic Orthopaedic Biomechanics*, Second Edition. Philadelphia, PA: Lippincott-Raven Publishers, 1997.
- [8] A. H. Burstein, J. D. Currey, V. H. Frankel, and D. T. Reilly, "The ultimate properties of bone tissue: The effects of yielding," *Journal of Biomechanics*, vol. 5, no. 1, pp. 35–42, IN1–IN2, 43–44, 1972.
- [9] J. Yan, A. Daga, R. Kumar, and J. J. Mecholsky, "Fracture toughness and work of fracture of hydrated, dehydrated, and ashed bovine bone," *Journal of Biomechanics*, vol. 41, no. 9, pp. 1929–1936, 2008.
- [10] D. J. Hadjidakis and I. I. Androulakis, "Bone Remodeling," *Annals of the New York Academy of Sciences*, vol. 1092, no. 1, pp. 385–396, Dec. 2006.

- [11] C. Ulbrich, M. Wehland, J. Pietsch, G. Aleshcheva, P. Wise, J. van Loon, N. Magnusson, M. Infanger, J. Grosse, C. Eilles, A. Sundaresan, D. Grimm, C. Ulbrich, M. Wehland, J. Pietsch, G. Aleshcheva, P. Wise, J. van Loon, N. Magnusson, M. Infanger, J. Grosse, C. Eilles, A. Sundaresan, and D. Grimm, "The Impact of Simulated and Real Microgravity on Bone Cells and Mesenchymal Stem Cells, The Impact of Simulated and Real Microgravity on Bone Cells and Mesenchymal Stem Cells," *BioMed Research International*, *BioMed Research International*, vol. 2014, 2014, p. e928507, Jul. 2014.
- [12] Y. Sambandam, K. L. Baird, M. Stroebel, E. Kowal, S. Balasubramanian, and S. V. Reddy, "Microgravity Induction of TRAIL Expression in Preosteoclast Cells Enhances Osteoclast Differentiation," *Scientific Reports*, vol. 6, p. 25143, May 2016.
- [13] J. Iwamoto, T. Takeda, and Y. Sato, "Interventions to prevent bone loss in astronauts during space flight," *The Keio Journal of Medicine*, vol. 54, no. 2, pp. 55–59, 2005.
- [14] T. F. Lang, A. D. Leblanc, H. J. Evans, and Y. Lu, "Adaptation of the Proximal Femur to Skeletal Reloading After Long-Duration Spaceflight," *J Bone Miner Res*, vol. 21, no. 8, pp. 1224–1230, Aug. 2006.
- [15] J. D. Currey, *Bones: Structure and Mechanics*. Princeton, New Jersey: Princeton University Press, 2002.
- [16] M. D. Landrigan and R. K. Roeder, "Systematic error in mechanical measures of damage during four-point bending fatigue of cortical bone," *Journal of Biomechanics*, vol. 42, no. 9, pp. 1212–1217, Jun. 2009.
- [17] D. R. Carter and W. C. Hayes, "Compact bone fatigue damage. I. Residual strength and stiffness," *J. Biomech*, vol. 10, no. 5–6, pp. 325–337, 1977.
- [18] J. C. Behiri and W. Bonfield, "Orientation dependence of the fracture mechanics of cortical bone," *J. Biomech*, vol. 22, no. 8–9, pp. 863–872, 1989.
- [19] A. A. Abdel-Wahab, K. Alam, and V. V. Silberschmidt, "Analysis of anisotropic viscoelastoplastic properties of cortical bone tissues," *Journal of the Mechanical Behavior of Biomedical Materials*, vol. 4, no. 5, pp. 807–820, Jul. 2011.
- [20] A. Alto and M. H. Pope, "On the fracture toughness of equine metacarpi," *J. Biomech*, vol. 12, no. 6, pp. 415–421, 1979.

- [21] K. L. Bell, N. Loveridge, J. Power, N. Garrahan, B. F. Meggitt, and J. Reeve, "Regional differences in cortical porosity in the fractured femoral neck," *Bone*, vol. 24, no. 1, pp. 57–64, Jan. 1999.
- [22] V. A. Gibson, S. M. Stover, R. B. Martin, J. C. Gibeling, N. H. Willits, M. B. Gustafson, and L. V. Griffins, "Fatigue behavior of the equine third metacarpus: Mechanical property analysis," *J. Orthop. Res.*, vol. 13, no. 6, pp. 861–868, 1995.
- [23] X. E. Guo, L. C. Liang, and S. A. Goldstein, "Micromechanics of osteonal cortical bone fracture," *J. Biomech. Eng.*, vol. 120, no. 1, pp. 112–117, 1998.
- [24] R. B. Martin, V. A. Gibson, S. M. Stover, J. C. Gibeling, and L. V. Griffins, "Osteonal structure in the equine third metacarpus," *Bone*, vol. 19, no. 2, pp. 165–171, Aug. 1996.
- [25] D. Moyle, J. W. Welborn III, and F. W. Cooke, "Work to fracture of canine femoral bone," *J. Biomech.*, vol. 11, no. 10–12, pp. 435–440, 1978.
- [26] A. Varvani-Farahani and H. Najmi, "A damage assessment model for cadaveric cortical bone subjected to fatigue cycles," *International Journal of Fatigue*, vol. 32, no. 2, pp. 420–427, Feb. 2010.
- [27] H. S. Gupta and P. Zioupos, "Fracture of bone tissue: The 'hows' and the 'whys,'" *Medical Engineering & Physics*, vol. 30, no. 10, pp. 1209–1226, Dec. 2008.
- [28] M. B. Schaffler, K. Choi, and C. Milgrom, "Aging and matrix microdamage accumulation in human compact bone," *Bone*, vol. 17, no. 6, pp. 521–525, Dec. 1995.
- [29] H. M. Frost, "Presence of microscopic cracks in vivo in bone," *Henry Ford Hosp Med Bull*, vol. 8, pp. 25–35, 1960.
- [30] S. Mori and D. B. Burr, "Increased Intracortical Remodeling Following Fatigue Damage," *Bone*, vol. 14, pp. 103–109, 1993.
- [31] O. Verborgt, G. J. Gibson, and M. B. Schaffler, "Loss of osteocyte integrity in association with microdamage and bone remodeling after fatigue in vivo," *J. Bone*, vol. 15, pp. 60–67, 2000.
- [32] V. Bentolila, T. M. Boyce, D. P. Fyhrie, R. Drumb, T. M. Skerry, and M. B. Schaffler, "Intracortical remodeling in adult rat long bones after fatigue loading," *Bone*, vol. 23, no. 3, pp. 275–281, Sep. 1998.
- [33] D. B. Burr, "Why bones bend but don't break," *J Musculoskelet Neuronal Interact*, vol. 11, no. 4, pp. 270–285, 2011.

- [34] R. O. Ritchie, M. J. Buehler, and P. Hansma, "Plasticity and toughness in bone," *Physics Today*, vol. 62, no. 6, pp. 41–47, Jun. 2009.
- [35] H. Peterlik, P. Roschger, K. Klaushofer, and P. Fratzl, "From brittle to ductile fracture of bone," *Nat Mater*, vol. 5, no. 1, pp. 52–55, Jan. 2006.
- [36] U. Hansen, P. Zioupos, R. Simpson, J. D. Currey, and D. Hynd, "The Effect of Strain Rate on the Mechanical Properties of Human Cortical Bone," *J Biomech Eng*, vol. 130, no. 1, pp. 011011–011011, Feb. 2008.
- [37] G. E. Fantner, T. Hassenkam, J. H. Kindt, J. C. Weaver, H. Birkedal, L. Pechenik, J. A. Cutroni, G. A. G. Cidade, G. D. Stucky, D. E. Morse, and P. K. Hansma, "Sacrificial bonds and hidden length dissipate energy as mineralized fibrils separate during bone fracture," *Nat Mater*, vol. 4, no. 8, pp. 612–616, Aug. 2005.
- [38] J. J. Kruzic and R. O. Ritchie, "Fatigue of mineralized tissues: Cortical bone and dentin," *Journal of the Mechanical Behavior of Biomedical Materials*, vol. 1, no. 1, pp. 3–17, Jan. 2008.
- [39] R. K. Nalla, J. H. Kinney, and R. O. Ritchie, "Mechanistic fracture criteria for the failure of human cortical bone," *Nat Mater*, vol. 2, no. 3, pp. 164–168, Mar. 2003.
- [40] R. K. Nalla, J. J. Kruzic, J. H. Kinney, and R. O. Ritchie, "Mechanistic aspects of fracture and R-curve behavior in human cortical bone," *Biomaterials*, vol. 26, no. 2, pp. 217–231, Jan. 2005.
- [41] R. K. Nalla, J. S. Stölken, J. H. Kinney, and R. O. Ritchie, "Fracture in human cortical bone: local fracture criteria and toughening mechanisms," *Journal of Biomechanics*, vol. 38, no. 7, pp. 1517–1525, Jul. 2005.
- [42] R. O. Ritchie, J. H. Kinney, J. J. Kruzic, and R. K. Nalla, "A fracture mechanics and mechanistic approach to the failure of cortical bone," *Fatigue Fract. Eng. Mater. Struct.*, vol. 28, no. 4, pp. 345–371, 2005.
- [43] M. E. Launey, M. J. Buehler, and R. O. Ritchie, "On the Mechanistic Origins of Toughness in Bone," *Annual Review of Materials Research*, vol. 40, no. 1, pp. 25–53, 2010.
- [44] P. K. Hansma, G. E. Fantner, J. H. Kindt, P. J. Thurner, G. Schitter, P. J. Turner, S. F. Udwin, and M. M. Finch, "Sacrificial bonds in the interfibrillar matrix of bone," *J. Musculoskelet. Neuronal Interact*, vol. 5, no. 4, p. 313, 2005.
- [45] J. B. Thompson, J. H. Kindt, B. Drake, H. Hansma, D. E. Morse, and P. Hansma, "Bone indentation recovery time correleates with bond reforming time," *Nature*, vol. 414, pp. 773–776, 2001.

- [46] H. S. Gupta, W. Wagermaier, G. A. Zickler, J. Hartmann, S. S. Funari, P. Roschger, H. D. Wagner, and P. Fratzl, “Fibrillar level fracture in bone beyond the yield point,” *Int J Fract*, vol. 139, no. 3–4, pp. 425–436, Jun. 2006.
- [47] H. S. Gupta, W. Wagermaier, G. A. Zickler, D. Raz-Ben Aroush, S. S. Funari, P. Roschger, H. D. Wagner, and P. Fratzl, “Nanoscale Deformation Mechanisms in Bone,” *Nano Lett.*, vol. 5, no. 10, pp. 2108–2111, Oct. 2005.
- [48] H. S. Gupta, P. Fratzl, M. Kerschnitzki, G. Benecke, W. Wagermaier, and H. O. K. Kirchner, “Evidence for an elementary process in bone plasticity with an activation enthalpy of 1eV,” *J. R. Soc. Interface*, vol. 4, no. 13, pp. 277–282, 2007.
- [49] P. Braidotti, F. P. Branca, and L. Stagni, “Scanning electron microscopy of human cortical bone failure surfaces,” *Journal of Biomechanics*, vol. 30, no. 2, pp. 155–162, Feb. 1997.
- [50] L. P. Hiller, S. M. Stover, V. A. Gibson, J. C. Gibeling, C. S. Prater, S. J. Hazelwood, O. C. Yeh, and R. B. Martin, “Osteon pullout in the equine third metacarpal bone: Effects of ex vivo fatigue,” vol. 21, no. 3, pp. 481–488, Jan. 2006.
- [51] D. R. Carter and W. E. Caler, “Cycle-dependent and time-dependent bone fracture with repeated loading,” *J. Biomech.*, vol. 105, no. 2, pp. 166–170, May 1983.
- [52] C. A. Pattin, W. E. Caler, and D. R. Carter, “Cyclic mechanical property degradation during fatigue loading of cortical bone,” *Journal of Biomechanics*, vol. 29, no. 1, pp. 69–79, Jan. 1996.
- [53] K. S. Ravichandran, R. O. Ritchie, and Y. Murakami, Eds., “Cause of Unsuccessful Results of Miner’s Rule: Behavior of Small Fatigue Crack Growth Under Repeated Two-Step Loadings,” in *Small Fatigue Cracks: Mechanics, Mechanisms and Applications*, Kidlington, Oxford OX5 1GB, UK: Elsevier Science Ltd., 1999, pp. 119–130.
- [54] S. L. Evans, “Fatigue crack propagation under variable amplitude loading in PMMA and bone cement,” *J Mater Sci: Mater Med*, vol. 18, no. 9, pp. 1711–1717, May 2007.
- [55] D. Chelidze, J. P. Cusumano, and A. Chatterjee, “A Dynamical Systems Approach to Damage Evolution Tracking, Part 1: Description and Experimental Application,” *J. Vib. Acoust*, vol. 124, no. 2, pp. 250–257, Mar. 2002.
- [56] J. P. Cusumano, D. Chelidze, and A. Chatterjee, “A Dynamical Systems Approach to Damage Evolution Tracking, Part 2: Model-Based Validation and Physical Interpretation,” *J. Vib. Acoust*, vol. 124, no. 2, pp. 258–264, Mar. 2002.

- [57] D. Chelidze and M. Liu, “Dynamical systems approach to fatigue damage identification,” *Journal of Sound and Vibration*, vol. 281, no. 3–5, pp. 887–904, Mar. 2005.
- [58] D. Chelidze and J. P. Cusumano, “Phase space warping: nonlinear time-series analysis for slowly drifting systems,” *Philosophical Transactions of the Royal Society of London A: Mathematical, Physical and Engineering Sciences*, vol. 364, no. 1846, pp. 2495–2513, Sep. 2006.
- [59] D. Chelidze and M. Liu, “Reconstructing slow-time dynamics from fast-time measurements,” *Philosophical Transactions of the Royal Society of London A: Mathematical, Physical and Engineering Sciences*, vol. 366, no. 1866, pp. 729–745, Mar. 2008.
- [60] A. Z. Palmgren, “Die Lebensdauer von Kugellagren,” *Z. Ver. Dtsch. Ingenieure*, vol. 68, pp. 339–341, 1924.
- [61] A. J. McEvily, S. Ishihara, and M. Endo, “On the Causes of Deviation from the Palmgren-Miner Rule,” *Fatigue Test. Anal. Var. Amplitude Load. Cond. ASTM STP*, vol. 1439, 2004.
- [62] J. Schijve, “Fatigue of structures and materials in the 20th century and the state of the art,” *International Journal of Fatigue*, vol. 25, no. 8, pp. 679–702, Aug. 2003.
- [63] C. Amzallag, “Standardization of the rainflow counting method for fatigue analysis,” *Int J Fatigue*, vol. 16, no. 4, pp. 287–293, Jun. 1994.
- [64] M. Matsuishi and T. Endo, “Fatigue of Metals Subjected to Varying Stress,” *Jpn. Soc. Mech. Eng.*, pp. 37–40, 1968.
- [65] A. M. Campbell, “Damage Accumulation of Bovine Bone under Variable Amplitude Loads,” Master of Science in Biomedical Engineering, Baylor University, Waco, TX, 2016.
- [66] D. Chelidze and W. Zhou, “Smooth orthogonal decomposition-based vibration mode identification,” *Journal of Sound and Vibration*, vol. 292, no. 3–5, pp. 461–473, May 2006.
- [67] R. H. Rand, “Lecture Notes on Nonlinear Vibrations.” 2005.
- [68] R. D. Thomas, N. C. Moses, E. A. Semple, and A. J. Strang, “An efficient algorithm for the computation of average mutual information: Validation and implementation in Matlab,” *Journal of Mathematical Psychology*, vol. 61, pp. 45–59, Aug. 2014.

- [69] S. Skogestad, C. Rhodes, and M. Morari, “The false nearest neighbors algorithm: An overview,” *Computers & Chemical Engineering*, vol. 21, pp. S1149–S1154, May 1997.
- [70] D. Chelidze, “Smooth local subspace projection for nonlinear noise reduction,” *Chaos*, vol. 24, no. 1, p. 013121, Mar. 2014.
- [71] “A biological raw materials resource.” Animal Technologies, Inc., 2015.